Eur. Phys. J. Spec. Top. (2025) 234:861–917
https://doi.org/10.1140/epjs/s11734-025-01605-z

THE EUROPEAN PHYSICAL JOURNAL SPECIAL TOPICS

Review

Technical design report for the cryogenic stopping cell of the Super-FRS at FAIR

Daler Amanbayev[1,2], Wolfgang R. Plaß[2,1,a], Timo Dickel[2,1], Samuel Ayet San Andrés[1,2,3], Peter Dendooven[4,15], Hans Geissel[2,1], Emma Haettner[2], Muhsin N. Harakeh[4], Ivan Miskun[1], Sivaji Purushothaman[2], Manisha Ranjan[4], Moritz P. Reiter[1,5], Ann-Kathrin Rink[1], Christoph Scheidenberger[1,2,6], Zoran Andelkovic[2], Soumya Bagchi[1,2,16], Dimiter Balabanski[7], Sönke Beck[1,2], Julian Bergmann[1], Michael Block[2], Paul Constantin[7], Sterian Danaila[8], Jens Ebert[1], Florian Greiner[1,2], Lizzy Gröf[1], Fabian Heiße[1,2,9], Frank Herfurth[2], Christine Hornung[1,2], Christian Jesch[1], Nasser Kalantar-Nayestanaki[4], Israel Mardor[10,11], Mihai Merisanu[7], Iain D. Moore[12], Martin Petrick[1], Stephane Pietri[2], Ilkka Pohjalainen[12], Anamaria Spataru[7,13], Alexandru N. State[7,13], Helmut Weick[2], John S. Winfield[2], Martin Winkler[2], Mikhail I. Yavor[14], and for the Super-FRS Experiment Collaboration

[1] II. Physikalisches Institut, Justus-Liebig-Universität Gießen, Gießen, Germany
[2] GSI Helmholtzzentrum für Schwerionenforschung GmbH, Darmstadt, Germany
[3] University of Valencia, Valencia, Spain
[4] University of Groningen, Groningen, The Netherlands
[5] University of Edinburgh, Edinburgh, UK
[6] Helmholtz Research Academy Hesse for FAIR (HFHF), GSI Helmholtz Center for Heavy Ion Research, Campus Gießen, Gießen, Germany
[7] Extreme Light Infrastructure-Nuclear Physics, Horia Hulubei National Institute for Physics and Nuclear Engineering, Magurele, Romania
[8] Department of Aerospace Sciences, Politehnica University of Bucharest, Bucharest, Romania
[9] Institut für Kern- und Teilchenphysik, Technische Universität Dresden, Dresden, Germany
[10] School of Physics and Astronomy, Tel Aviv University, Tel Aviv, Israel
[11] Soreq Nuclear Research Center, Yavne, Israel
[12] University of Jyväskylä, Jyväskylä, Finland
[13] Doctoral School in Engineering and Applications of Lasers and Accelerators, University Polytechnica of Bucharest, Bucharest, Romania
[14] Institute for Analytical Instrumentation, Russian Academy of Sciences, St. Petersburg, Russia
[15] Present Address: PARTREC & Department of Radiation Oncology, University Medical Center Groningen, Groningen, The Netherlands
[16] Present Address: Department of Physics, Indian Institute of Technology (Indian School of Mines) Dhanbad, Jharkhand, India

Received 31 December 2024 / Accepted 31 March 2025 / Published online 8 May 2025

H. Geissel and J. S. Winfield: Deceased.

This publication is an updated version of the Technical Report for the Design, Construction and Commissioning of the Cryogenic Stopping Cell of the Super-FRS, which was evaluated and approved previously by the Expert Committee Experiments of the Facility for Antiproton and Ion Research (FAIR).

[a] e-mail: W.Plass@gsi.de (corresponding author)

Abstract Precision experiments with thermalized exotic nuclei will be possible at the super-conducting fragment separator Super-FRS at the Facility for Antiproton and Ion Research (FAIR). In the Early Science/First Science programs of FAIR, they will be performed at the focal plane FHF1 of the Super-FRS (in front of the High-Energy Branch) and, at a later stage during First Science++, also at the Low-Energy Branch. Exotic nuclei will be produced in flight and separated in the Super-FRS and their momentum spread will be reduced by energy-bunching. The ions will be further slowed down in a homogeneous degrader, thermalized in a gas-filled stopping cell, and extracted and transferred to the experimental setups. The stopping cell is, thus, a key device for experiments with thermalized exotic nuclei, and its performance characteristics will have a strong impact on the range of nuclides available and their yields, since its stopping and extraction efficiencies and extraction times strongly influence the rate of the extracted nuclei and put a limit on their lifetimes.In combination with a multiple-reflection time-of-flight mass spectrometer, the stopping cell will enable the measurement of masses, branching ratios, e.g., β-delayed (multi-)neutron emission probabilities, and lifetimes, as well as the in-cell production of exotic nuclei by multi-nucleon transfer with primary and secondary beams. Moreover, it will be a tool for the absolute calibration of the particle identification in the Super-FRS. Furthermore, using the combination of accurate mass determination with the PID of the Super-FRS on an event-by-event basis, completely new experimental possibilities will become available, such as the identification of millisecond isomers at the Super-FRS and the measurement of the dependence of the isomer-to-ground-state ratios on the production mechanism. These studies will be pursued in the context of the Super-FRS Experiment Collaboration.At the Low-Energy Branch, high-accuracy mass measurements, in-trap conversion electron and alpha spectroscopy, and trap-assisted spectroscopy will be performed with MATS (Precision Measurements of very short-lived nuclei using an Advanced Trapping System for highly charged ions). Measurements of nuclear spins, magnetic dipole and electric quadrupole moments, and root-mean-square charge radii will be carried out using collinear laser spectroscopy on ions and atoms and beta-NMR experiments with LaSpec (Laser Spectroscopy of short-lived nuclei). These experiments will address a wide scientific field ranging from nuclear structure and nuclear astrophysics to tests of the weak interaction and of the Standard Model.For the Super-FRS, a stopping cell with an areal density of $20\,\mathrm{mg/cm^2}$ is required, with a cross-section of the stopping volume of $200\,\mathrm{cm^2}$, a high extraction efficiency that is element-independent, an extraction time on the order of 10 ms, and a rate capability of 10^7 ions/s up to a nuclear charge of Z=92. Furthermore, the stopping cell needs to deliver bunches of ions with high purity. No existing stopping cell is capable of reaching these performance characteristics simultaneously. To fulfill these requirements, a novel concept for gas-filled stopping cells has been developed. It is based on the cryogenic stopping cell of the FRS Ion Catcher, and, in addition, it implements the two-stage extraction of the thermalized ions in a direction orthogonal to the incoming ion beam (high-areal-density orthogonal-extraction cryogenic stopping cell, HADO-CSC). This will boost all performance characteristics of the stopping cell and thus remove the performance bottleneck of present stopping cells for the thermalization of exotic nuclei produced at relativistic energies.

1 Introduction and scientific case

The in-flight production of exotic nuclei and their subsequent slowing-down and thermalization combines the advantages of the in-flight and ISOL techniques of universal, element-independent and fast production, high selectivity, and low-emittance secondary beams. It enables high-precision experiments at in-flight facilities, such as trap experiments and collinear laser spectroscopy, that so far have only been available at ISOL and IGISOL facilities. At the Facility for Antiproton and Ion Research (FAIR) in Darmstadt, Germany, such experiments will be possible at the super-conducting fragment separator Super-FRS in Early Science/First Science at the focal plane FHF1 in front of the High-Energy Branch, and at a later stage during First Science++ also at the Low-Energy Branch (LEB) [1–3].

In combination with a high-resolution broadband mass spectrometer, such as a multiple-reflection time of-flight mass spectrometer (MR-TOF-MS) [4], the stopping cell will enable the measurement of masses, branching ratios, e.g., β-delayed (multi-)neutron emission probabilities [5], and lifetimes, as well as the in-cell production of exotic nuclei by multi-nucleon transfer (MNT) with primary and secondary beams [6–8]. These studies will be pursued in the context of the Super-FRS Experiment Collaboration [9], starting in Early Science/First Science. Moreover, the stopping cell can be a tool for the absolute calibration of the particle identification (PID) in the Super-FRS or, alternatively, for a PID that exclusively relies on the mass excess value only [10]. Furthermore, using the combination of accurate mass determination with the PID of the Super-FRS on an event-by-event basis, completely new experimental possibilities will become available, such as the identification of millisecond isomers at the Super-FRS and the measurement of the dependence of the isomer-to-ground-state ratios on the production mechanism [11, 12].

At a later stage during First Science++ at the Low-Energy Branch of the Super-FRS, high-accuracy mass measurements, in-trap conversion electron and alpha spectroscopy, and trap-assisted spectroscopy will be performed with MATS (Precision Measurements of very short-lived nuclei using an Advanced Trapping System for highly

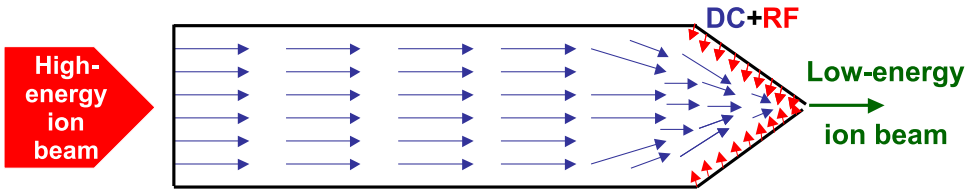

Fig. 1 Schematic figure illustrating the principle of operation of gas-filled stopping cells. A beam of high-energy ions is injected into the stopping cell through a window, slowed down and thermalized by interaction with the buffer gas (typically helium). The ions are then transported to the exit side of the stopping cell using electric DC fields (blue), focused to the center of the exit side of the stopping cell using a combination of electric DC fields and repulsive electric RF fields (red) and extracted with the gas flow through a nozzle

charged ions) [13, 14]. Measurements of nuclear spins, magnetic dipole and electric quadrupole moments, and root-mean-square charge radii will be carried out using collinear laser spectroscopy on ions and atoms and beta-NMR experiments with LaSpec (Laser Spectroscopy of short-lived nuclei) [13, 15]. These experiments will address a wide scientific field ranging from nuclear structure and nuclear astrophysics to tests of the weak interaction and of the Standard Model.

The key requirement for these experiments is the conversion of the secondary beams, which are produced at relativistic energies (up to 1.5 GeV/u) with momentum spreads of a few percent, corresponding to tens of MeV/u, to cooled ions with kinetic energies of a few eV. This will be achieved using the compression of the momentum spread of the beam in the Super-FRS with a monoenergetic degrader system [16–18], further slowing down in a homogeneous degrader and thermalization in a gas-filled stopping cell [19]. Figure 1 illustrates the principle of operation of such a stopping cell. The high-energy ion beam is injected into the stopping cell through a window, slowed down and thermalized by interaction with the stopping gas (typically helium). The ions are then transported to the exit side of the stopping cell using electric DC fields, focused to its center using a combination of electric DC fields and repulsive electric RF fields and extracted with the gas flow through a nozzle. The ions can then be separated from the gas and cooled in an RF quadrupole (RFQ). Here, the transport energy of the ions is about 1 eV. After extraction from the RFQ, the ions can be transferred to experiments downstream of the stopping cell.

The origin of this method is based on the IGISOL technique, which was pioneered at the University of Jyväskylä (Finland) [20, 21]. Stopping cells for short-lived nuclides, which use electric fields for extraction of the ions, were first developed at RIKEN (Tokyo, Japan) [22] and at Argonne National Laboratory (USA) [23, 24]. Further stopping cells of this type have been built at Michigan State University/FRIB (East Lansing, USA) [25, 26], GSI (Darmstadt, Germany) [27, 28], and Maier-Leibnitz-Laboratory (Garching, Germany) [29]. Most of these stopping cells use discrete stainless steel electrodes in the form of a funnel to provide the repelling RF field at the exit side of the stopping cell. The drawback of such RF funnels is that it is extremely challenging to reliably produce large RF funnels with a high density of electrodes, i.e., thin electrodes and fine spacing, as is required to obtain high effective RF fields. Alternatively, an RF structure based on printed circuit boards (PCBs) can be used. Such structures are referred to as RF carpets and can provide ion focusing at higher gas densities than RF funnels [19]. A similar development is RF wire carpets [26]. Stopping cells have been successfully used to thermalize fusion-evaporation and MNT products as well as projectile and fission fragments. They have also been used to stop recoils from fission [30] and α sources [31]. They have enabled impressive experiments, including laser spectroscopy of halo nuclei [32], mass measurements of rp-process nuclei [33] and nuclei at the $N = Z$ line [34], proton-unbound nuclei [35] and super-heavy elements [36, 37], measurements for neutrino physics and tests of standard model [38, 39], and the direct detection of the nuclear clock transition in ^{229}Th [40].

A first step toward the stopping cell for the Super-FRS was taken in 2005 with a large stopping cell with an RF funnel, which was developed at Argonne National Laboratory [23] and tested at the projectile fragment separator FRS [41] at GSI. It demonstrated the capability to thermalize projectile fragments produced at the FRS at relativistic energies, but also suffered from (i) low stopping efficiencies, because the areal density was limited to 2 mg/cm^2, and (ii) intense contamination due to ionization of impurities in the stopping cell [42]. As a result of these tests, a prototype stopping cell for the Super-FRS was developed, which features a much larger areal density due to the use of an RF carpet and a much improved cleanliness due to operation at cryogenic temperatures [43–47]. This stopping cell was commissioned at the FRS as part of the FRS Ion Catcher [5, 45, 47–57] and employed for a large variety of experiments, both, with off-line ion sources [58–62] and on-line in FAIR Phase-0 [8, 53, 63–65].

The performance characteristics of the stopping cell of the Super-FRS will have a strong impact on the range of nuclides available and their yields, since the stopping and extraction efficiencies and extraction times strongly influence the rate of the extracted nuclei and put a limit to their lifetime. Because of the very high kinetic energy of the ions at the Super-FRS and its large acceptance, the demands on the stopping cell of the Super-FRS are particularly challenging: A stopping cell with an areal density of tens of mg/cm^2 is required with a transverse cross-section of the stopping volume of 200 cm^2, a high extraction efficiency that is element-independent, an extraction

time on the order of 10 ms, and a rate capability of 10^7 ions/s up to an atomic number of $Z = 92$. These requirements are not fulfilled by any existing stopping cell worldwide. They also preclude the use of alternative approaches such as a cyclotron gas stopper [66, 67] or a stopping cell that relies on the neutralization of the stopped ions and a selective re-ionization using a laser [68, 69]. Therefore, a novel concept for gas-filled stopping cells has been developed for the Super-FRS [11, 70] based on experience with the two prototype stopping cells that have been tested and operated at the FRS. This concept implements the two-stage extraction of the thermalized ions in a direction orthogonal to the incoming ion beam (high-areal-density orthogonal-extraction cryogenic stopping cell, HADO-CSC). This will boost all performance characteristics of the stopping cell and thus remove the performance bottleneck of present stopping cells for the thermalization of exotic nuclei produced at relativistic energies.

2 Requirements and design goals

2.1 Physical-technical requirements

To determine the design parameters for the stopping cell of the Super-FRS, simulations have been performed using the Monte Carlo simulation program MOCADI [71]. These simulations have focused on the LEB as the most important location of the stopping cell after Early/First Science; however, the results are also indicative for the requirements at the focal plane FHF1 in front of the High-Energy Branch. The ion optical layout of the LEB used in these simulations is shown in Fig. 2. The ions are produced at the entrance of the Super-FRS, separated in the pre-separator and in the main separator. In the LEB, they are dispersed according to their momenta in the three dipole stages at an energy of about 300 MeV/u and energy-bunched using a monoenergetic degrader at the focal plane FLF5. Then, they are re-focused onto the stopping cell located at the focal plane FLF6. Three representative nuclides, ^{78}Ni, ^{132}Sn and ^{220}Pb, were chosen for the simulations. The nuclides ^{78}Ni and ^{132}Sn were produced by projectile fission of ^{238}U on a 0.6 g/cm^2 and a 4 g/cm^2 graphite target and at energies of 700 MeV/u and 1000 MeV/u, respectively, and the nuclide ^{220}Pb was produced by projectile fragmentation of ^{238}U on a 4 g/cm^2 target at an energy of 1000 MeV/u. A beam spot on the target was assumed with standard deviations for position and angle in the dispersive direction of $\sigma_x = 1$ mm and $\sigma_a = 4$ mrad, respectively, and position and angle in the non-dispersive direction of $\sigma_y = 2$ mm and $\sigma_b = 2$ mrad, respectively. All slits were open to their maximum position (±200 mm in the dispersive direction).

Figure 3 shows the range distributions in the helium gas of a stopping cell at FLF6. The full width at half maximum (FWHM) of the distribution amounts to 7 mg/cm^2 for ^{220}Pb, 17 mg/cm^2 for ^{132}Sn and 29 mg/cm^2 for ^{78}Ni. The width of the distribution decreases with increasing atomic number of the fragment. Matter inhomogeneities and energy-loss straggling due to atomic charge exchange [17] were not taken into account in the simulations. They are expected to amount to about 5 mg/cm^2 in helium (standard deviation), which is in agreement with a recent measurement of the minimum range distribution of ^{238}U ions performed at the FRS [72]. This will significantly increase the expected width of the range distribution for ^{220}Pb, but will have only a minor

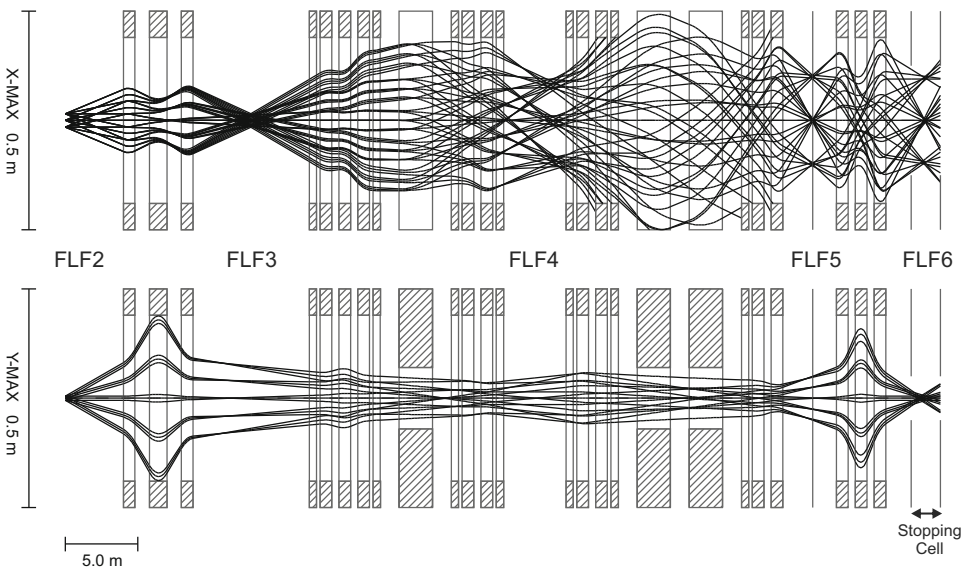

Fig. 2 Ion optical layout of the LEB of the Super-FRS. The positions of the focal planes FLF2 to FLF6 are indicated as well as the length of the stopping cell at FLF6

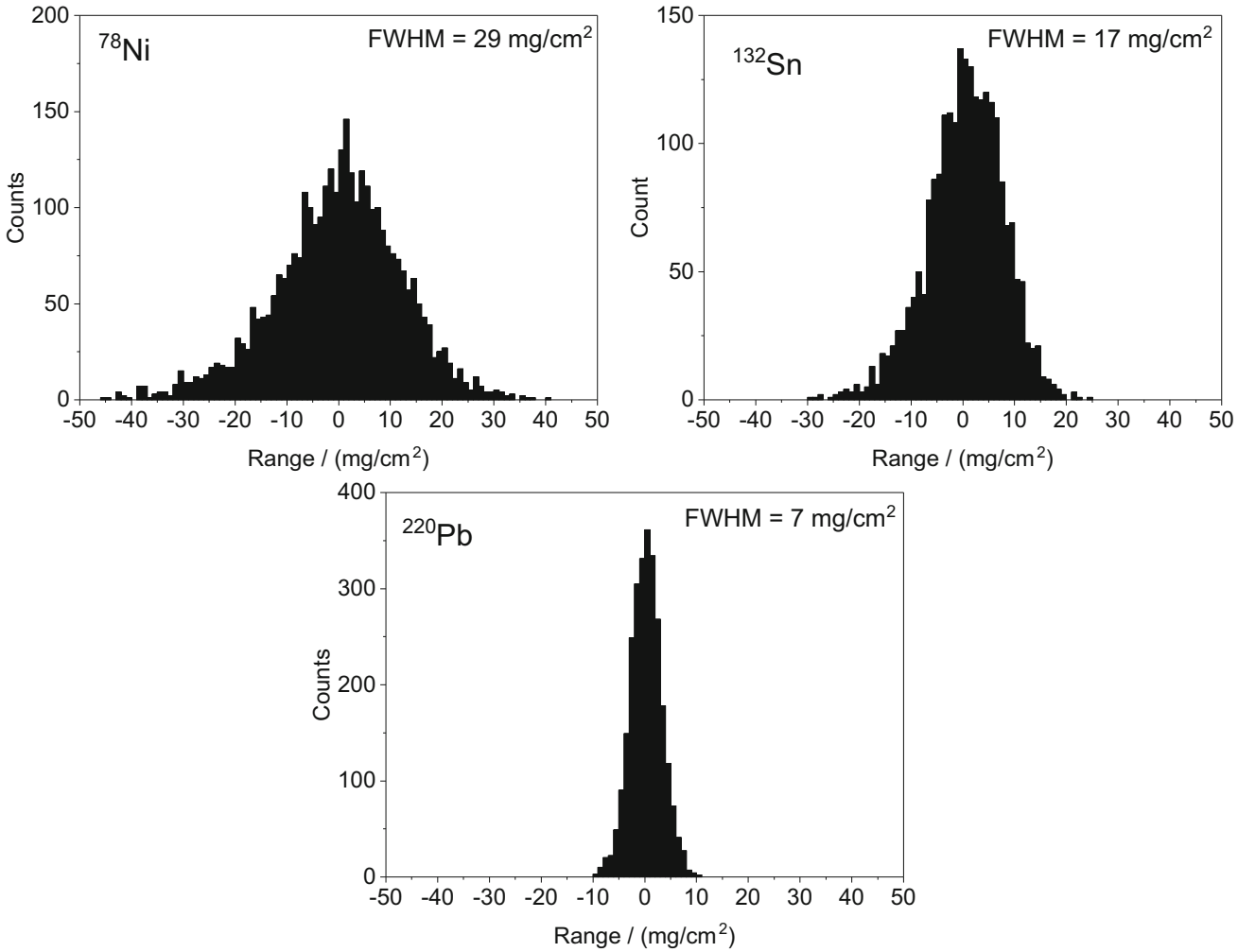

Fig. 3 Simulated range distributions in helium for the nuclides ^{78}Ni, ^{132}Sn and ^{220}Pb in the stopping cell at FLF6

influence on the width for ^{78}Ni. Because of the inevitable matter inhomogeneities, for heavy and medium–heavy fragments operation with a lower primary beam energy will not significantly reduce the overall range straggling. Rather, the advantages of the high primary beam energy at FAIR, such as larger yields due to thick targets, high transmission efficiency, and clean separation far outweigh the small gains in stopping efficiency due to slightly smaller range straggling. Therefore, the stopping cell needs to be designed for these high primary beam energies. Overall, an areal density of the stopping cell of at least 20 mg/cm^2 is required for efficient stopping. Considering a length of 2 m to be the maximum length of a stopping volume that is practically feasible and can be built and operated with reasonable effort, a stopping gas density of 100 μg/cm^3 is thus required.

Figure 4 shows the size of the beam spot at the position of the stopping cell at FLF6 averaged over the length of the stopping volume of 2 m. The FWHM of the beam spots amounts to about 150 mm in the horizontal direction for all three nuclides and from 55 mm for ^{220}Pb to 118 mm for ^{78}Ni in the vertical direction. A stopping volume with a cross-section (active area) of 200 mm × 100 mm will thus allow most of the fragments to be contained transversally in the stopping cell.

Furthermore, it is desirable that the extraction efficiency of the ions from the stopping cell is high. This efficiency includes the survival probability of the ions during the thermalization process and their transport through the stopping cell in a charged state (i.e., neutralization in the stopping gas must be avoided) as well as the transport efficiency along the focusing RF structure at the exit side of the stopping cell and out of the stopping cell. From experiments with the prototype of the stopping cell of the Super-FRS, an extraction efficiency of at least 50% seems to be feasible [45, 47]. To retain the advantage of the universality of the in-flight isotope production technique, this efficiency should be achievable for ions of most elements. While the interaction of the thermalized fragments with the stopping gas will always depend on the chemical properties of the ions, such a dependence should be reduced as much as possible by choice of the buffer gas and its cleanliness. The ions of interest should be extracted preferably

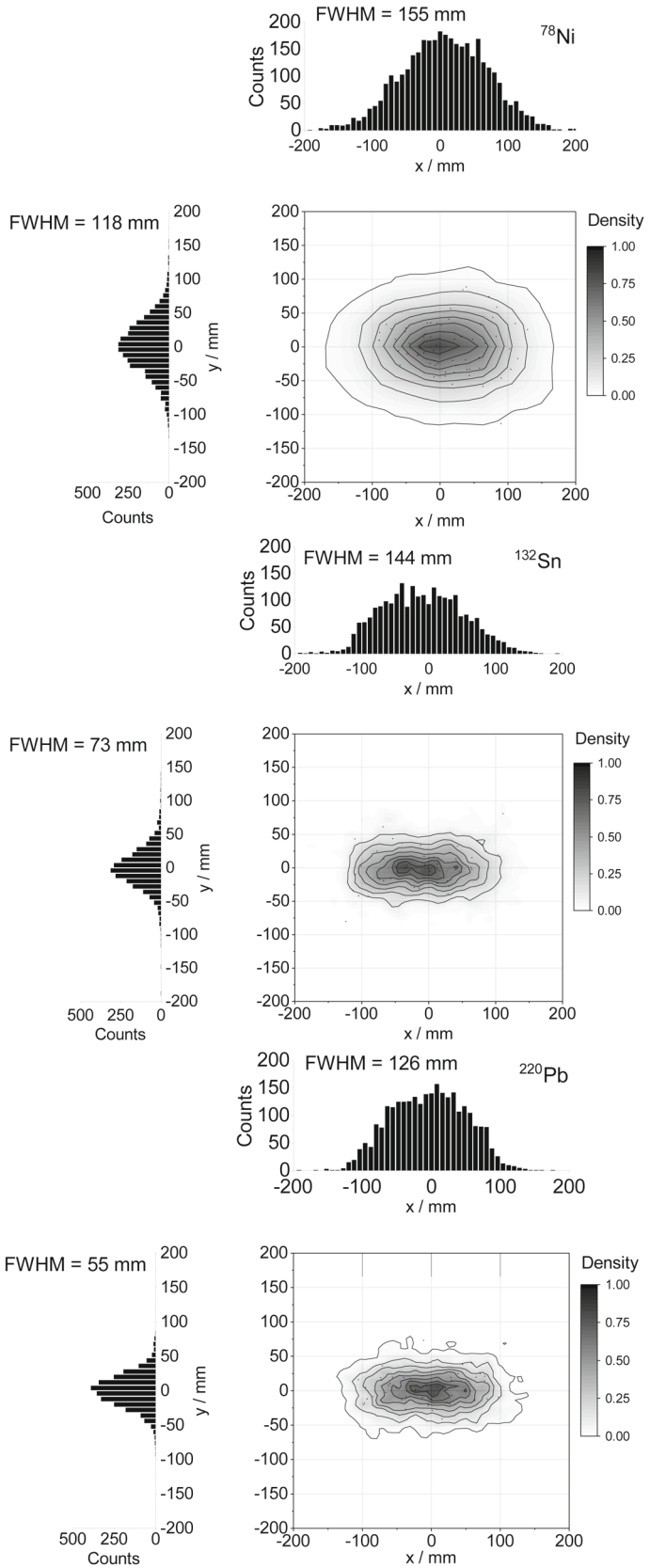

Fig. 4 Simulated beam spots for the nuclides ^{78}Ni, ^{132}Sn and ^{220}Pb in the stopping cell at FLF6

as atomic ions without adducts. The beam of ions extracted from the stopping cell should also be sufficiently pure (see also Sect. 2.3).

The rates required for the different experiments, which will employ the stopping cell, cover a large range. While typical experiments with MATS will only require low rates for the ion of interest on the order of 1 ion/s or less, rates required for LaSpec are expected to lie in the range from 10/s to 10^4/s. Furthermore, for MNT reaction studies to be performed in the context of the Super-FRS Experiment Collaboration, a rate capability of ions impinging on the stopping cell as high as possible is desired.

The rate capability of the stopping cell needs to be significantly higher than the rates required at the experimental stations of MATS and LaSpec. There are several reasons for this. First, the beam delivered from the Super-FRS may also contain other fragments than the one of interest. Depending on their range, these ions may also fly through the CSC and create ionization, even if they are not stopped. They therefore have to be included in the overall rate. In unfavorable cases, such as fission fragments, the ratio of the rate of the ions of interest to the overall rate can amount to only about 1%. Second, some of the ions of interest fragment in the degrader in front of the stopping cell; they also pass through the stopping cell and create ionization. Finally, both, the limited stopping, ion survival and extraction efficiency of the stopping cell and the limited transmission efficiency from the stopping cell to the experimental stations need to be taken into account, i.e., a higher intensity of the beam entering the stopping cell is required to compensate the transmission losses downstream of the device. Assuming losses by fragmentation in the final slowing-down in front of the stopping cell of 30%, a combined stopping and extraction efficiency of the stopping cell of 50%, and a transport efficiency from the stopping cell to MATS and LaSpec of 50%, this results in an overall rate of ions impinging on the stopping cell of 6×10^3/s to 6×10^6/s. Therefore, a maximum rate of about 10^7/s is aimed for with the stopping cell. This is compatible with the maximum rate foreseen for the LEB hall of 10^7 ions/s for elements up to uranium. Secondary beams with such high rates will be readily available at the Super-FRS, albeit not for the most exotic species.

An additional requirement is that the extraction time of the ions from the stopping cell is reasonably fast, since it would otherwise put a limit on the lifetime of the ions that can be measured. Thus, it is desirable that the extraction time is not much longer than the typical cooling and preparation times for ions in ion traps, which are on the order of 10 ms, see, e.g., [73, 74]. The Super-FRS will deliver exotic nuclei located at or beyond the drip lines with shorter lifetimes, but most nuclei produced at the Super-FRS with rates sufficient for experiments with MATS and LaSpec will have half-lives that are of this order or longer [75].

Further design goals concerning the detectors and the degrader located at the final focal plane FLF6 in front of the stopping cell and the beamline from the stopping cell to MATS and LaSpec are addressed in Sects. 6.7 and 2.3, respectively. To allow for other experimental setups at FLF6, it must be possible to remove the stopping cell from its location at FLF6.

In summary, the design goals for the stopping cell of the Super-FRS can be specified as follows:

- Areal density: $\geq 20\,\mathrm{mg/cm^2}$
- Extraction efficiency: $\geq 50\%$, preferably for ions of most elements
- Extraction time: $\sim 10\,\mathrm{ms}$
- Rate capability: $\geq 10^7$ ions/s up to atomic number of $Z = 92$
- Active area: $200\,\mathrm{mm} \times 100\,\mathrm{mm}$ (width $\times$ height).

2.2 Discussion of the requirements and challenges

The design of a stopping cell as described in Fig. 1, which can operate at areal densities of 20 $\mathrm{mg/cm^2}$ or more, at rates up to 10^7 ions/s and with extraction times on the order of 10 ms, is far from trivial. First, the effective repelling field of the RF structure needs to be strong enough to compensate the DC field (push field), which drives the ions to the exit side of the stopping cell, and to avoid ion losses at the RF structure. The strength of the effective field decreases with increasing gas density, such that the achievable gas density is limited. The effective field of the RF structure is given approximately by [22]

$$E_{\mathrm{eff}} = \frac{1}{2}\left(\frac{m}{q}\right) K_0^2 \left(\frac{n_0}{n}\right)^2 \frac{V_{\mathrm{rf}}^2}{r_0^3}, \tag{1}$$

where m/q is the mass-to-charge ratio and K_0 the reduced mobility of the ion, n the density of the stopping gas and n_0 the gas density at the standard temperature $T_0 = 273.15\,\mathrm{K}$ and standard pressure $p_0 = 1013.25\,\mathrm{mbar}$, V_{rf} the amplitude of the RF voltage applied to the RF structure and r_0 half the distance between the centers of neighboring RF electrodes. The RF amplitude is limited because of discharges at the RF structure. Typically, this limit lies in the broad minimum of the Paschen curve [76, 77] and is therefore almost independent of the

structure size and the density. It amounts to about 150 V (peak-to-peak). To achieve a high gas density n for a given effective field, the structure size r_0 needs to be reduced. RF structures with discrete metal electrodes are, however, typically limited to a density of about two electrodes per millimeter or less. An increase in the areal density of the stopping cell then requires a stopping cell with a length of many meters.

Second, the velocity v of an ion in the stopping gas is determined by the mobility and the electric field strength E along the extraction path

$$v = K_0\left(\frac{n_0}{n}\right)E. \tag{2}$$

A short extraction time therefore requires a short extraction path of the ions in the stopping cell, i.e., typically a short stopping cell, and a high field strength along this path. For example, a heavier singly or doubly charged atomic cation in helium gas has a reduced mobility of about $17.5\,\mathrm{cm}^2/(\mathrm{Vs})$ [78]. It thus requires 50 ms to drift through a distance of 1 m in helium at a pressure of 100 mbar and a temperature of 300 K under the influence of an electric field with a strength of 10 V/cm. A high field strength, however, needs to be compensated by a strong effective repelling field at the RF structure, which is limited by the reasons explained above. Furthermore, in stopping cells with long extraction paths and strong axial fields, high voltages arise, which may also result in discharges at the electrodes or at the electrical feedthroughs. Here, the situation is, however, more advantageous, since in contrast to the sub-millimeter distances of RF structures, the conditions for the electrode structures that create the axial electric field are characterized by distances of several centimeters and thus correspond to the part of the Paschen curve, where the breakdown voltage increases with density.

Third, the operation of stopping cells with high beam intensities is a challenge [79–85]. Heavy ions that are slowed down and thermalized in helium lose their energy mainly due to ionization and excitation of the helium atoms. Each heavy ion stopped in helium with an areal density of $10\,\mathrm{mg/cm}^2$ creates about 10^7 He–electron pairs [86]. At 10^7 ions/s, the overall ionization rate amounts to 10^{14} He–electron pairs/s. Due to their high mobility, the electrons are quickly removed from the stopping cell by the extraction field, leaving a region with strong positive charge. Consequently, space-charge effects arise in the stopping cell, which may lead to severe ion losses. At even higher ionization rates, a region of plasma is created in the stopping cell. The plasma compensates the external electric fields, such that the ions are trapped and lost due to recombination processes. This loss in efficiency is particularly harmful if the ions of interest are produced with orders of magnitude lower rates as compared to the contaminants. To counteract the space-charge and plasma effects and thus to achieve a high rate capability, short extraction paths and high field strengths are required.

Clearly, these three goals partially contradict each other, and it is very difficult to reconcile these contradicting requirements. Possible solutions that will be implemented in the design of the stopping cell of the Super-FRS are discussed in Sect. 4.

The survival efficiency of the ions in the stopping cell and the purity of the extracted ion population are limited by the cleanliness of the stopping gas [47]. Helium is an ideal stopping gas because of its chemical inertness and its high ionization potential. In a stopping cell filled with pure helium, the ions are thermalized in a charge state of 1+, 2+, or 3+, depending on their ionization potential, and ion losses due to neutralization are minimized. Figure 5 shows the charge states, in which ions of a certain element are expected to be extracted from a stopping cell, if only helium atoms are present in the stopping volume. It shows that about 10% of all elements will be extracted in a 1+ charge state, 60% in a 2+ charge state, and 30% in a 3+ charge state. Furthermore, in pure helium, the ions will not form molecules with the stopping gas. The situation changes drastically if contaminants, e.g., hydrocarbons, which may have much lower ionization potentials, are present in the stopping cell. Then, ions of many elements will be neutralized during their extraction from the stopping cell. Therefore, ultra-pure stopping gases are needed for an efficient operation of a stopping cell. Simulations show that in a stopping cell with an areal density of $10\,\mathrm{mg/cm}^2$ a contamination of at most a few parts-per-billion (ppb, 10^{-9}) can be tolerated if ion survival efficiencies of more than 70% should be achieved [47].

A pure stopping gas is also needed to obtain a good purity of the extracted ion population. Because of the high ionization potential of helium, stopping gas atoms that have been ionized during the stopping process of the projectiles will charge exchange with all contaminant gases in the stopping gas. The contaminant ions are extracted together with the ions of interest, and may hamper the measurement if they are much more abundant than the ions of interest. The ions of interest and the ionized stopping gas atoms have similar mobilities and trajectories in the stopping volume. Therefore, similar purity requirements apply for the purity of the extracted ion population as for the survival of the ions of interest in the stopping cell.

A drawback of using pure helium as stopping gas is a weakening of the effective field of the RF structure due to the higher charge states of the ions. As can be seen from Eq. (1), the magnitude of the effective field is inversely proportional to the charge of the ion. For an ion in a 3+ charge state, the attainable stopping gas density is hence smaller by a factor of $\sqrt{3}$ than that of an ion in a 1+ charge state. It may therefore be advantageous to operate with a stopping gas with very high purity, but to allow for a small fraction of an additional gas with a lower ionization potential, such as argon, krypton, xenon, oxygen, or nitrogen monoxide, which is introduced intentionally to the

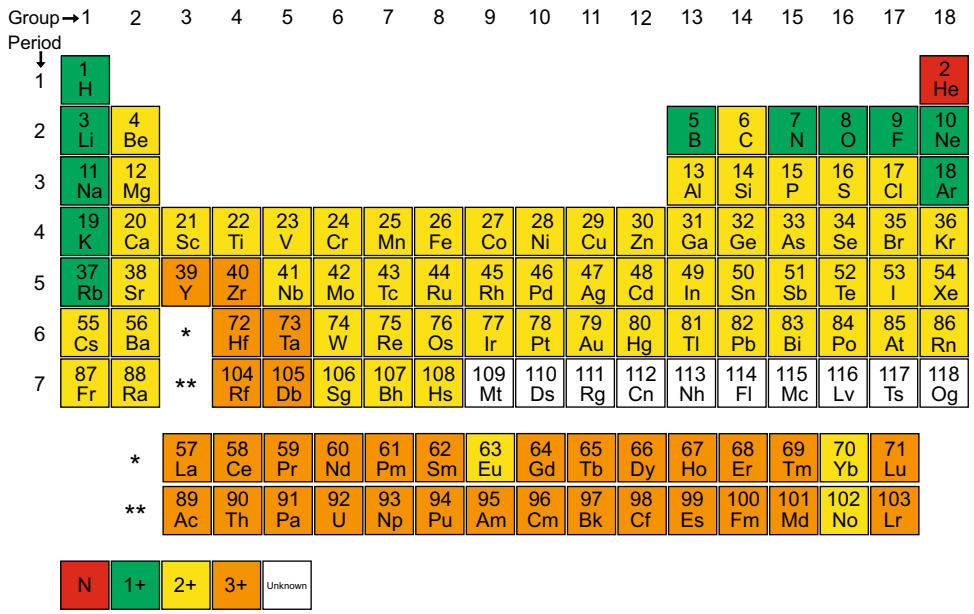

Fig. 5 Estimated charge states of elements extracted from a stopping cell using pure helium as stopping gas. The charge state is derived from the first, second, and third ionization potential of each element in comparison with the ionization potential of helium of 24.6 eV. The ionization data were taken from the NIST database [87]

stopping cell as a charge exchange gas to reduce the charge state of the ions to 1+ or 2+. The charge exchange gas needs to be chosen, such that it does not form molecules with the ions of interest, or that molecules formed from the gas can readily be broken up again or can otherwise be removed.

Reaching a stopping-gas cleanliness on the ppb level is a challenge, because the stopping volume can be pumped only during an initial cleaning period. For operation, the stopping cell is filled with the stopping gas and the vacuum pumps need to be separated from the chamber. No additional pumping can be applied to the stopping volume and contaminants, evaporating from the walls of the chamber, are no longer removed.

Different solutions are used to reach the required cleanliness goals. The strict usage of UHV materials, such as stainless steel and ceramics, is one approach [27]. In this case, the stopping cell is baked at high temperatures before operation and contaminants are removed from the stopping volume before operation. This approach has the disadvantage that it strongly limits the range of materials that may be used in the stopping cell. In particular, electronic components may not be used inside the stopping cell, and only ceramics may be used as insulators. This can lead to complex and sometimes fragile mechanical constructions and poses a strong limitation for the design of the electronic circuitry in the stopping cell.

A different approach is to clean the stopping gas by cryo-sorption [88, 89]. In this case, the stopping cell is cooled down to a low temperature and the impurities freeze out on the walls of the stopping cell chamber. Such a cryogenic stopping cell (CSC) allows a wide choice of materials and can be constructed more easily. When cooling down the stopping cell, the vapor pressure of impurities is reduced, e.g., for CO_2 at 100 K the vapor pressure amounts to 10^{-3} mbar and can be reduced to below 10^{-11} mbar at 65 K. At about 70 K the vapor pressures of most impurities are reduced to the level of 10^{-9} mbar [90]. In a cryogenic stopping cell under operating conditions, cryo-sorption takes place and the helium stopping gas is purified constantly. However, the pumping speed of the cold surface is reduced once an initial monolayer is absorbed. This means that the residual gas pressure inside the stopping volume before starting the cooling needs to be sufficiently low, in order not to reach the limit of one monolayer.

In addition to the cleanliness of the stopping cell, the purity of the stopping gas needs to be considered, which is introduced to the stopping cell to replenish the stopping gas that flows out from the extraction nozzle. Since helium gas with a purity at the ppb level is not available commercially, an additional gas purification is required before feeding the gas to the stopping volume.

2.3 Discussion of the beam transport to MATS and LaSpec

The ion transport from the stopping cell to MATS and LaSpec will be performed with an electrostatic low-energy beamline. In the MATS-LaSpec hall, the beam will be cooled and bunched in a dedicated RFQ cooler and buncher [91], before it is delivered to either MATS or LaSpec [13]. The transport energy of the ions and the electric potentials of the stopping cell, the beamline, and the experimental setups of MATS and LaSpec are important design choices. Different concepts were considered and discussed [92]. The requirements for the choice of the transport scheme are to deliver a well-controlled bunch of ions of interest produced in the Super-FRS with highest efficiency, purity and reliability. There is no priority ordering of the requirements, since it would easily

compromise measurements proposed by and expected from MATS and LaSpec if one condition were fulfilled and others are not.

One approach is to place the stopping cell and the experimental stations on a high-voltage platform and to keep the beamline at ground potential, such that the ions have a transport energy in the beamline equivalent to the high voltage. Another solution is to keep the stopping cell and the experimental stations at ground potential and to have the beamline at a (negative) high voltage. Yet, another solution is to keep the stopping cell, the experimental stations, and the beamline at ground potential and to accelerate the ions behind the stopping cell with the help of a pulsed drift tube [93–95] and to retard the ions in front of the experimental stations with a second pulsed drift tube. Furthermore, a mixture of the approaches can be used, placing either the stopping cell or the experimental stations on a high voltage and keeping the other at ground in combination with a pulsed drift tube.

For such a low-energy beamline, transport energies in the range from several keV/charge to several 10 keV/charge are used. If a dipole magnet is needed to remove intense contaminants with currents on the order of $\sim \mu$A from the beam, a transport energy of several 10 keV/charge is desirable to reduce the emittance of the beam, in particular under space-charge conditions. However, for the LEB of the Super-FRS, such conditions are not to be expected, since the Super-FRS will supply secondary beams with high purity and since the formation of strong molecular contaminants in the stopping cell can be suppressed by adequate cleanliness of the stopping cell (cf. Sects. 2.2 and 3.2.3). In this case, mass separation can be performed in the extraction RFQ system of the stopping cell and for the ion transport in the beamline an energy of a few keV/charge is sufficient.

In addition, there are some requirements driven by LaSpec. The beam for LaSpec needs to have low emittance, it must be bunched to a few microseconds, and the energy has to be variable in a certain range of several 10 keV. Presently, the most successful schemes that deliver those conditions use an RFQ cooler and buncher on a high-voltage platform with a potential of 40 to 60 kV. The control of the potential on this platform defines the achievable precision and hence needs a special attention. However, the development of a laser–ion-beam interaction region raised or lowered not by a few kV only but rather by a few 10 kV would allow in addition the RFQ cooler and buncher for MATS and LaSpec to be operated close to ground potential. This kind of interaction zone has not been used or developed yet; however, the LaSpec collaboration is confident that this is possible. The option of having MATS on HV seems not appropriate because of the central issues with voltage stability and noise for precision measurements and single-ion detection.

It is difficult to estimate the expected reliability along with the ease of operation and hence the projected availability of beam from the different possible schemes. This can only be based on experience with present setups, but projection to future solutions is difficult, since improvements on the known weaknesses are to be sought. Generally, it is safe to claim that a simpler system will be superior concerning ease of operation and reliability. The aim should, therefore, be to reduce the technical complexity wherever possible and to avoid technically challenging solutions. Many technical challenges are connected to a large stopping cell, which needs to be movable to allow for other experimental setups at FLF6. Operating the stopping cell on a high-voltage platform certainly adds more complexity and complication. Another technical complication that should be avoided is connected to the beamline operated completely, with pumps, diagnostics, vacuum controls, on high voltage—the higher the more complicated.

Pulsed drift tubes with large voltage difference (> 10 kV) are known to be challenging for operation at high transmission efficiency. However, pulsed drift tubes with smaller voltage differences seem to be feasible.

To devise a transport scheme that best reflects the considerations discussed above, the following assumptions are made:

- The stopping cell produces a microsecond bunch of less than 10^6 ions in total.

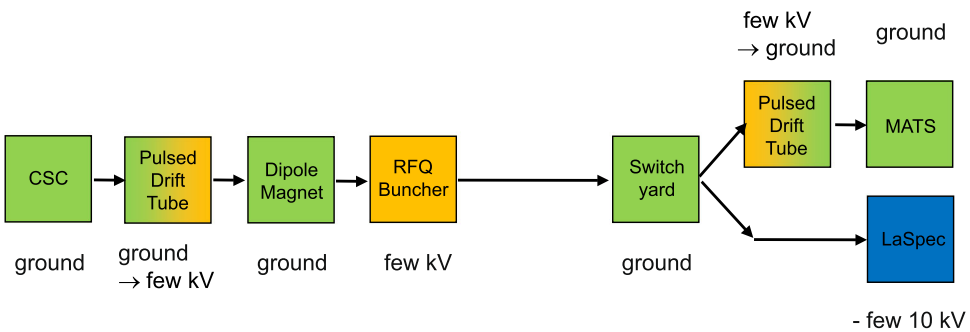

Fig. 6 Schematic figure of the beamline from the stopping cell to MATS and LaSpec. The operating potential of the individual setups is indicated using different colors: ground potential (green), positive potential of a few kV (orange), and negative potential of a few 10 kV (blue)

- The ions of interest should typically be the most abundant component for bunches with more than about 10^2 ions.
- The laser–ion–beam interaction region and/or the charge-exchange cell used by LaSpec can be operated at a potential of a few 10 kV.
- An efficient switching of low-energy (keV) ion bunches in pulsed drift tubes is available.

Based on these assumptions, the transport scheme shown in Fig. 6 has been chosen as the most reasonable solution. It allows for operation of the stopping cell, MATS, and the beamline at ground potential. The transport energy of about 5 keV/charge in the beamline is achieved using a pulsed drift tube behind the stopping cell. The beam is retarded in front of MATS using a second pulsed drift tube. A dipole magnet in the beamline is foreseen, but used mainly as a bending device.

This concept has been discussed within the MATS and LaSpec collaborations, has been agreed upon, and is reflected in the design choices presented in this document.

3 Prototype results

The feasibility of thermalizing projectile and fission fragments produced at relativistic energies (up to 1000 MeV/u) in a gas-filled stopping cell was demonstrated with two generations of stopping cells at the projectile fragment separator FRS [41] at GSI as part of the FRS Ion Catcher [42, 48, 53]. Furthermore, the concepts and technical developments for the stopping cell of the Super-FRS were tested using these prototypes, and first experiments targeting mass measurements of exotic nuclei were performed. Based on the results, the technical design of the stopping cell of the Super-FRS has been developed. These tests and developments are described in the following.

3.1 First generation: room-temperature stopping cell with RF funnel

3.1.1 Stopping cell

The first generation stopping cell was developed at Argonne National Laboratory [23, 96]. It has a stopping volume with an inner diameter of 250 mm and a length of 1.25 m. Concentric electrodes, which also form the body of the stopping cell, create an axial electric DC field that guides the ions to the exit side of the stopping cell. An RF funnel with electrodes with a thickness of 0.43 mm and a spacing of 0.38 mm focuses the ions onto the exit nozzle that has a diameter of 1.6 mm. The stopping cell has an entrance window with a width of 250 mm and a height of 30 mm in the vertical direction covered by a 100 µm titanium foil. The stopping cell consists of more than 7400 components, of which more than 4000 are prepared for ultra-high vacuum conditions. The stopping cell is operated at room temperature, and indium seals in the stopping cell limit the bake-out temperature to about 340 K. The stopping cell can be pumped out through a port with a diameter of 3 cm. The base pressure reached inside the cell after bake-out amounts to about 10^{-7} mbar.

3.1.2 Experiment

The stopping cell was tested in 2005 at the FRS [42]. Figure 7 shows the setup. Helium was used as stopping gas. It was introduced into the stopping cell through a gas purification system consisting of a cold trap to freeze out contaminants and a commercially available purifier (Mono-Torr). The exit side of the stopping cell was connected to an RFQ, which was pumped by a large roots-blower pump with a pumping speed of 5000 m^3/h. Behind the extraction RFQ, the ions could be guided to a silicon detector or, alternatively, to a time-of-flight mass spectrometer with orthogonal acceleration (Ortho-TOF-MS) [97] using an RFQ-based distribution system [98]. The silicon detector served for counting of the β decays of the extracted radioactive ions. The Ortho-TOF-MS is a broadband mass spectrometer with a mass resolving power of 10^4 and thus allows for the detection and identification of all ions, including contaminant ions formed in the stopping cell.

A ^{58}Ni primary beam with an energy of 300 MeV/u was transported through the first half of the FRS and fragmented in a 2.5 g/cm^2 aluminum target in the mid-plane of the FRS. The projectile fragments were dispersed according to their momentum in the second half of the FRS and energy-focused using a monoenergetic degrader system at the exit of the FRS. The selection of fragments with $A/Z = 2$ led to almost monoenergetic secondary beams with almost identical mean velocities (corresponding to about 260 MeV/u) at the exit of the FRS. The various fragments with $N = Z$ (^{56}Ni, ^{54}Co, etc.) have different mean ranges. Due to the energy focusing, the range differences exceed the width of the range straggling. This imposes a longitudinal separation and thus, varying the degrader thickness, allows to stop an isotopically pure beam in the stopping cell. Ion rates were measured in a multiple-sampling ionization chamber (MUSIC), while three scintillators in front of the stopping cell determined

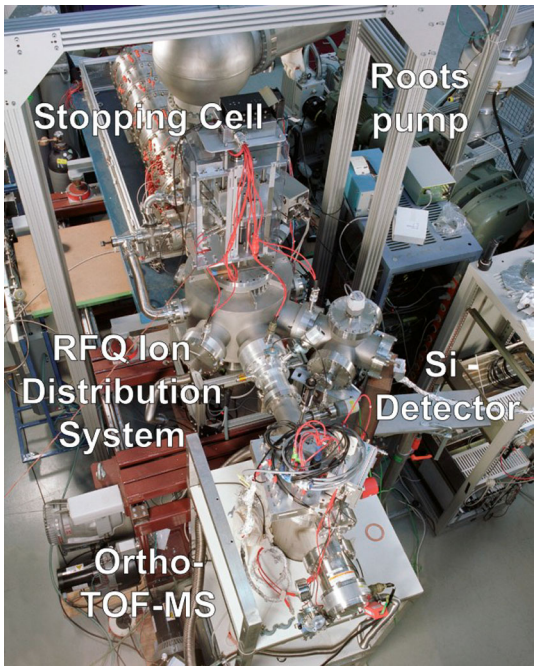

Fig. 7 On-line test of the first generation stopping cell at the FRS. Photograph of the setup consisting of stopping cell, roots pump, RFQ ion distribution system, Ortho-TOF mas spectrometer, and silicon detector

the vertical distribution of the ions. In the experiment, the stopping cell was operated successfully at a helium pressure of up to 100 mbar, corresponding to an areal density of 2.3 mg/cm^2. Extraction field strengths of 3.5 V/cm up to 7 V/cm were applied and an RF voltage of 145 V (peak-to-peak) at a frequency of 900 kHz was used in the RF funnel.

3.1.3 Results

Using a variation in the wedge angle of the degrader, a minimum range distribution of the fragments inside the stopping cell with a standard deviation of 15 mg/cm^2 glass equivalent could be achieved. The overall efficiency as given by the ratio of ^{54}Co ions on the silicon detector to the number of ^{54}Co measured in the MUSIC detector in front of the stopping cell was $(1.8 \pm 0.3)\%$. To determine the extraction efficiency of the stopping cell, the measured overall efficiency can be divided into a stopping efficiency, an extraction efficiency, and a transport efficiency through the RFQ system. The stopping efficiency was calculated from the measured range distribution to be $(5.0 \pm 1.1)\%$. The extraction and transport efficiency is given by the ratio of overall efficiency and stopping efficiency and amounted to $(35.8 \pm 9.4)\%$. This value also includes the transport efficiency through the RFQ system to the detector, which was estimated as $(75 \pm 25)\%$. The extraction efficiency thus amounted to about 45%.

A small leakage in the gas cell occurred during the setup of the experiment, which could not be fixed in time. During the experiment, abundant contamination of ions from water clusters and hydrocarbons formed in the stopping cell was observed with the Ortho-TOF-MS, which made detection of the radioactive ions in the mass spectrometer impossible. From extraction time measurements of polyatomic ions formed in the stopping cell, extraction times of atomic ions in the range of 20 ms to 50 ms could be derived. The potential of the system was illustrated by the half-life measurement of ^{54}Co with a short half-life of 193 ms only.

The experiment successfully demonstrated the range bunching of projectile fragments produced at the FRS at relativistic energies, their thermalization, and efficient extraction. However, two limitations of the stopping cell also became apparent: (i) Because of the use of an RF funnel with a density of only about 1.2 electrodes/mm, the areal density was limited to about 2 mg/cm^2. This limits the stopping efficiency for projectile and fission fragments to a few percent. (ii) The cleanliness of the stopping cell was not high enough to extract a sufficiently clean ion population from the stopping cell. The residual gas pressure of 10^{-7} mbar in the stopping cell after bake-out corresponds to a purity of 1 ppb after filling the stopping cell with 100 mbar of helium for operation. However, during operation, the pumping port must be closed and further pumping of the stopping cell is not possible. Therefore, during operation of the stopping cell, the purity is much worse (see, e.g., [27]) and would not have been sufficient even without the small leak in the stopping cell that occurred during the experiment. These issues were addressed in the second-generation stopping cell at the FRS.

3.2 Second generation: cryogenic stopping cell with RF carpet

3.2.1 Stopping cell

Based on the experience with the first generation stopping cell, a second-generation stopping cell was developed, which addresses the shortcomings of the previous device [43–47]. Its key innovative features are operation at high gas densities and cryogenic temperature [88, 89]. It was the first stopping cell of this type to be constructed, commissioned, and used for experiments. The CSC was developed in a collaboration between KVI-CART/University of Groningen (The Netherlands), Justus Liebig University Gießen (Germany), and GSI. Its design was guided by extensive simulations [44, 99]. After the commissioning, the device was improved continuously [47, 48, 53, 100–104].

The CSC is shown schematically in Fig. 8. An outer vacuum chamber provides the insulation vacuum for the cold inner chamber. A beam of high-energy ions enters the stopping volume in the inner chamber through three thin windows and is stopped in the helium stopping gas. The stopping volume has a length of 104.5 cm and a diameter of 25 cm and is formed by a DC electrode structure (DC cage) and an RF carpet at the exit side of the CSC. The thermalized ions are drawn by the DC field created by the cage to the exit side, focused onto an exit nozzle in the center of the RF carpet, extracted from the CSC with the gas flow, and separated from the stopping gas in an extraction RFQ.

Both vacuum chambers are built from stainless steel. The outer chamber has a length of 140 cm and a diameter of 66 cm and the inner chamber a length of 120 cm and a diameter of 46 cm. The inner chamber is supported against the inside of the outer chamber by ball bearing supports. Both chambers have a rectangular opening of 250 mm by 100 mm on the entrance side, which is covered by a stainless steel window with a thickness of 100 µm. The cylindrical part of the inner chamber is covered by a thin stainless steel sheet, which was welded and blown at high pressure, resulting in cooling channel winding around it. The channels are connected via stainless steel tubes to cryogenic feedthroughs, where the cooling system is connected. The cooling system consists of a cryo-cooler (Leybold Coolpower 140 T) with a cooling power of 140 W at 80 K and a cryo-fan. The cryo-fan circulates the cooling medium (high-pressure helium gas) in a closed circuit from the cold head of the cryo-cooler to the cold chamber of the CSC. A pre-cooler using liquid nitrogen allows to pre-cool the cooling medium before reaching the cold head and thus increases the cooling power of the system. Temperature tuning of the CSC can be done using a line that bypasses the cold head. Radiation heat losses are minimized by wrapping the cold chamber in super-insulation. Before cool-down, the CSC can be baked to a temperature of 420 K using heating bands wrapped around the inner chamber. The heating bands also allow for a fast warming-up of the stopping cell for maintenance. Temperature sensors placed on all important elements of the CSC allow monitoring of the cool-down and operation of the CSC. After a cool-down time of typically 24 h the CSC is ready for operation. The walls of the inner chamber reach a lowest temperature of 50 K, the stopping gas about 75 K. If the RF voltage of the RF carpet is turned on, the RF carpet, in particular the coil of the RF circuit, heats up by several 10 K, depending on the amplitude of the RF voltage and the stopping gas density.

The outer vacuum chamber of the CSC is pumped by a turbomolecular pump to pressures below 10^{-7} mbar. The inner chamber is pumped through a pumping port by a turbomolecular pump. During normal operation of the CSC with stopping gas, the pump port is closed using a cryogenic valve. At room temperature, the stopping volume can be evacuated down to a pressure of 6×10^{-6} mbar. After cool-down, the pressure in the stopping region

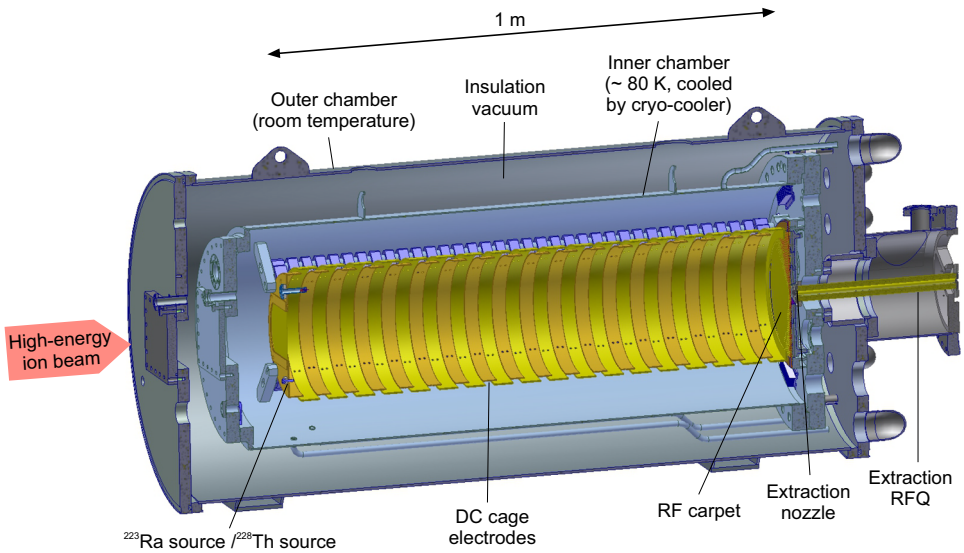

Fig. 8 Schematic figure of the prototype CSC. For details, see text

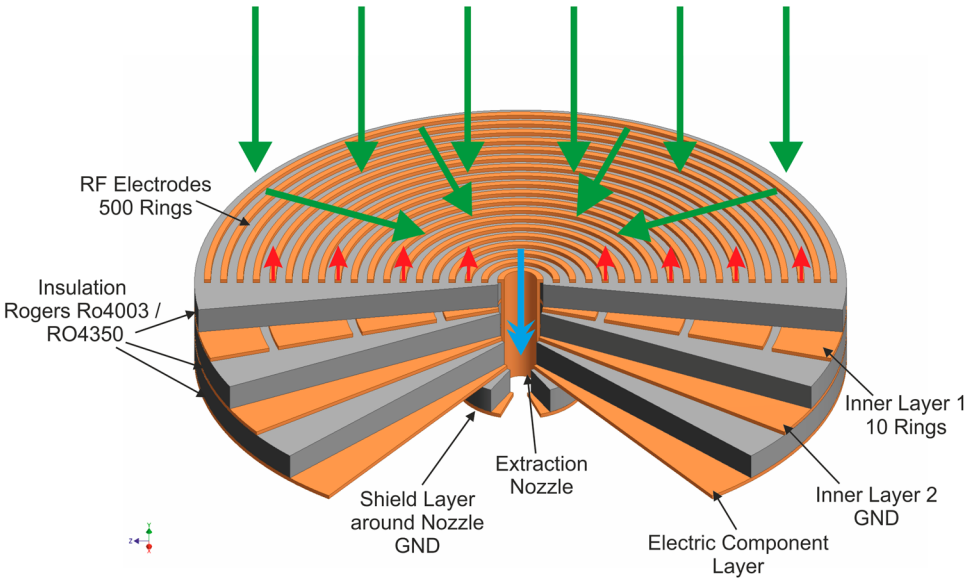

Fig. 9 Schematic figure showing the layout of the RF carpet of the prototype CSC. The forces acting on the ions resulting from the DC field (green), the effective RF field (red), and the gas flow (blue) are indicated

typically amounts to 4×10^{-8} mbar with the pump port open and to 2×10^{-7} mbar with the pump port closed. Under these conditions, the residual gas spectrum is dominated by N_2. Assuming no impurities are added to the system by the helium gas supply, this corresponds to a cleanliness at the 5 ppb level at a stopping gas pressure of 50 mbar. Before the helium stopping gas is introduced into the CSC, it is purified using a purification getter (SAES MicroTorr MC400-902V) and optionally in a cold trap cooled by liquid nitrogen. Then, it is pre-cooled in a heat exchanger, which is coupled to the cooling circuit, and fed into the cold chamber of the CSC.

The DC cage consists of 33 overlapping electrodes with alternating inner diameters of 250 mm and 267 mm. The electrodes are mounted on PEEK rods, insulated from each other using PEEK spacers, and connected with resistors that form a voltage divider to create a homogeneous voltage gradient toward the exit side of the stopping cell. Due to the overlap of the electrodes, the insulators are shielded from the charges in the stopping volume. The electrodes have a distance of 70 mm to the inner chamber walls. The entrance side of the DC cage is formed by a planar titanium window with a thickness of 25 µm. A voltage of up to 3 kV can be applied to the entrance side of the DC cage at a stopping gas pressure of 100 mbar and a temperature of 100 K, corresponding to an areal density of 5 mg/cm^2. Thus, a DC field of 30 V/cm enables fast extraction of the ions from the CSC. The first DC ring and the beam window are biased separately and are not part of the resistor chain. This allows measurement of the electron current on the beam window, which is produced by the ionization of the buffer gas by the beam particles.

The RF carpet is shown schematically in Fig. 9. It has a diameter of 250 mm and a thickness of 1.3 mm, and is made using printed circuit board technology with Rogers RO4003/4350 material. The 500 ring electrodes have a nominal width of 125 µm, a height of 30 µm, and a spacing of 125 µm, corresponding to an electrode density of 4 electrodes/mm. A cylindrical nozzle with a nominal diameter of 0.6 mm is located in the middle of the carpet. The capacitance formed between the odd and even rings and an external inductance define a parallel LC resonant circuit. An RF amplifier (KL-500, RM Italy) is used to drive this resonant circuit, generating RF voltages (peak-to-peak) of up to 120 V at a frequency of about 6.5 MHz. A matching network is included in the RF carpet to match the impedance of the amplifier. In addition to the RF voltage, a DC voltage gradient can be applied to the RF carpet to drive the ions toward the exit nozzle. The electronic components for the RF and DC voltages are placed on the backside of the carpet except for the coil that forms the inductance for the resonant circuit, which is mounted on the front side to be in direct thermal contact with the cold stopping gas. The DC voltage gradient is created using a resistor chain. The RF voltage is coupled capacitively onto the DC voltage of each electrode. Connections between the front side and the backside of the carpet are made by 0.1 mm diameter vias. Two inner layers between the front electrodes and the backside of the carpet control the field penetration through the ring electrodes and provide a fine control of the DC field in front of the electrodes. No electronics is placed close to the extraction nozzle on the backside to reduce the influence on the ions between the nozzle and the extraction RFQ. An additional layer shields the ion pathway behind the RF carpet. The RF carpet is also equipped with circuits for a direct measurement of the RF amplitude during operation.

A ^{223}Ra recoil ion source with a half-life of 11.4 days or a ^{228}Th recoil source with a half-life of 1.9 years as well as a ^{252}Cf fission source can be mounted to the entrance side of the stopping region. The recoils and their decay products can be used for commissioning, optimization, calibration, and performance characterization of the CSC. In addition, a discharge ion source is mounted on the DC cage about 30 cm away from the RF carpet; it

allows testing the operation of the CSC off-line at high ionization densities and investigating the cleanliness of the stopping gas.

3.2.2 Experiment

The CSC was commissioned in five test experiments in 2011–2016 as part of the FRS Ion Catcher at the FRS at GSI. The performance parameters of the CSC were determined, and first experiments targeting measurements of exotic nuclei were performed [5, 45, 47–57]. The results of the commissioning are reported here. Since then, the stopping cell was employed for a large variety of experiments, both, with off-line ion sources [58–62] and on-line in FAIR-Phase-0 [8, 53, 63–65].

The FRS Ion Catcher setup at the final focus of the FRS consists of the CSC, an RFQ beamline and the multiple-reflection time-of-flight mass spectrometer (MR-TOF-MS) for the MATS experiment. The setup used during the commissioning experiments is shown schematically in Fig. 10 and as photograph in Fig. 11.

Exotic nuclei are produced at relativistic energies by projectile fragmentation or fission on a Be target at the entrance of the projectile fragment separator FRS and separated in-flight. At the Super-FRS, a pre-separator and a main separator will be used for the separation of the ions of interest from unwanted contaminants. The dedicated energy buncher at the Low-Energy-Branch will perform the range compression. In contrast, there is no dedicated energy buncher stage at the FRS. For experiments with the CSC, the FRS is therefore operated in a special mode, such that both separation and range compression are performed using the four dipole stages. The variable degrader system at the central focal plane of the FRS can be tuned to act as an achromatic degrader for optimum separation performance or as a monoenergetic degrader for optimum range bunching [16]. To achieve this, the degrader system consists of two counter-rotating wedge-shaped aluminum disks, two aluminum wedges, and uniform degrader aluminum slabs. A set of scintillator detectors and two time-projection chambers (TPCs) [105] at the middle and final focal planes and two multiple-sampling ionization chambers (MUSICs) [106, 107] at the final focal plane are used to provide ion-by-ion identification by measurement of the time-of-flight, the magnetic

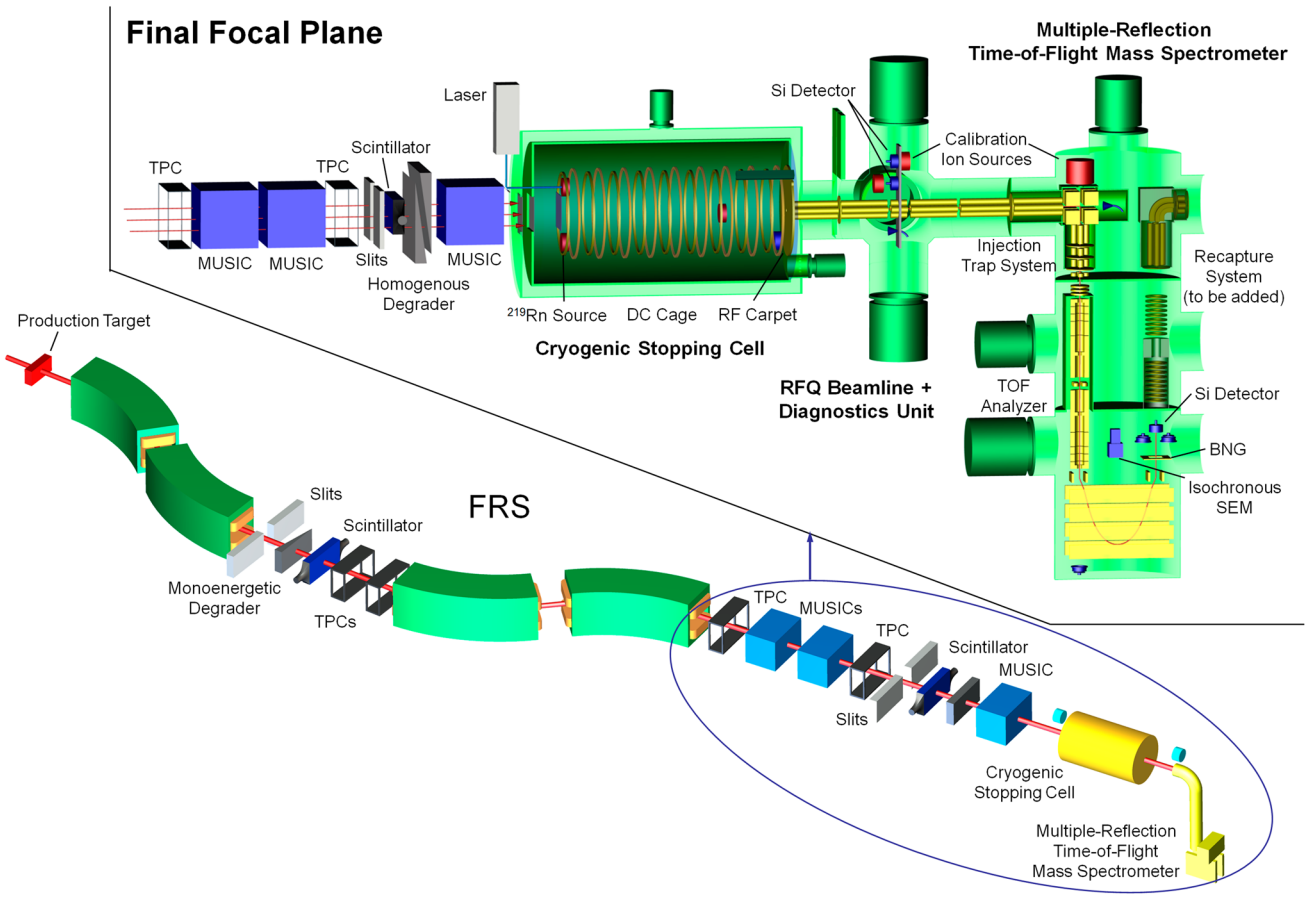

Fig. 10 Schematic figure of the FRS, including its detectors and degraders, and the FRS Ion Catcher setup, as used during the commissioning experiments

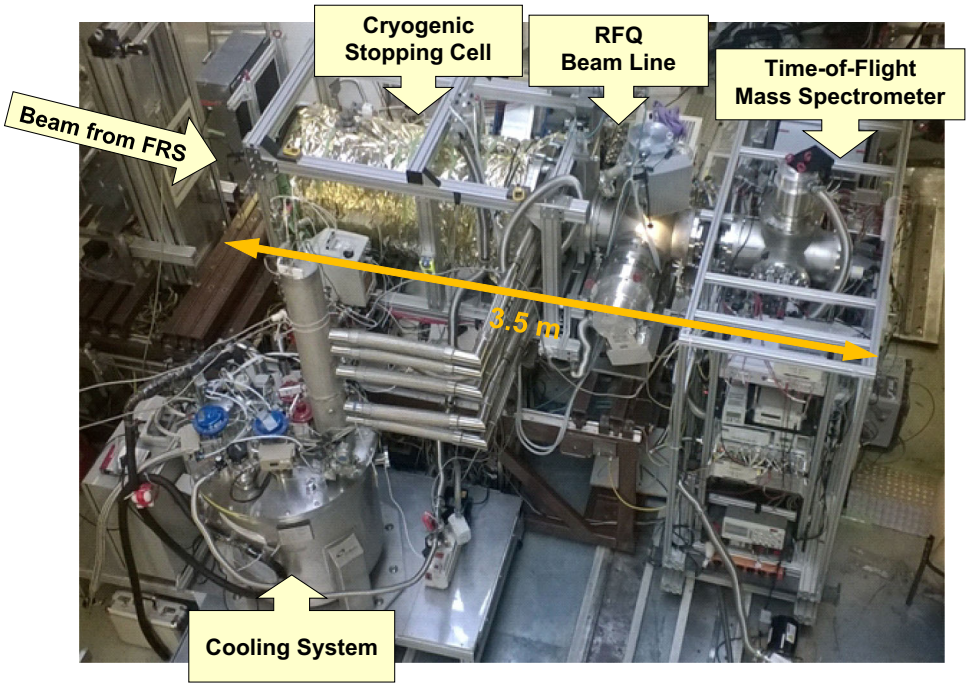

Fig. 11 Photograph of the FRS Ion Catcher setup consisting of the CSC, the RFQ beamline, and the MR-TOF-MS

rigidity, and the energy loss. An additional homogeneous variable degrader at the final focal plane in front of the stopping cell is used to adjust the range of the ions, such that they come to rest in the stopping volume of the CSC. The range of the ions is measured using a third MUSIC mounted behind the homogeneous degrader.

After thermalization of the ions in the CSC, the ions are extracted into a low-energy RFQ transport system. This RFQ beamline is based on a novel concept [42, 47, 73, 98, 108]. This approach allows the beamline to be compact and it provides for differential pumping in the vicinity of the stopping cell, ion cooling, transport, bunching, beam monitoring, and mass separation. Although the full length of the RFQ beamline must be covered with RF structures for ion confinement, solutions have been developed to also implement gate valves, and test ion sources and various detectors for ion identification and counting. In addition, it is possible to split the ion beam, to guide it to different directions, and to merge ion beams into the beamline. This functionality can be implemented in a beamline with a length of about 1 m only. The RFQ beamline is thus ideally suited for the space-restricted area at the final focus of the FRS.

The RFQs rods are built from resistive carbon-filled PEEK with a rod diameter of 11 mm and a radial distance of 10 mm. They are operated with RF voltages with amplitudes of a few hundred volts and frequencies of about 1 MHz. A longitudinal electric field can be created by applying a voltage difference of a few volts between both ends of the RFQ rods [80, 109]. A set of three turbomolecular pumps, with a total pumping speed up to 4000 l/s, are used to pump the extraction region to a pressure of about 1×10^{-2} mbar during operation of the CSC at 100 mbar and 80 K, corresponding to an areal density of 6 mg/cm^2. The diagnostics unit implemented in the RFQ beamline behind the extraction RFQ enables detection, identification, and quantification of the ions extracted from the stopping cell. It consists of three RFQ segments. The middle segment is located in a horizontally movable sled, which includes, in addition to an RFQ segment, two identical setups of negatively biased aluminum foil and silicon surface-barrier detectors, a channeltron detector, and a thermal cesium ion source for testing of instruments downstream of the diagnostics unit. By changing the horizontal position of the detector sled using an in-vacuum step motor and gear system, the respective function of the diagnostics unit can be selected. The channeltron detector setup includes a conversion dynode and can be operated in single-ion detection mode at pressures up to 5×10^{-2} mbar without increase of dark counts or loss in performance [110]. A segmented aperture, mounted between the extraction RFQ and the diagnostics unit, is used as a dipole deflector. It can be used to attenuate the ion beam for the study of ions of strongly different abundance ratios and to determine the time profile of the extracted ions. In addition, it can be used to only transmit ions from the CSC to downstream detectors, when ions of interest are stopped in the CSC. A three-line α source (^{239}Pu, ^{241}Am, ^{244}Cm) is positioned off-axis from the RFQ beamline, such that all silicon detectors can be moved in front of the three-line α source for commissioning or calibration. Vacuum separation between the stopping cell and the beamline for maintenance reasons is realized using a gate valve [110]. The RFQ segment located in the closing region of the valve can be retracted to make way for the valve. This is achieved by a dedicated movable RFQ segment mounted on a second horizontal sled. Within minutes, the CSC can be vacuum-separated from the downstream beamline allowing, e.g., for repairs of

detectors, etc. The extraction RFQ can be operated in broadband transmission mode or in a narrow-band mass filter mode with a mass resolving power (FWHM) of 10 at full transmission efficiency or with a mass resolving power of 100 at a transmission efficiency of a few percent [47, 111]. Thus, ions from the CSC can be mass-selected, and in combination with one of the different detectors, a coarse mass determination or charge-state identification of the ions extracted from the CSC can be performed.

The MR-TOF-MS is connected directly to the RFQ beamline. The MR-TOF-MS is a powerful and universal mass spectrometer. As a broadband mass spectrometer, it can determine the abundances and identities of different ion species extracted from the stopping cell simultaneously. It can be used to optimize the range and the range compression and to verify the cleanliness of the stopping cell and its proper operation. It can be used as a mass tagger for the particle identification (PID) in the FRS or for PID by high-accuracy mass measurement as the only information [10]. The device can be operated as an ultra-high-resolution mass separator to provide an isobarically and isomerically pure beam [49]. In addition, the MR-TOF-MS can perform direct mass measurements of very short-lived and rare nuclides and search for and measure isomeric states.

The MR-TOF-MS is described in detail in [4, 52, 112–115]. Ions enter the device through RFQs and an RFQ switchyard. In a triple-stage injection trap system, the ions are accumulated, cooled by collisions with the buffer gas, and injected as bunches into the time-of-flight analyzer. The analyzer is formed by two electrostatic reflectors. In the analyzer, the ions travel for a selectable number of turns, which determines the mass resolving power. After ejection from the analyzer, the ions pass through the time-focus shift reflector (previously referred to as post-analyzer reflector) [116] and alternatively (i) impinge on an isochronous secondary electron multiplier for measurement of their time-of-flight (mass measurement mode) or (ii) pass through a Bradbury-Nielsen Gate [117], in which unwanted ions are deflected and detected by two gate detectors, and only the ions of interest are transmitted (isobar separator mode). The MR-TOF-MS achieves a mass resolving power of up to 1,000,000, a relative mass measurement accuracy down to 2×10^{-8}, and single-ion sensitivity [63].

In the commissioning experiments with the FRS Ion Catcher, various projectile and fission fragments, covering different sections of the chart of the nuclides, were produced from different primary beams. Heavy α-decaying nuclides in the element region above Pb were produced by projectile fragmentation of a ^{238}U primary beam at an energy of 1000 MeV/u in a Be target with an areal density of $1.624\,\mathrm{g/cm^2}$ followed by a $0.223\,\mathrm{g/cm^2}$ Nb stripper foil. A monoenergetic degrader at the central focal plane of the FRS was used for separation and energy-bunching of the fragments. Intermediate mass, neutron-rich nuclides around the $N = 82$ shell closure were produced by in-flight fission of a ^{238}U primary beam on a $6.333\,\mathrm{g/cm^2}$ Be target and $0.223\,\mathrm{g/cm^2}$ Nb stripper foil. Neutron-deficient nuclides, around mass $A = 160$ and in the mass range $90 < A < 120$, were produced by fragmentation of a ^{238}U primary beam at an energy of 300 MeV/u on a $0.27\,\mathrm{g/cm^2}$ Be target and of a ^{124}Xe primary beam at an energy of 600 MeV/u, respectively, on a $1.622\,\mathrm{g/cm^2}$ Be target. The CSC was operated with helium as stopping gas at pressures ranging from 47 mbar to 106 mbar and temperatures ranging from 78 K to 100 K, corresponding to areal densities ranging from $3.1\,\mathrm{mg/cm^2}$ to $6.3\,\mathrm{mg/cm^2}$. Note that the maximum stopping gas density used in the experiments of $0.06\,\mathrm{mg/cm^3}$ is almost two times larger than that reached previously on-line in a stopping cell with RF structures [80], and the areal density of about $6.3\,\mathrm{mg/cm^2}$ is higher than that reached before with such a stopping cell worldwide. After an upgrade of the pumping system and implementation of an additional pumping stage, a maximum areal density of $9\,\mathrm{mg/cm^2}$ was achieved [101]. Typically, a voltage of 2.5 kV was applied over the DC cage, resulting in a push field with a nominal field strength of about 25 V/cm. The RF carpet was operated with an RF voltage (peak-to-peak) of 50 V to 100 V; a DC voltage of 60 V was typically applied across the RF carpet.

3.2.3 Results

Stopping and extraction efficiencies. Stopping and extraction efficiencies were determined for the heavy α-emitting ^{238}U fragments ^{211}Po, ^{218,219}Rn, ^{220}Ra, ^{221}Ac and ^{223}Th [45, 47, 53]. These measurements were performed at low beam intensities of a few hundred ions per second, such that intensity-related efficiency limitations due to space-charge and plasma effects in the CSC can be ignored. The ions of interest were extracted from the CSC and transported to the silicon detector in the RFQ beamline. Identification was performed by the characteristic α-decay energies of the nuclei. The number of extracted ions of each nuclide of interest was determined from the number of decay events, taking into account the solid angle of the active area of the silicon detector with respect to the collection aluminum foil. The range distribution was measured by scanning the thickness of the homogeneous degrader and determining the number of extracted ions for each thickness. The width of the distribution was then deconvoluted from the areal density of the stopping cell. The standard deviations of the measured distributions range from $13\,\mathrm{mg/cm^2}$ to $21\,\mathrm{mg/cm^2}$ (in thickness of the aluminum degrader) depending on the fragment and the settings of the FRS. Under the conditions of the experiment, the corresponding standard deviations of the range distributions in the helium stopping gas in the CSC can be obtained by dividing by a conversion factor of (2.0 ± 0.1). The stopping efficiency can be calculated from the relative overlap between the known areal density

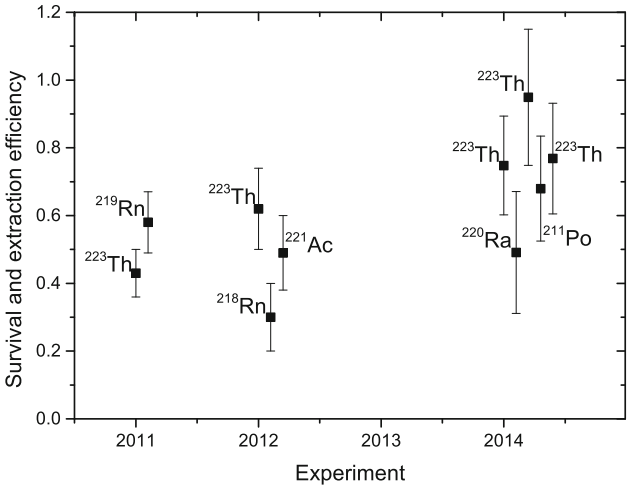

Fig. 12 Ion survival and extraction efficiency for different projectile fragments as measured during the three experiments. The enhanced cleanliness of the CSC results in an increased efficiency

of the CSC and the measured range distribution for each nuclide. Stopping efficiencies in the range from 15% to 27% were obtained.

The total efficiency for the thermalization of the ions includes the stopping efficiency and the extraction efficiency. For the optimum degrader thickness, the total efficiency of the CSC for a selected nuclide was determined as the ratio of the number of extracted ions of this nuclide to the number of ions of this nuclide entering the CSC. The number of ions entering the CSC was determined from the particle identification in the FRS. Corrections were applied, taking into account the dead time of the in-flight data-acquisition system, misidentification of particles where the signals of the different in-flight detectors could not be correlated to a single ion, fragmentation losses in the homogeneous degrader, and decay losses. Total efficiencies in the range from 5% to 22% were obtained depending on nuclide, setting of the FRS, and operating condition of the CSC.

The combined ion survival and extraction efficiency was determined from the ratio of the total efficiency and the stopping efficiency. It reflects ion losses due to neutralization during the slowing-down and thermalization processes in the CSC as well as losses due to collisions of the ions with the electrodes of the CSC during the transport and extraction. The extraction efficiencies for the investigated nuclides are shown in Fig. 12 for the different years of the respective experiment. The mean survival and extraction efficiency for the experiments in 2011 and 2012 amounts to $(47 \pm 8)\%$, for the experiment in 2014 to $(80 \pm 14)\%$. These efficiency values are among the highest obtained for gas-filled stopping cells. The increase in survival and extraction efficiency achieved over the years is most likely a result of the effort put into increasing the cleanliness of the CSC, e.g., the addition of a purification getter in the helium feeding line and a bake-out before cool-down [47]. It is noteworthy that similar extraction efficiencies are obtained for ions of the noble gas element Ra and the chemically very reactive element Th as for ions of the other elements; within the experimental uncertainties, the observed efficiency values do not depend on the chemical properties of the elements. This shows the excellent cleanliness of the prototype CSC.

Rate capability. At high rates of incoming ions, space-charge effects arise in the CSC, which may lead to strong ion losses (Sect. 2.2). The space-charge effect can manifest itself in three regions: (i) along the length of the stopping volume [80], (ii) at the RF carpet [84], and (iii) at the extraction nozzle of RF carpet [85]. It is crucial not only to measure the rate capability but also to identify the region where it is strongest to enable the development of effective strategies to counteract space-charge effects. The rate capability of the CSC and the region of space-charge effects were determined in three experiments, here referred to as Experiments I, II, and III.

In Experiments I and II, the rate capability study was performed by measuring the extraction efficiencies for different beam intensities and for two different DC field strengths applied along the length of the CSC (push field) [50, 51]. In Experiment I, ^{221}Ac ions (half-life of 52 ms) were thermalized in the helium gas at a pressure of 49 mbar and a temperature of 74 K, corresponding to an areal density of 3.3 mg/cm^2. They were extracted from the CSC into the RFQ beamline and were identified and counted by their characteristic α-decay energies in the silicon detector. In Experiment II, ^{213}Fr ions (half-life of 34.6 s) were thermalized in the helium gas at a pressure of 63 mbar and a temperature of 86 K, corresponding to an areal density of 3.7 mg/cm^2. After extraction from the CSC, they were transferred to the MR-TOF-MS and identified by their time-of-flight. The beam intensities were measured using the scintillator mounted in front of the CSC. Ionization of the helium gas in the CSC resulted in an electric current on the window located at the entrance of the DC cage inside the CSC. In Experiment II, this current was measured and allowed the determination of the number of electrons produced per ion injected into the CSC. The measurements were performed using short beam spills (4–6 ms). At the same overall number of ions, short spills give rise to stronger space-charge effects in the CSC than long spills, since the rate (ions/s) is larger.

To complement the measurements, simulations of space-charge effects occurring in the CSC were performed [86]. The longitudinal and transverse distributions of the stopped ions and of the ionization created in the CSC were obtained using the simulation programs MOCADI [71] and SRIM [118]. These distributions were used as starting distributions for trajectory calculations of the ions in the CSC, which take into account the externally applied electric field, the space-charge field created by the ions, and the mobility and diffusion of the ions in the helium stopping gas (see Sect. 5). The ion motion at the RF carpet or in the nozzle was not included in the simulation. Rather, an ion was considered to be successfully extracted from the CSC if it reached the RF carpet. Hence, the simulation study addressed only the space-charge effect along the length of the CSC. The simulations were also used to derive a conversion factor to convert the results of measurements and simulations with pulsed bunches of ions to the equivalent values for a DC beam. Comparison of the measurements and the simulations also requires knowledge about the number of helium ion–electron pairs created per ion impinging on the CSC. The corresponding conversion factor depends on the energy the ion deposits in the CSC and hence on the beam energy, the beam composition, the range of the beam components, and the areal density of the stopping cell. Taking into account that the mean energy loss per helium ion–electron pair amounts to 41 eV [119], 6.4×10^6 helium ion–electron pairs were created per impinging ion in the experiment with ^{221}Ac and 9.5×10^6 helium ion–electron pairs in the experiment with ^{213}Fr. The latter value is compatible with the measurement of the electron current on the entrance window of the DC cage of the CSC.

The extraction efficiencies for ^{221}Ac and ^{213}Fr measured as a function of the beam rate are shown in Fig. 13a. The rate was converted to the equivalent rate for a DC beam and the extraction efficiencies were normalized to an extraction efficiency of unity at low rate. Up to a rate of about 10^4 ions/s injected into the CSC, the extraction efficiency is constant. For higher beam rates, the extraction efficiency decreases strongly with increasing rate and drops to about 10% of its original value at 10^7 ions/s. A higher DC push field strength increases the extraction efficiency at a given beam rate, or conversely, it increases the rate for a given extraction efficiency; however, the

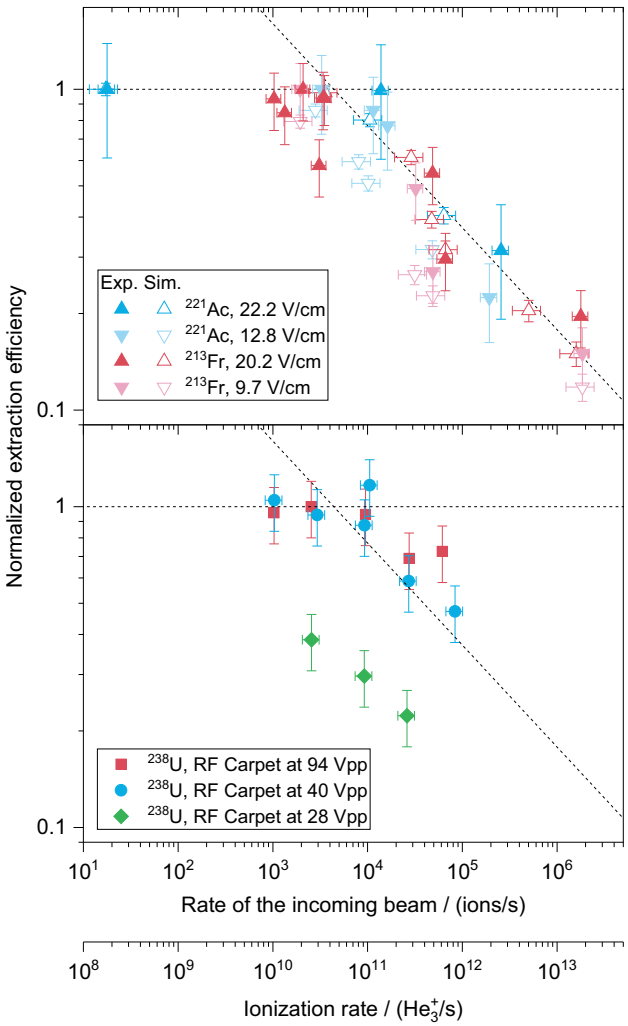

Fig. 13 **a** Top panel: Extraction efficiencies for ^{221}Ac ions (Experiment I) and ^{213}Fr ions (Experiment II) as a function of the beam rate from experiment (solid symbols) and simulation (open symbols) for two different electric DC field strengths. Each data series has been normalized independently to an extraction efficiency of unity at low rate. **b** Bottom panel: Measured extraction efficiencies for ^{238}U ions (Experiment III) as a function of the beam rate for three different RF voltages at the RF carpet. The data series have been normalized to an extraction efficiency of unity for the highest RF voltage at low rate. The dashed lines are drawn to guide the eye

gain in rate for an increase in field strength by a factor of two is only about 40%. The results of the simulations are in good agreement with the measured results. The agreement is a strong indication that the reduction of the efficiency with increasing beam rate is due to space-charge effects along the DC cage of the CSC, rather than due to space-charge effects at the RF carpet or in the nozzle region of the CSC.

To further rule out space-charge effects at the RF carpet as a cause for reduced extraction efficiency at high beam intensities, Experiment III was conducted, which investigated the rate capability at different RF voltages applied to the RF carpet using ^{238}U primary beam [101, 120]. ^{238}U ions were thermalized in the helium gas at a pressure of 59 mbar and a temperature of 94 K, corresponding to an areal density of 3.2 mg/cm^2, extracted from the CSC and identified and counted with the MR-TOF-MS. A spill length of 1 s was used, and the CSC was operated with a DC push field of 20.0 V/cm. As uranium is a highly reactive element it was detected in different molecular forms. The extraction efficiencies were calculated from the total count rates of all observed forms, i.e., $^{238}U^{2+}$, $^{238}UO^{2+}$, $^{238}UOH^{2+}$, and $^{238}UO_2^{2+}$. They are shown in Fig. 13b as a function of the beam rate. The slopes of the decrease in extraction efficiency with beam rates are independent of the RF voltage and are the same as those observed in the Experiments I and II. While the extraction efficiencies for the RF voltages (peak-peak) of 40 V and 94 V are the same, the extraction efficiency at the lowest RF voltage of 28 V is systematically reduced to approximately 40% of the values measured at the higher RF voltages and, remarkably, the reduction factor is the same for all investigated beam intensities. This can be explained by the fact that at an RF voltage of 28 V, the repelling field of the RF carpet is not strong enough to enable a safe transport of the ions over a longer distance along the RF carpet, whereas at an RF voltage of 40 V and higher full ion transport is achieved. The observation that the relative ion loss at the carpet at low RF voltage is independent of beam rate is a clear indication that the ion transport along the RF Carpet is not affected by high beam rates of incoming beam, and that the decrease in extraction efficiency is due to space-charge effects along the length of the stopping volume.

This can be explained by the transmission characteristics of the RF carpet. When the CSC is operated at high rates, high charge densities of helium ions and ionized contaminants arise in the bulk of the CSC. However, the majority of this charge is not transported by the RF carpet. The RF carpet acts as high-mass filter, which transports only ions with mass-to-charge ratios above a certain cut-off value. This low-mass cut-off can be adjusted using the RF amplitude. The motion of ions with mass-to-charge ratios below the low-mass cut-off is unstable, such that they are not repelled by the RF field, but impinge on the conducting sections of the RF carpet (Fig. 14). As will be shown below, the purity of the ions extracted from the CSC is high and a large abundance of contaminant ions is expected only at low mass. Therefore, the majority of the space charge is due to the helium ions and light contaminant ions (e.g., ionized nitrogen molecules). It is hence immediately lost at the carpet and never reaches the nozzle, in contrast to the much heavier projectile fragments, which are transported by the RF carpet and are extracted. This also excludes the nozzle of the RF carpet as a region responsible for the space-charge effect.

The results of the study shows that the rate capability of the CSC is limited by the space-charge effects along the length of its stopping volume. It follows that the key to high rate capability of the Super-FRS CSC lies in short extraction paths and high field strengths. This conclusion has been verified by later work, in which the DC cage was replaced with a new DC cage that has only half the length of the original DC cage and a somewhat larger effective inner diameter [120, 121]. An increase in the rate capability by a factor of at least 20 has been achieved.

The conditions chosen for the reported Experiments I, II, and III are challenging (i) since the high energy of the ions leads to a large energy straggling after slowing-down and consequently requires a high stopping gas density and (ii) because of the high nuclear charge of the fragments. Since the energy deposition roughly scales with the square of the nuclear charge, the rate capability of the CSC for lighter elements will be much higher.

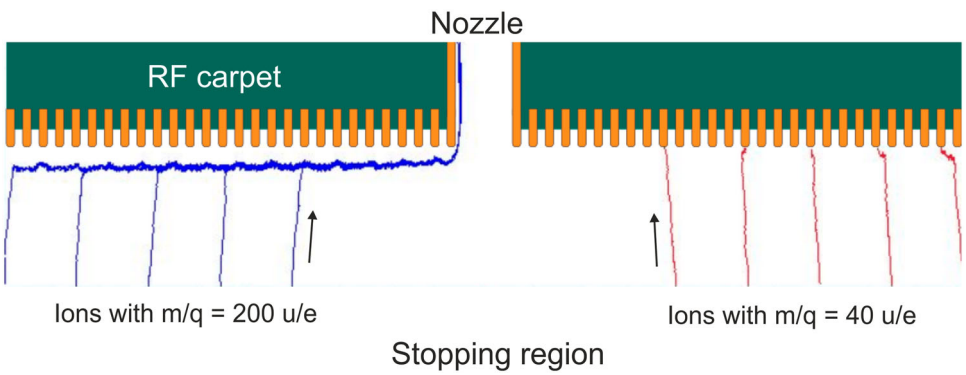

Fig. 14 Simulated ion trajectories of two different ion species with mass-to-charge ratios m/q of 200 u/e and 40 u/e at an RF carpet set to a low-mass cut-off of about 40 u/e. While the ions with $m/q = 200\,u/e$ are transported along the RF carpet, the ions with $m/q = 40\,u/e$ hit the RF carpet electrodes and never reach the extraction nozzle

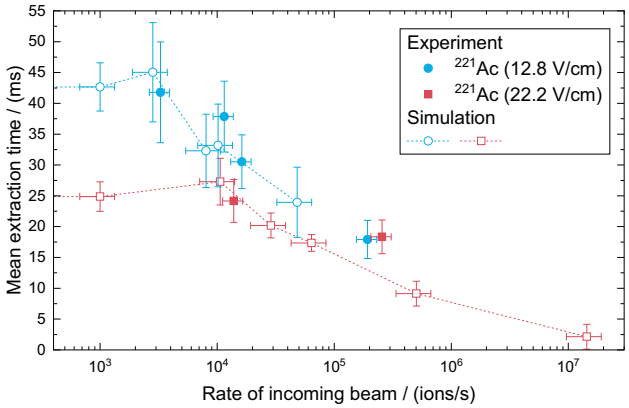

Fig. 15 Mean extraction time of ^{221}Ac ions from the CSC as a function of the beam rate for two different mean electric DC field strengths along the body of the CSC. The pressure and the temperature in the CSC amounted to 49 mbar and 74 K, respectively. The measured values (solid symbols) are compared with the results of simulations (open symbols)

Long-term operation of the CSC at rates of about 10^6 ions/s injected into the CSC did not result in noticeable changes to the RF carpet, e.g., arising from charging of the insulating sections of the carpet. Short-term operation with up to 8×10^8 ions injected into the cell ignited a steady discharge, but did not cause damage to the CSC.

Extraction Times. A measurement of the extraction time as a function of the beam rate was performed using short spills of ^{221}Ac, as in Experiment I described above (Sect. 3.2.3: Rate capability). The pressure and the temperature of the buffer gas in the CSC amounted to 49 mbar and 74 K, respectively [45, 50]. After injection of the ion bunch into the CSC, the decays of the extracted ^{221}Ac ions were measured on the silicon detector located behind the CSC. After injection of the ^{221}Ac ions, activity accumulates on the silicon detector and the decay rate increases. After the last ^{221}Ac ions are extracted, the decay rate decreases again. The mean extraction time is half that of the maximum extraction time. For a beam rate of 650 ions per spill and a DC field strength of 22.2 V/cm, a mean extraction time of 24 ms was determined in good agreement with simulations [86]. Similar extraction times were obtained in off-line measurements [48].

The extraction times determined by measurements and simulations as a function of the beam rate are shown in Fig. 15. Up to a rate of about 10^4 ions/s injected into the CSC the extraction times are roughly constant. For the higher DC field strength, shorter extraction times are achieved. The values obtained by simulations agree with the results predicted by the ion mobilities. For higher beam rates, the extraction time decreases, and the difference between the extraction times at high and low DC field strengths reduces. The measurements and the simulations are in fair agreement, although for the higher DC field strength, only two experimental data points are available. The decrease can be explained by the fact that with increasing space-charge effects only ions close to the nozzle region of the CSC are extracted. Since they have a shorter distance to travel to the nozzle than ions from other regions in the CSC, the extraction time is reduced. A higher DC field strength increases the region, from which ions are extracted. Thus, for a higher DC field strength, the average distance the ions need to travel is larger, but the ion velocity is also larger. These two effects compensate each other to a certain extent, reducing the difference in the extraction times at high and low field strengths under space-charge conditions.

Purity of the extracted ions. The cleanliness of the CSC was investigated using the MR-TOF-MS in a broadband mode [47]. Figure 16 shows a mass spectrum of extracted ions in the mass range from 190 u/e to 240 u/e, while ^{213}Fr and ^{212}Fr were injected into the CSC. In addition to the extracted projectile fragments, the mass spectrum also contains mass lines corresponding to ^{219}Rn ions from the internal ^{223}Ra recoil ion source in the CSC and their decay products. The ratio of the number of ions originating from the beam injected into the CSC to the number of contaminant ions produced in the CSC, e.g., by charge exchange or chemical reactions, amounts to 2.2 for the mass window shown in the spectrum. In this calculation, the mass line corresponding to ^{211}Pb+OH was counted as background. The average contamination background per mass unit amounts to only 1.2 counts. Therefore, a signal-to-noise ratio for ^{213}Fr of 70 to 1 is obtained. Clearly, the CSC features such a good cleanliness that contaminant ions are not a major problem in this mass range.

This behavior also does not change significantly at higher beam rates. Mass spectra of ions extracted from the CSC at different beam rates were acquired with the MR-TOF-MS. They are dominated by the ions of interest, which have been stopped in the CSC. Furthermore, within the uncertainties of the measurement, the ratio of the number of contaminant ions, such as ions with adducts or molecular contaminants, to the number of ions of interest does not depend significantly on the beam rate.

Despite the excellent cleanliness of the CSC, some contaminants were observed in mass spectra at lower mass. These have been found to be mostly light molecules containing noble gases. The noble gas atoms are most likely

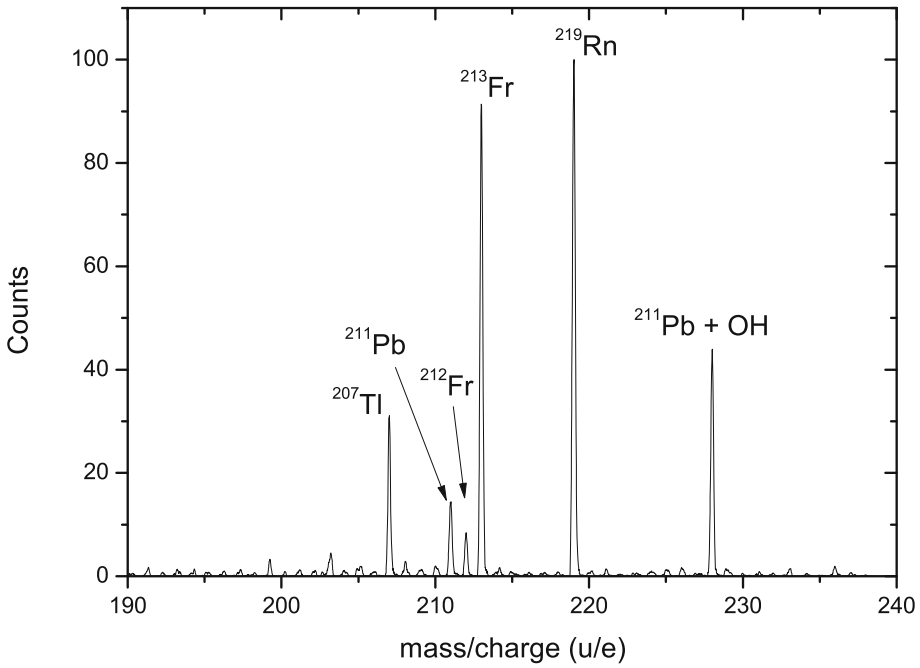

Fig. 16 Mass spectrum of ^{238}U projectile fragments extracted from the CSC. The labeled mass lines originate from the beam and from the ^{223}Ra recoil source in the CSC

introduced into the CSC together with the helium stopping gas. As an example, Fig. 17a shows a high-resolution MR-TOF-MS spectrum of ions extracted from the CSC in an experiment, in which ^{124}Xe primary beam was injected into the CSC and thermalized. Abundant ions containing krypton atoms dominate the mass spectrum, but no further contaminants are observed. Note that the spectrum, despite the high resolution, covers a mass range from 108 u/e to 130 u/e.

The molecular ions do not harm ion survival, but can still hamper measurements of the ions of interest, because they may be much more abundant than the ions of interest. These contaminants can be removed using a collision induced dissociation (CID) process together with two-stage mass separation in the RFQ beamline downstream of the CSC (isolation–dissociation–isolation method, IDI) [54, 122]. In the first stage, the extraction RFQ is operated as a mass filter to transmit only ions in a narrow band of mass-to-charge ratios, including the ions of interest. Then the ions are accelerated by a voltage gradient of 50–80 V in the three RFQs in the diagnostics unit, either by applying this voltage difference along the resistive RFQ rods, or as voltage steps between the RFQs. Depending

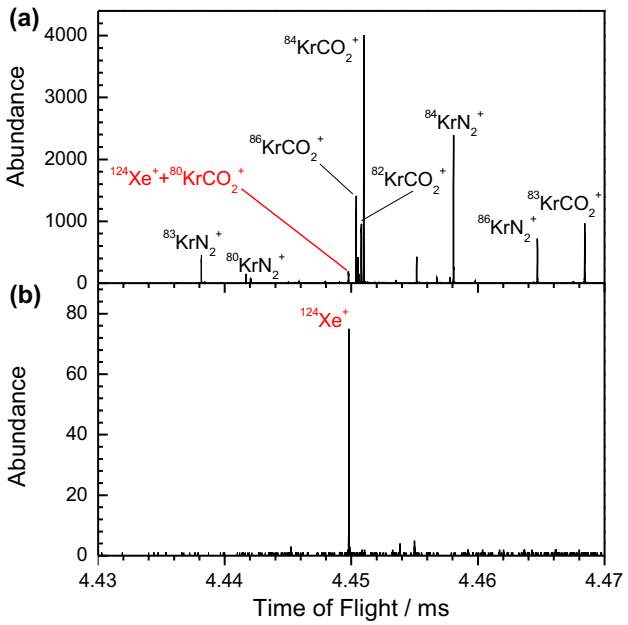

Fig. 17 High-resolution time-of-flight spectrum of ions extracted from the CSC and measured with the MR-TOF-MS when injecting ^{124}Xe primary beam. Ions from different mass numbers appear in the spectrum; they undergo different numbers of turns in the MR-TOF-MS. **a** No CID applied, the spectrum is dominated by contaminants. The ^{124}Xe peak (in red) is covered under the $^{80}KrCO_2^+$ peak. **b** IDI is applied. The measurement time here is four times longer. The contaminants are suppressed by a factor of 10^4

on the amount of kinetic energy of the ions converted to the internal degrees of freedom in collisions with the buffer gas in the RFQs and the chemical structure of the ions, polyatomic ions are fragmented. In the last step, the fragment ions are removed from the RFQ beamline, e.g., by operating the RFQ with a higher RF amplitude, such that lighter ions than the ions of interest are ejected radially. Figure 17b demonstrates this method. Due to the application of IDI, the contaminants are removed from the spectrum with a suppression factor of 10^4, including the isobaric contaminant $^{80}KrCO_2^+$ with a mass difference from ^{124}Xe of $\sim 300\,keV$ only. This enables a precision measurement of ^{124}Xe, which represents the ion of interest in this case. This approach is efficient and universal and is foreseen to be used in the RFQ beamline of the stopping cell of the Super-FRS.

An additional method to remove abundant molecular contaminants is the operation of the RF carpet as an ion mobility separator [123]. According to Eq. (1), the transmission at the RF carpet depends both on the mass-to-charge ratio of the ion and its mobility. The transport of polyatomic ions with smaller ion mobilities than the (mono-atomic) ions of interest can therefore be suppressed in the same way as the transport of ions with a small mass-to-charge ratio. The RF voltage of the RF carpet is tuned, such that the transport of polyatomic ions with a similar mass-to-charge ratio as the ions of interest, but with smaller ion mobilities, is suppressed.

Charge states of the extracted ions. For the ions of all elements produced at the FRS and thermalized in the CSC, the charge states were determined [101]. For some cases, the measurement was done by a mass scan using the combination of the extraction RFQ operated as mass filter and either the silicon detector or the channeltron detector in the diagnostics unit. For other cases, the MR-TOF-MS was employed for the measurement. The charge states of the extracted ions are shown for each element in Fig. 18. In the upper half of the box of each element, the predicted charge states are presented in color code, based on the assumption that charge exchange processes in the CSC are governed by the ionization potential of N_2 molecules, which are present in trace amounts in the helium stopping gas. In the lower half of the box of each element, the experimentally measured charge states are shown. The results indicate that the assumption is correct. Further purification of the buffer gas can result in the survival of ions in higher charge states (Fig. 5). As discussed in Sect. 2.2, higher charge states reduce the effective repelling field of the RF carpet in the stopping cell. They thus limit the mass range of the ions transmitted by the RF carpet and extracted from the CSC. Therefore, the stopping cell of the Super-FRS will have the option to control the charge state of thermalized ions using an admixture of a small concentration of another gas for charge exchange, such as argon, krypton, xenon, oxygen, or nitrogen monoxide, to the helium stopping gas.

However, this gas can be ionized by charge exchange with the helium ions and possibly also undergo chemical reactions. Therefore, one needs to consider if this ionization has an adverse effect on the extraction efficiency. This depends on the conditions of the experiment and on the particular choice of the charge-exchange gas. If the mass-to-charge ratio of the (ionized) charge-exchange gas is smaller than that of the ion of interest, its transport at the RF carpet can be suppressed. Alternatively, it can also be removed because of its smaller ion mobility. The admixture of a charge-exchange gas is foreseen not as a general-purpose solution, but for specific cases. It is most relevant for heavy nuclides, which are thermalized in the charge state 3+. For these nuclides, suppression of contaminant ions at the RF carpet is easiest, because of the large mass difference to the contaminant ions. Furthermore, the reduction in charge state due to the charge-exchange gas will help to keep the ions of interest out of the low mass-to-charge range, where significant amounts of contaminant ions may be present. Please note

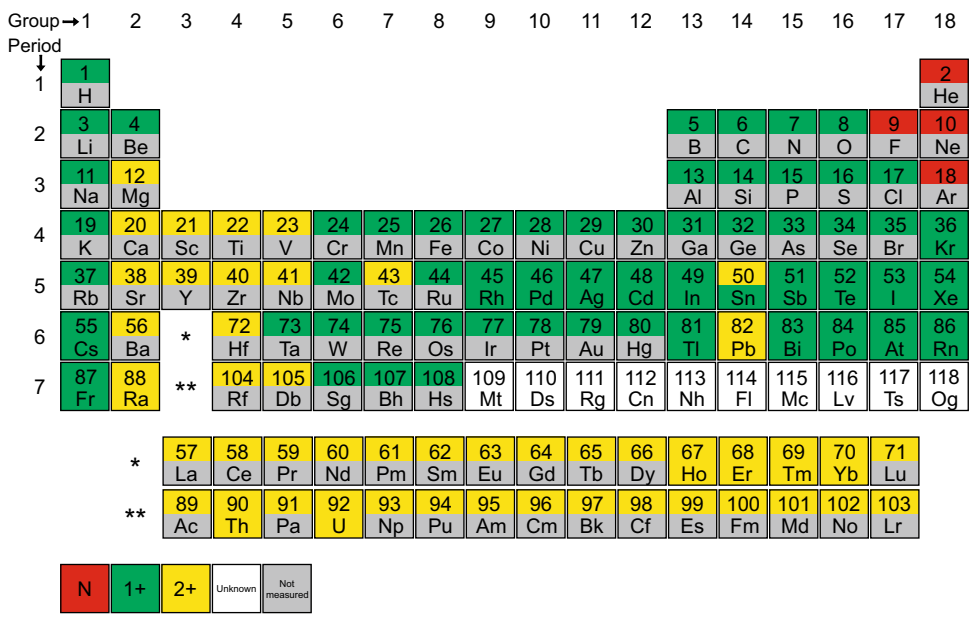

Fig. 18 Predicted and measured charge states of elements extracted from the CSC as given by the color codes at the bottom left of the figure. Upper half of the box for each element: predicted; lower half: measured. The predicted charge state is derived from the first, second, and third ionization potential of each element in comparison with the ionization potential of N_2 (15.6 eV). The ionization data were taken from the NIST database [87]

that the successful operation of the prototype CSC at the FRS Ion Catcher can be seen as that of a CSC filled with pure helium gas and an admixture of nitrogen.

3.3 Operation at high density and high field strength

The stopping cell for the Super-FRS is designed to have a much larger areal density and shorter extraction time than the prototype CSC, which is currently in operation at the FRS. This is in part achieved using higher stopping gas densities, higher DC field strengths, and higher effective fields of the RF carpet. To validate the successful operation of a stopping cell under these conditions, dedicated tests have been performed with the prototype CSC.

3.3.1 Ion transport in the stopping region

The dependence of the extraction time on the stopping gas density has been investigated by measuring the maximum voltage that can be applied along the body of the CSC for different helium gas densities [47]. It was found that the voltage increases approximately linearly with the density. The result agrees with the breakdown voltage described by Paschen's law and lies within the range of predictions given by different models [76, 77]. This indicates that the breakdown most likely occurs either across the voltage break at the feedthrough for the voltage of the DC cage, or between the first electrode of the DC cage, to which the highest voltage is applied, and the inner chamber, which has a distance of 7 cm from the electrode and is held at ground.

From the maximum voltage, the maximum operation DC field along the CSC was calculated and the extraction time of the ions according to ion mobility theory was determined using Eq. (2) for a reduced ion mobility of $17.5\,\mathrm{cm}^2/(\mathrm{Vs})$ and for areal densities up $10\,\mathrm{mg/cm}^2$, corresponding to gas densities of up to $100\,\mu\mathrm{g/cm}^3$, which are required for the stopping cell of the Super-FRS. Figure 19 shows the resulting mean extraction times for different areal densities. The figure also includes extraction times measured off-line using the ^{223}Ra recoil ion source with pulsed operation [48]. These measurements also agree with the on-line measurements shown in Sect. 3.2.3: Extraction times. A mean extraction time of about 25 ms can be achieved almost independently of the areal density of the CSC. This shows that the minimum mean extraction time of a given stopping cell is almost independent of the areal density and that operation of the stopping cell of the Super-FRS at high stopping gas densities will not lead to longer extraction times. The result also shows that the extraction time is defined by the design of the cell. To achieve short extraction times, the path that the ions travel inside the stopping cell needs to be short and high extraction field strengths must be achieved.

3.3.2 Ion transport at the RF carpet

Furthermore, the operation of the RF carpet at high electric DC fields (push fields) directed toward the RF carpet was investigated in off-line experiments with ions from the ^{223}Ra recoil ion source [51]. Since in the prototype CSC, the DC field is limited by discharges from the first electrodes of the DC cage to the inner vacuum chamber or across the voltage break at its feedthrough, higher DC fields can be achieved by shortening the DC cage, i.e., by reducing the distance over which the maximum achievable potential difference is applied. For these tests, the length of the DC cage was reduced from 104.5 cm to 12 cm. Helium gas pressures ranging from 25 mbar to 90 mbar were used at temperatures of about 80 K, corresponding to gas densities of up to $50\,\mu\mathrm{g/cm}^3$. The electrical DC

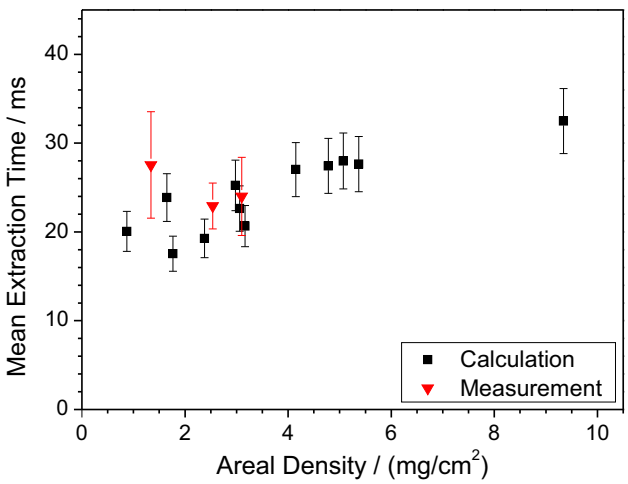

Fig. 19 Measured and calculated extraction times for different areal densities of the CSC. The calculations are based on ion mobility theory and the measured maximum achievable DC field strength along the body of the CSC

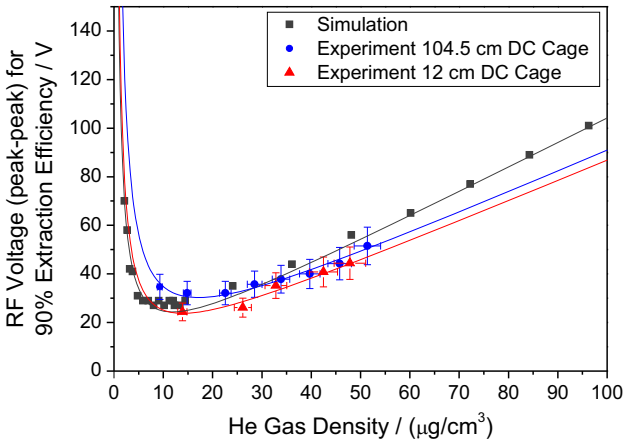

Fig. 20 Measured and simulated minimum RF voltages (peak-peak) required to achieve an extraction efficiency corresponding to 90% of its plateau value as a function of the helium stopping gas density

fields directed toward the RF carpet amounted to values between 13 V/cm and 72 V/cm. The ion source was mounted in front of the RF carpet at a distance of 70 mm.

The RF voltage of the RF carpet required to extract ^{219}Rn ions from the CSC was investigated. In general, a threshold behavior is observed; a certain RF voltage is required to extract ions successfully. With increasing RF voltage, the extraction efficiency quickly increases and reaches a plateau value. Figure 20 shows the measured RF voltages required to achieve an extraction efficiency corresponding to 90% of the plateau value as a function of the helium gas density for a DC field strength of about 10 V/cm. The values are compared with measurements made using the prototype CSC with a long DC cage and with simulations (see also Sect. 5). In general, good agreement is obtained. In a second step, measurements were made for the full range of gas densities and DC field strengths. At a gas density of 48 μg/cm^3 and a DC field strength of 72 V/cm, an RF voltage of less than 70 V (peak-to-peak) was sufficient to reach the plateau value of the extraction efficiency of about 50%. The RF voltages V_{rf} required to achieve an extraction efficiency corresponding to 50% of the plateau value were fitted with the empirical equation

$$V_{\mathrm{rf}} = \frac{C_1}{n} + C_2 \times n, \tag{3}$$

where n is the density of the gas and C_1 and C_2 are constants obtained from the fit. Since the CSC is used only with gas densities larger than 10 μg/cm^3, the first term on the right-hand side of Eq. (3) is small and parameter C_2 is sufficient to describe the RF carpet under typical operating conditions. Figure 21 shows the values for C_2 determined for different DC field strengths and different electric potentials of the inner shielding layer 1 of the

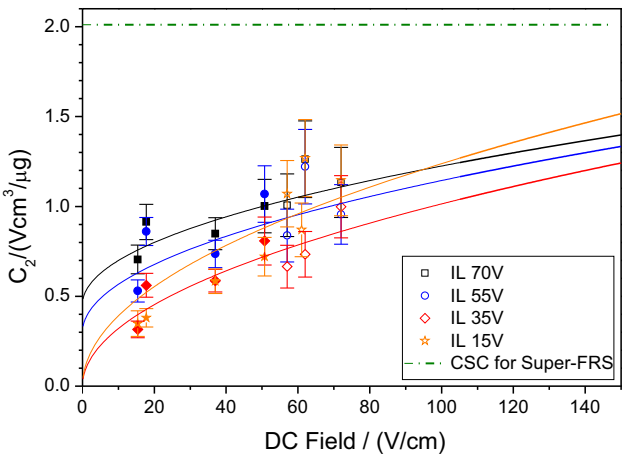

Fig. 21 Measured values of the parameter C_2, which correspond to the minimum RF voltages (peak-to-peak) required to achieve an extraction efficiency corresponding to 50% of its plateau value as a function of the DC field strength and for different electric potentials of the inner shielding layer 1 (IL) of the RF carpet. Full symbols represent data points that have been determined from the fit to a complete measurement series, whereas open symbols correspond to a single measurement only

RF carpet (see also Fig. 9). The measurements are compatible with a square-root dependence of the required RF voltage on the DC field strength as expected from Eq. (1). Figure 21 also shows the value for C_2 that is expected for the stopping cell of the Super-FRS. This value is calculated for a gas density of 137 µg/cm^3, corresponding to a He pressure of 200 mbar at a temperature of 70 K, and an RF voltage of 150 V (peak-to-peak); furthermore, it is scaled according to Eq. (1) by a factor of $(r_0^{\mathrm{Super-FRS}}/r_0^{\mathrm{prototype}})^{(3/2)} = (6/4)^{(3/2)} \approx 1.84$, which reflects that for the stopping cell, an RF carpet with 6 electrodes/mm will be used as compared to 4 electrodes/mm with the prototype CSC. Clearly, the results indicate that the operation of the RF carpet of the stopping cell of the Super-FRS should be compatible with DC field strengths of at least 200 V/cm.

In addition, extraction time measurements were performed for ^{219}Rn ions with the short DC cage. At a gas density of 14 µg/cm^3 and a DC field strength of 19 V/cm, an extraction time of less than 2.5 ms was measured for a distance from the ion source to the RF carpet of 70 mm. This measurement demonstrates that very short extraction times are in reach. Most importantly, it verifies that no significant delays in the ion transport time arise, such as might be possible, in principle, at the innermost rings of the RF carpet before the ions reach the nozzle. The potential of the technique was further demonstrated by the mass and lifetime measurement of the very short-lived nuclide ^{215}Po, which has a half-life of 1.78 ms [51].

4 Conceptual design of the stopping cell

The design of the stopping cell for the Super-FRS is based on the successful concepts and proven technical solutions tested with the prototype CSC (Sect. 3.2) as well as on new concepts developed to fulfill the challenging requirements at the Super-FRS as discussed in Sect. 2. As in the prototype, the stopping cell of the Super-FRS will employ helium as stopping gas at cryogenic temperatures. Helium will be used as stopping gas because of its high ionization potential and chemical inertness. The cryogenic operation is required, because it has been proven to be the method of choice for achieving good ion survival efficiencies and a high purity of the extracted ions. Electric fields will be used to obtain short extraction times from a large stopping volume with a high stopping gas density. RF carpets with a high electrode density will be employed to create strong RF repelling fields at the exit side of the stopping cell, which are required to ensure efficient ion collection and extraction at high stopping gas densities.

However, the design of the prototype CSC is considered to be not sufficient for achieving the design goals for the stopping cell of the Super-FRS. An increase in areal density by a factor of 4, a reduction of the extraction time by a factor of 2, and the increase of the rate capability by at least two orders of magnitude are required. These goals partly contradict each other, such that they cannot be fulfilled by a simple up- or downscaling of the system (see Sect. 2). Rather, a novel concept has been chosen, in which the extraction of the ions occurs in the orthogonal direction to the incoming beam using multiple RF carpets and nozzles, and in which a second, differentially pumped extraction region is employed [11, 70]. A stopping cell of this type is referred to as high-areal-density orthogonal-extraction cryogenic stopping cell (HADO-CSC). As will be shown in Sect. 5.5, a stopping cell with this design can be expected to fulfill the requirements of the Super-FRS. The same conceptual design will also be used for the stopping cells at ELI-NP (Bucharest, Romania) [124] and SARAF (Yavne, Israel) [125]. Further information concerning the stopping cell is also given in [126].

The conceptual design of the stopping cell of the Super-FRS is shown schematically in Fig. 22. As it is the case for the prototype CSC, the CSC for the Super-FRS consists of two main vacuum chambers. An outer chamber provides the thermal insulation for the inner chamber, which is at cryogenic temperature. The inner chamber is divided into a high-density stopping region and a low-density extraction region and is pumped differentially. The ion beam enters the stopping region horizontally through two vacuum windows and is stopped in the helium stopping gas. Using electric DC fields the stopped ions are transported in the orthogonal direction upward to an array of RF carpets, which focuses the ions onto multiple intermediate extraction nozzles; here, the gas flow flushes the ions into the low-density extraction region. In the extraction region, the ions are collected and transported to the exit nozzle using an RF carpet. Behind the exit nozzle, the ions are further separated from the gas in an RFQ beamline and transported to experiments downstream of the CSC.

For the stopping region, a length of 2 m has been chosen. This is considered to be the maximum length for a stopping cell that is practically feasible and can be built and operated with reasonable effort. According to the discussion in Sect. 2, a stopping gas temperature of 70 K has been chosen. At this temperature, most contaminants are frozen out. However, in contrast to even lower gas temperatures, one retains the possibility to use charge-exchange gases, such as argon, krypton, xenon, oxygen, or nitrogen monoxide, to manipulate the charge state of the ions. Furthermore, for much lower gas temperatures, significantly higher cooling power would be required; hence, this choice also ensures reasonable investment and operating costs. The RF carpets in the stopping region will have an electrode density of 6 electrodes/mm. This will allow the stopping cell to be operated with a gas density of at least 137 µg/cm^3, corresponding to a pressure of about 200 mbar (Sect. 5.2). Consequently, the areal

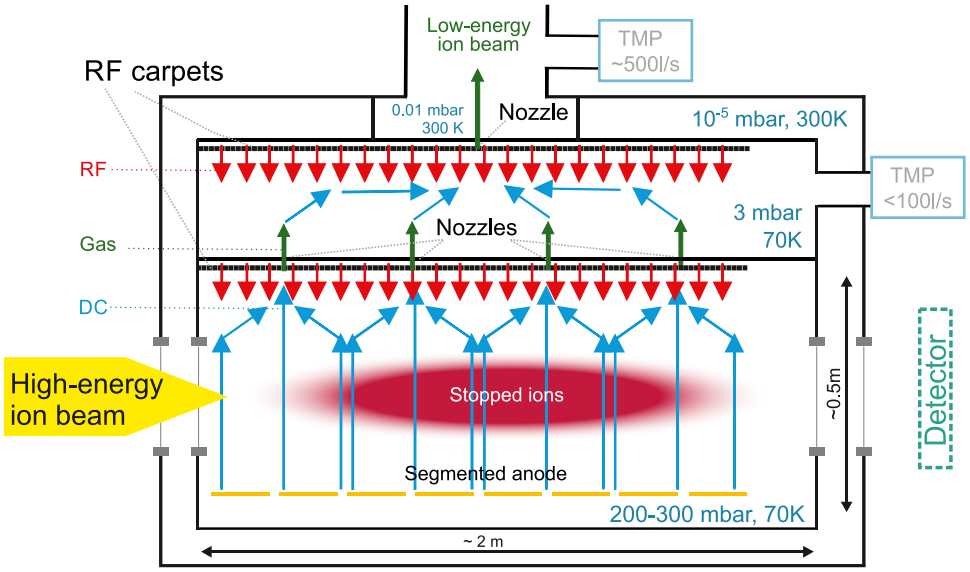

Fig. 22 Schematic figure of the stopping cell for the Super-FRS. For details, see text

density will amount to at least 28 mg/cm^2. The extraction region will also be operated at a temperature of 70 K; the gas density will amount to 2 µg/cm^3, corresponding to a pressure of about 3 mbar. Here, the ion transport will not be driven by static DC fields alone as in the stopping region, but also using a traveling wave technique, which works best at these densities [127].

The CSC for the Super-FRS incorporates several novel concepts:

- **Two-stage extraction.** The inner, cold chamber is divided into a high-density stopping region and a low-density extraction region.
- **Orthogonal extraction.** Ion extraction is performed in the direction orthogonal to the incoming fragment beam (in the non-dispersive plane of the Super-FRS) throughout the full stopping volume. This is in contrast to previous orthogonal-extraction schemes [22, 27].
- **Multiple nozzles.** Multiple extraction nozzles are used in parallel between the high and the low-density region. Ions from these multiple nozzles are merged in the extraction region using an RF carpet.
- **Segmented anode.** The electrode opposite to the RF carpet is segmented to optimize the DC fields throughout the stopping volume, in particular at the RF carpet, and to enable a position-resolved measurement of the ionization current.
- **Particle detector behind the stopping region.** Due to the orthogonal extraction, detectors can be mounted at the end of the stopping region, or the unstopped beam can exit the stopping cell through a window and be detected behind the stopping cell to enable additional diagnostics or experiments.
- **Manipulation of charge states.** The charge state of the ions can be manipulated using trace gases for charge exchange.

Compared to the prototype CSC, these concepts have several important advantages:

- **Performance characteristics independent of the length of the CSC.** The design scales favorably with an increased length of the stopping volume; the length and, consequently, the areal density can be increased without increasing extraction times, decreasing ion extraction efficiencies or rate capability.
- **RF carpet operation at higher gas densities.** The areal density of the CSC is only limited by the effective repelling fields of the RF carpet [Eq. (1)]. The repelling field needs to compensate the DC field that pushes the ions toward the RF carpet at every position along the RF carpet. If the DC push field is generated by a single plate parallel to the RF carpet and an electric DC gradient along the RF carpet is used to focus the ions toward the nozzle, the resulting DC field directed toward the RF carpet near the nozzle is much higher than in the bulk of the stopping region. Thus, a higher repelling field is needed to counteract the DC field and to prevent the ions from hitting the RF carpet. Consequently, a lower stopping gas density must be used for optimum ion transport, because the RF amplitude is limited by discharges. This problem can be solved by segmenting the anode and applying the same DC gradient on the anode as on the RF carpet.
- **Short and ion-independent extraction times.** Due to the orthogonal extraction and the use of multiple nozzles, the extraction path is shortened considerably and all ions have a similar extraction path, independent of their mean stopping position. A higher DC field strength is achieved for a given voltage applied between the

anode and the RF carpet, due to the shorter distance between the anode and the RF carpet. A fast transport of the ions in the extraction region can be achieved using the traveling wave technique.

- **High rate capability.** The short extraction times, due to the high DC field strength, lead to a faster removal of the helium ions and thus increase the rate capability, i.e., the rate at which space-charge or plasma effects arise. A method that has been proposed to counteract the defocusing of the stopped ions due to space charge is to cover the entire inner surface of the stopping volume with RF structures (RF body) [84]. In the CSC, only the extraction side and thus only about one-third of the surface of the stopping volume needs to be covered with RF structures. This simplifies the system significantly and minimizes the needed RF power, which is crucial for cryogenic operation.
- **Improved differential pumping.** The two-stage extraction enables very efficient differential pumping of the CSC. Due to this solution, the operation at high stopping gas densities in combination with multiple nozzles becomes technically feasible. Due to the lower density in the extraction region, an RF carpet with a larger structure size and a lower frequency can be used in this region. Also, the heat input in the extraction region by the RF power is negligible.
- **Stopping position measurement inside the CSC.** The segmented anode opposite to the RF carpet wall collects the electrons created during the stopping; the electron current can be used to measure the stopping position of each ion individually. This allows, for example, a very fast and efficient optimization of the range and range compression. If the segmentation and the sensitivity are high enough, position-resolved measurements of the ionization created by decay products, similar to a time-projection chamber [128], are possible. To increase the sensitivity, a GEM type structure can be used under the conditions of the stopping volume [129, 130].
- **Transparent stopping cell.** The stopping region is not blocked by an RF carpet at its end. Therefore, a detector can be mounted at the end of the stopping volume to identify and count the ions with a longer range. The position and the angle of each ion can be measured with a position-sensitive detector. This allows for easy optimization of the beam position, the focusing and the efficient stopping inside the CSC. Alternatively, windows can be implemented at the end of the CSC, through which ions with a longer range leave the CSC. These ions can be identified with a detector positioned behind the CSC. They can even be used for a different experiment. Moreover, the ion beam does not hit the RF carpet and desorption of atoms and molecules from the RF carpet is avoided. The desorption from the electrodes forming the beginning and end of the stopping region can be avoided by building them from thin wires.

The CSC will employ a helium recovery unit (HRU) to reuse the helium pumped from the stopping region. Such a concept has already been implemented for the PALIS stopping cell at RIKEN [131]. The helium gas can be recovered with a high efficiency and circulates in the CSC for many cycles. Since it is purified at every cycle using getters, the purity of the stopping gas increases far beyond the level achievable without the HRU. In this way, an excellent cleanliness of the CSC can be achieved, although it is not operated at a temperature much below 70 K. Furthermore, the operation costs can be reduced significantly, because the consumption of high-purity helium (He 6.0) is reduced dramatically.

The beam transport behind the extraction region will be performed in a similar RFQ beamline as for the prototype CSC at the FRS Ion Catcher (Sect. 3.2). It will enable very efficient ion transport, versatile diagnostics options, mass-to-charge separation and analysis by mass number, fragmentation of molecular ions, and the preparation of ion bunches. The electric potential of the ion bunches will be shifted using a pulsed drift tube, which is located behind the RFQ beamline. The ion bunches are then injected into the electrostatic beamline for transport to the experimental setups of MATS and LaSpec according to the discussion in Sect. 2.3.

5 Simulation results

Simulation studies were performed to investigate several aspects of the ion transport in the CSC of the Super-FRS, for which a validation was considered to be necessary, but which could not be inferred from tests with the prototype CSC. Two different simulation programs were used in these studies. The simulations package SIMION 8.1 [132, 133] allows to calculate the electric potential distribution for a given set of boundary conditions using the Laplace or the Poisson equation and can perform ion trajectory simulations in these potential distributions. The ion trajectory simulation program ITSIM 6 [134–136] can import potential distributions obtained using different Laplace solvers, including SIMION, and gas flow data, and then calculate ion trajectories, taking into account the electric fields and the interaction with the buffer gas. For the latter, a macroscopic model based on ion mobility and diffusion or a microscopic model that takes into account individual collisions between ions and the buffer gas [137] can be used.

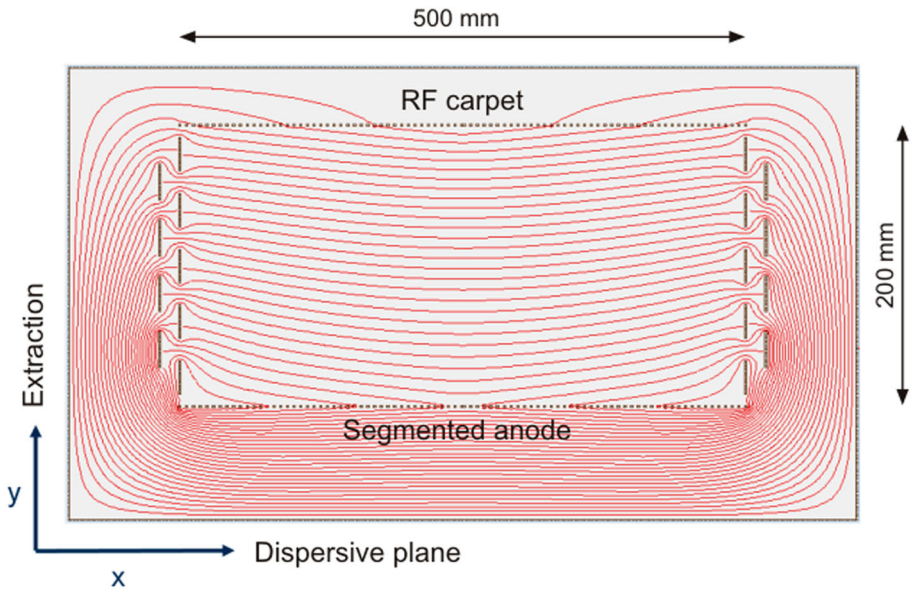

Fig. 23 Cut through the electrode system of the DC cage (black) for the stopping region in the dispersive plane and calculated electric equipotential lines (red). The ions are focused from every position within the stopping region toward the RF carpet and the DC field is almost constant throughout the stopping region

5.1 Electrode system

The electrode structure of the DC cages for the stopping and extraction regions was designed using the simulation program SIMION 8.1 [11, 86]. Figure 23 shows a cut through the electrode system for the stopping region in the dispersive plane and the corresponding calculated electric potential distribution. In this study, a width of 500 mm and a height of 200 mm of the stopping region have been considered. (Note that the values chosen for the final design presented in Sect. 6 are somewhat different.) A voltage is applied between the anode (bottom) and the RF carpet (top), which creates the DC field to drag the ions to the RF carpet. In addition, a voltage gradient is applied along the RF carpet from the outer edges to the center, which drags the ions toward the nozzle. The same voltage gradient is applied to the segmented anode. As can be seen from the equipotential lines, the ions experience a focusing field toward the center at every point in the stopping region, and the DC field directed toward the RF carpet is almost constant throughout the stopping region. Without segmentation of the anode, the DC field directed toward the RF carpet in the vicinity of the nozzle would be much larger (see discussion in Sect. 4). Therefore, the segmentation allows increasing the maximum stopping gas density. Note that the vertical sides of the electrode structure are formed from overlapping electrodes in a similar way as in the DC cage of the prototype CSC. In this way, the stopping region can be pumped efficiently, but the material used to insulate the individual electrodes from each other and to mount them is shielded from the charge created in the stopping volume.

5.2 RF carpet operation

For the design of the RF carpets and the choice of the stopping-gas density, simulations of the ion motion at the RF carpets were performed. SIMION 8.1 was used to calculate the electrode potentials created by the RF carpet and the DC cage. Then, the potential arrays were imported in ITSIM 6 and the ion motion onto and along the RF carpet was simulated and the transport efficiency and the mean transport times were determined, taking into account the ion interaction with the buffer gas.

In a first step, the validity of the simulations was tested. Simulations were performed for the conditions of the experiments presented in Sect. 3.3.2. The experimental and the simulated minimum RF voltages required to achieve an extraction efficiency corresponding to 50% of its plateau value for different stopping-gas densities and electric DC push fields were compared with each other (Fig. 24). The experimental values were derived from the fits to measured values (Fig. 21). The simulated and the experimental values show good agreement. Simulations with the microscopic and the macroscopic collision models reproduce the experimental results within the uncertainties of the measurement. Consequently, it can be assumed that the simulations will also yield reliable predictions for the RF carpets of the CSC for the Super-FRS.

Next, RF carpets with different electrode densities were investigated, and simulations were performed for ions of different mass-to-charge ratios, for different RF amplitudes and frequencies, and for different stopping gas densities. Helium was used as stopping gas at a temperature of 70 K. At cryogenic temperature, the mobilities of heavier singly or doubly charged atomic cations in helium gas are very similar; a reduced ion mobility of $17.5\,\mathrm{cm}^2/(\mathrm{Vs})$ was assumed [78]. The results show that RF carpets with an electrode density of 6 electrodes/mm will be able to fulfill

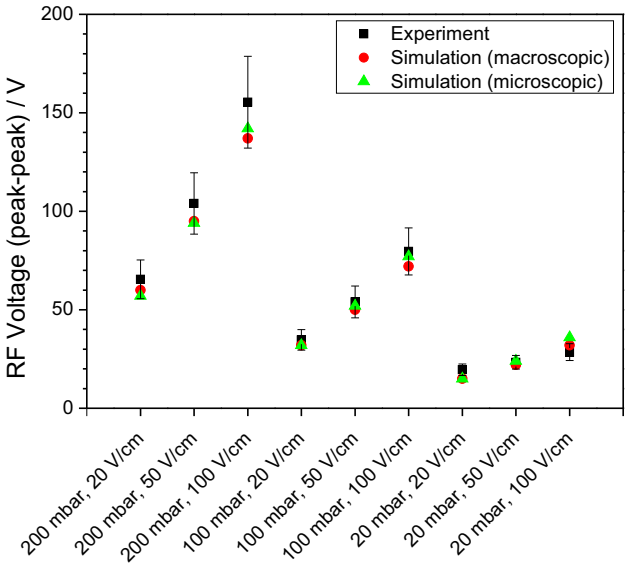

Fig. 24 Comparison of simulated and experimental RF voltages (peak-to-peak) required to achieve an extraction efficiency corresponding to 50% of its plateau value for different helium stopping gas density and DC push fields

the requirements for the stopping region. This finding is in agreement with the extrapolation of the experimental results in Sect. 3.3.2. RF carpets with an electrode density of 6.25 electrodes/mm have already been manufactured and used successfully [138]. RF carpets with a finer structure were rejected because of the challenges they would impose on the manufacturing of the carpets and because of the much larger RF power that would be needed to drive them.

For RF carpets with an electrode density of 6 electrodes/mm, parameter studies were performed to optimize the frequency of the RF voltage applied to the carpets. Three different stopping gas densities were considered. The DC push field used in the simulations was scaled with the gas density to maintain a constant transport time. At a gas density of 137 $\mu g/cm^3$, corresponding to a pressure of 200 mbar, a push field of 100 V/cm was applied; this corresponds to an ion drift time of about 8 ms over a distance of 20 cm. Figure 25 shows the color-coded transmission efficiency as a function of the mass-to-charge ratio and the RF frequency. For all three cases, a certain RF frequency is required to transport the ions; for lighter ions a higher RF frequency is required. As expected from Eq. (1), a limit for the smallest mass-to-charge ratio, which can be transported, exists. With increasing density, this limit increases. From the results, an optimum RF frequency of 15 MHz has been chosen for the operation of the RF carpets in the stopping region. Case (a) with a density of 69 $\mu g/cm^3$, corresponding to a pressure of 100 mbar and an areal density of about 14 mg/cm^2, represents a low-mass mode, which allows to extract very light ions. At the temperatures used in the CSC, helium ions occur primarily as trimers He_3^+; therefore, in this mode, care needs to be taken that ionized helium gas is not extracted together with the ions of interest. Case (b) with a gas density of 137 $\mu g/cm^3$, corresponding to a pressure of 200 mbar and an areal density of about 28 mg/cm^2, represents a standard operation mode of the RF carpet, which optimizes mass range and stopping efficiency. For heavy fragments, even higher gas densities may be used up to about 200 $\mu g/cm^3$, corresponding to an areal density of 41 mg/cm^2, as shown in case (c). Note that these results are in agreement with the extrapolations made based on the experimental measurements obtained with the prototype CSC (Sect. 3.3.2).

Figure 26 shows the color-coded transmission efficiency as a function of the mass-to-charge ratio and the DC push field. The results show that, as expected from Eq. (1), higher push fields can be applied, and thus, shorter transport times and a higher rate capability can be achieved, at the expense of transmitting only larger mass-to-charge ratios, or, conversely, smaller mass-to-charge ratios can be transmitted at the expense of lower push fields and thus longer extraction times. For experiments that are not covered by the standard operation mode of the CSC with about 28 mg/cm^2, either because shorter extraction times or higher rate capabilities are required, or because the experiment involves smaller mass-to-charge ratios, the operating conditions of the CSC can be adjusted and an optimum compromise between areal density, extraction time, rate capability, and mass range can be chosen.

Another important finding of the simulation study is that under reasonable conditions, the transport velocity of the ions along the RF carpet occurs with a velocity that is very similar to that in the bulk of the stopping region. This is the case if no excessive minima of the combined electric DC and effective RF potential are formed at the RF carpet, in which the ions can be trapped. This can be ensured by implementing a shielding layer in the RF carpet (see Sect. 3.2).

The conditions for the RF carpet in the extraction region were investigated using a similar procedure as described above for the RF carpet in the stopping region. In the extraction region, a gas density of 2 $\mu g/cm^3$ will be used,

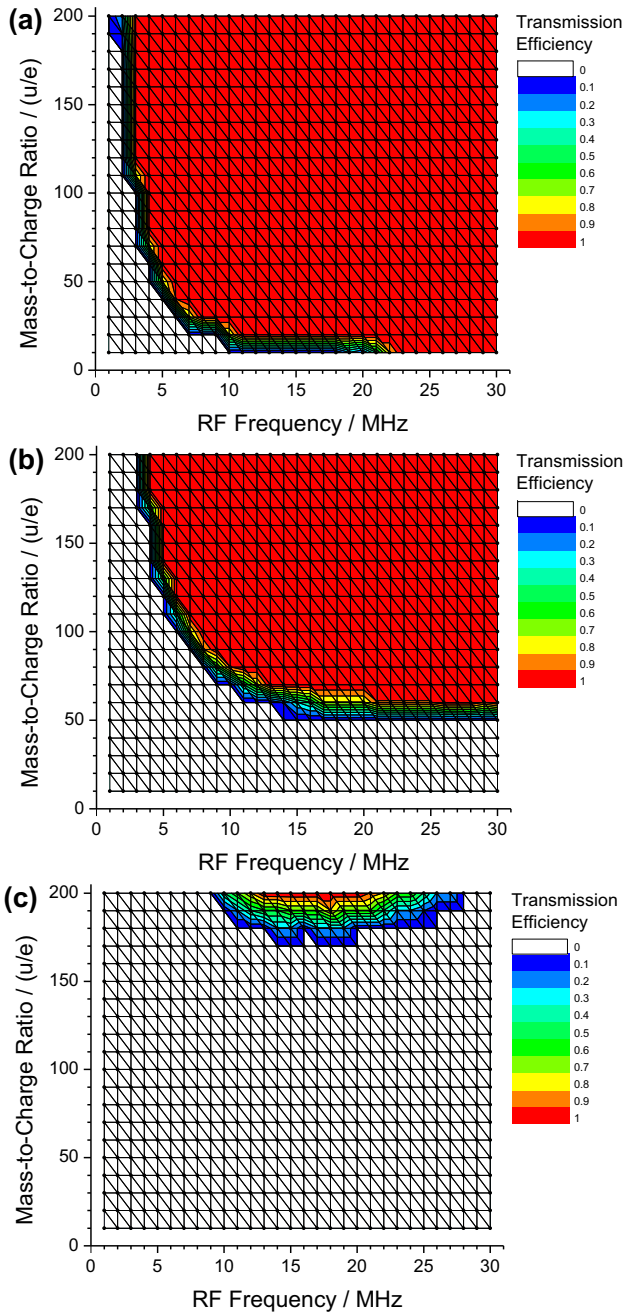

Fig. 25 Simulated transmission efficiency of an RF carpet with an electrode density of 6 electrodes/mm and an RF voltage (peak-to-peak) of 150 V for helium pressures and push fields of **a** 100 mbar and 50 V/cm, **b** 200 mbar and 100 V/cm, and **c** 300 mbar and 150 V/cm, respectively, at a temperature of 70 K as a function of the mass-to-charge ratio of the ion and the RF frequency. The transmission efficiency is given color-coded with red, corresponding to full transmission, and white, corresponding to complete ion loss

corresponding to a pressure of about 3 mbar. Here, an RF carpet with an electrode density of 2 electrodes/mm and an RF frequency of 3 MHz has been found to be suitable.

5.3 Ion transport from stopping region to extraction region

In the stopping region, the ions are transported along the RF carpet, focused onto one of the intermediate extraction nozzles, and captured into the gas flow from the stopping region to the extraction region. In the extraction region, the gas jet transports the ions onto the RF carpet. An additional DC field is applied in the extraction region, which is directed toward the RF carpet. Simulations have been performed to investigate the transition from the ion transport in the gas jet to the transport along the RF carpet, to ensure that the ion motion in the extraction region can be controlled sufficiently and ion losses at the RF carpet can be avoided.

The gas flow from the stopping region to the extraction region was calculated using the simulation program ANSYS-Fluent. Nozzles formed by cylindrical holes in the RF carpet of the stopping region with diameters of

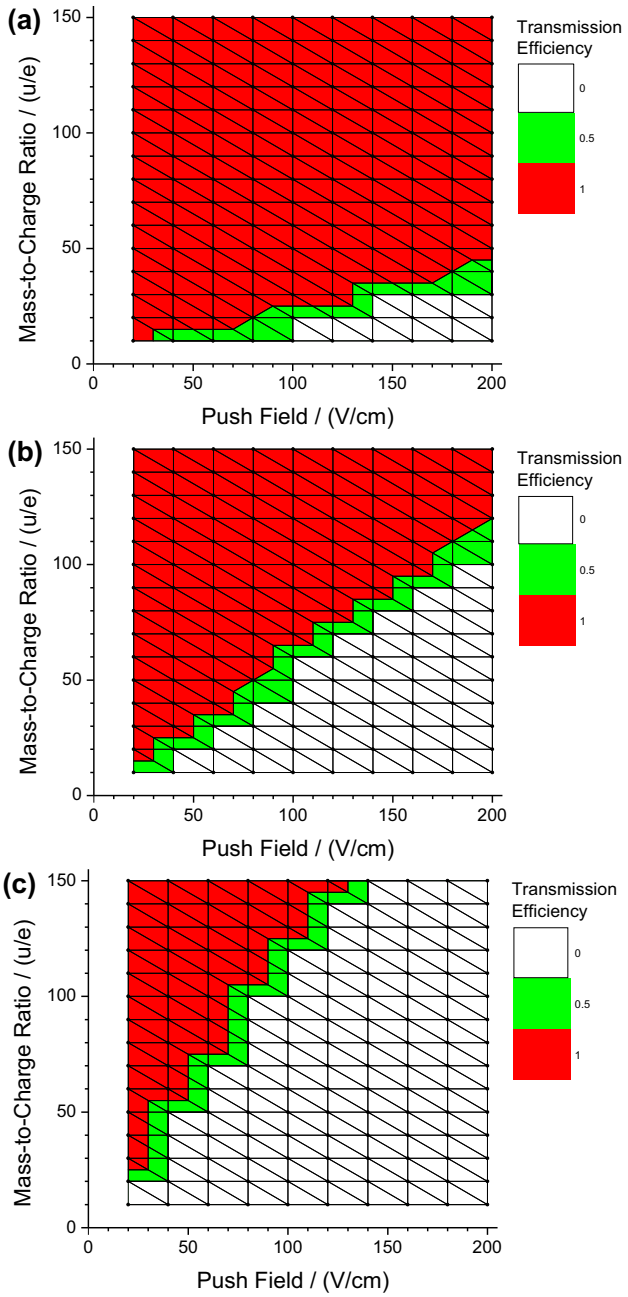

Fig. 26 Simulated transmission efficiency of an RF carpet with an electrode density of 6 electrodes/mm and an RF voltage (peak-to-peak) of 150 V and frequency of 15 MHz for helium pressures of **a** 100 mbar, **b** 200 mbar, and **c** 300 mbar at a temperature of 70 K as a function of the mass-to-charge ratio of the ion and the push field. The transmission efficiency is given color-coded with red, corresponding to full transmission, and white, corresponding to complete ion loss

0.3 mm, 0.4 mm, and 0.6 mm and a length of 1.6 mm were considered; helium gas densities of 128 $\mu g/cm^3$ and 2 $\mu g/cm^3$ at a temperature of 75 K, corresponding to about 200 mbar and 3 mbar, were used in the stopping region and the extraction region, respectively. The distance from the nozzle to the RF carpet in the extraction region amounts to 100 mm.

For simulations of the ion motion, the electric potentials of an RF carpet in the extraction region with two electrodes/mm were calculated using SIMION 8.1 and imported in ITSIM 6.0 together with gas flow data. Ion trajectories were then calculated in the extraction region for singly charged ions of mass 219 u at an RF voltage (peak-to-peak) of 50 V and a push field of 5 V/cm.

Figure 27 shows typical results of simulations for a nozzle with a diameter of 0.6 mm. Without an electric DC field along the RF carpet, the ions approach the carpet and are prevented from hitting the RF carpet by the effective RF repelling field ((a) and (b)). The gas flow then drags the ions away radially along the carpet. If a DC field is applied along the RF carpet, the ions can be guided into a desired direction ((c) and (d)). Further simulations (not shown) demonstrate that ions can also be transported from one side of the gas jet that hits the RF carpet to the other side. Here, the gas flow defocuses the ions in the region of the gas jet, such that they need

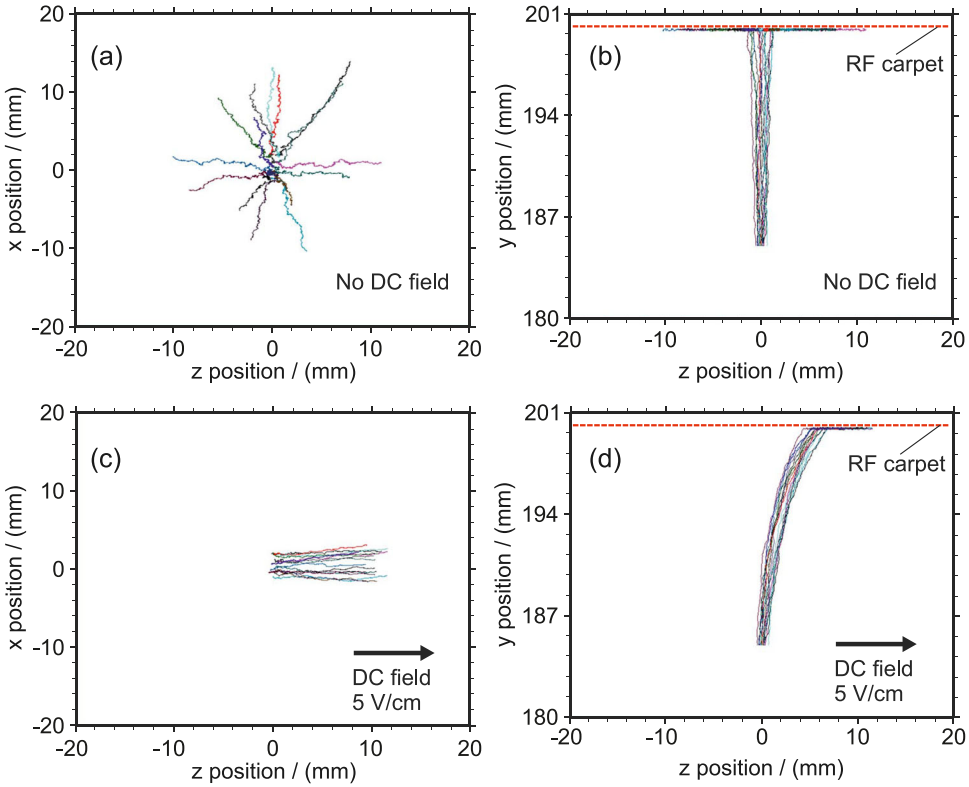

Fig. 27 Simulated trajectories of singly charged ions of mass 219 u approaching the RF carpet in the extraction region in the x-z plane parallel to the RF carpet [panels **a** and **c**] and in the y-z plane orthogonal to the RF carpet [panels (b) and (d)]. For the definition of the coordinate system, please also see Fig. 29. In panels (**a**) and (**b**), no DC field is applied along the RF carpet. In panels (**c**) and (**d**), a DC field of 5 V/cm is applied along the RF carpet. The simulations take into account the gas flow from the stopping region to the extraction region. The pressure in the stopping region amounts to 200 mbar at a temperature of 75 K and the pressure in the extraction region amounts to 3 mbar at a temperature of 75 K. The nozzle is a cylindrical hole with a diameter of 0.6 mm. The RF carpet has 2 electrodes/mm and is operated with an RF voltage (peak-to-peak) of 50 V at a frequency of 3 MHz. The DC push field onto the RF carpet amounts to 5 V/cm

to be re-focused afterward. Qualitatively, the same findings are obtained with simulations considering stronger and weaker gas jets. This indicates that the transport to and along the carpet is rather robust under the conditions envisaged for the CSC and that the ion motion can be sufficiently controlled using the electric fields of the RF carpet.

The simulations further predict that similar transmission efficiencies can be achieved with cylindrical nozzles with diameters of 0.3 mm or 0.4 mm as with nozzles with a diameter of 0.6 mm. Therefore, RF carpets with a nozzle diameter smaller than 0.6 mm will be pursued as an alternative to the 0.6 mm diameter used in the prototype CSC. For these nozzles, a shorter length may be required, i.e., a reduced carpet thickness in the vicinity of the nozzle. In case that nozzles with a reduced diameter are used, the size of the RF carpets along the stopping region can be reduced and the number of RF carpets and nozzles increased correspondingly. This keeps the gas flow rate from the stopping region to the extraction region the same, but reduces the average path length of the ions in the stopping volume and hence reduces the extraction time and increases the rate capability.

5.4 Rate capability

The rate capability of the CSC for the Super-FRS was investigated using the simulation package SIMION 8.1 [11, 51, 86]. These simulations were performed using the same procedure as the simulations of the rate capability of the prototype CSC (Sect. 3.2.3: Rate capability). The external electric fields were calculated from the voltages applied to the DC electrodes of the CSC and the known geometry of the electrodes. The space-charge fields were obtained using the Poisson solver of SIMION, which implements a particle-in-cell method. While the external electric potential is calculated only once, the space-charge potential needs to be re-calculated at every time step of the simulation. The influence of the helium stopping gas was taken into account using the ion mobility, and the effect of diffusion was modeled by applying an offset in the position in each Cartesian direction of each ion per

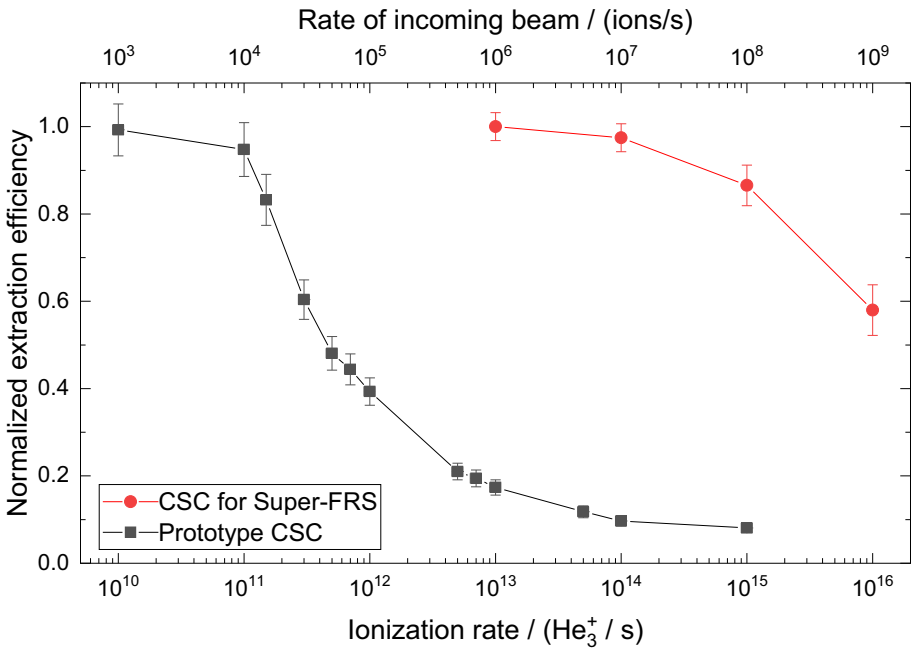

Fig. 28 Simulation of the extraction efficiency of the CSC of the Super-FRS under space-charge conditions in comparison to the prototype CSC (Fig. 13). For the CSC of the Super-FRS, the simulations have been performed for singly charged ions of mass 223 u, a pressure of 300 mbar, a temperature of 100 K, and a DC field of 300 V/cm. The ionization rate is given in helium trimer ions (He_3^+) per second, which are generated due to the ionization of the stopping gas by the stopping of the relativistic ions. He_3^+ is the main charge carrier under the conditions of the CSC

simulation time step. The diffusion coefficient was obtained from the ion mobility using the Einstein relation. A reduced ion mobility of 17.5 $cm^2/(Vs)$ was assumed. Under the conditions of the experiment, the helium ions occur primarily as trimers He_3^+; their reduced mobility amounts to about 18 $cm^2/(Vs)$ [139, 140]. To have a reasonable computation time, only 10^4 ions were simulated and a charge weighting factor, which increases the charge repulsion in the simulation, was applied. The ion motion at the RF carpet or in the nozzle was not included in the simulation. Rather, an ion was considered to be successfully extracted from the CSC when it reached the RF carpet.

The extraction efficiency of the CSC was calculated for different ionization rates and compared with the results obtained for the prototype CSC. The results are shown in Fig. 28. An improvement by three-to-four orders of magnitude is observed. For the prototype CSC, the onset of space-charge effects for heavy elements occurs at about 10^4 ions/s. Taking into account the increased rate capability of the CSC for the Super-FRS, the system should not suffer from space-charge or plasma effects even at the maximum rates allowed at the LEB of 10^7 ions/s.

The increased rate capability compared to the prototype CSC can be explained by the fact that a larger part of the CSC is covered with RF carpets, that the DC fields are stronger, and that the system has a shorter extraction path in the stopping region. For a given extraction voltage, the critical ionization rate, at which space-charge saturation occurs, scales with $1/d^4$, where d is the distance of the extraction electrodes (here: anode and RF carpet) in the stopping region [79]. Compared to the prototype CSC, in the CSC for the Super-FRS d is smaller by a factor of 3.3–5, resulting in an increase in the rate capability by two-to-three orders of magnitude. A further increase in the rate capability is due to the increased density in the stopping region that allows application of higher voltages, and the increased length of the stopping region with multiple extraction nozzles.

As shown above (Sect. 3.2.3: Rate capability), the measured results for the rate capability of the prototype CSC are in good agreement with the corresponding simulations. This indicates that the predictions for the rate capability of the CSC for the Super-FRS should also be reliable. As for the prototype CSC, the majority of the charge, i.e., helium ions and light contaminant ions, will not be transmitted by the RF carpet, but impinge on the RF carpet electrodes. For cases, in which an intense contaminant ion species heavier than the ion of interest might pose a problem, the operation of the RF carpet as an ion mobility separator is foreseen to remove this ion species at the RF carpet (Sect. 3.2.3: Purity of the extracted ions). Therefore space-charge effects should mainly occur in the stopping region of the CSC, and space-charge effects at the RF carpets or in the nozzles, which have not been included in the simulations, should be small in comparison.

Finally, the expected increase in the rate capability has been verified experimentally with the prototype CSC. In this experiment, the DC cage has been replaced with a new DC cage that has only half the length of the original DC cage and a somewhat larger effective inner diameter [120, 121]. An increase in the rate capability by a factor of at least 20 has been achieved. A further reduction of the distance between the extraction electrodes by a factor of about 2, as in the design for the CSC of the Super-FRS, will thus result in the expected total gain in rate capability by at least three orders of magnitude.

Table 1 Expected performance of the stopping cell of the Super-FRS. In the standard mode, all performance parameters can be reached simultaneously (middle column). Alternatively, one of the performance parameters can be optimized at the expense of reducing the others. The optimum values achievable are given in the right column. They cannot be reached simultaneously

	Performance parameters in the standard mode	Optimum performance parameters
Areal density	$28\,\mathrm{mg/cm^2}$	$40\,\mathrm{mg/cm^2}$
Extraction efficiency	$\geq 50\%$	$\geq 70\%$
Mean extraction time	15 ms	$\leq 10\,\mathrm{ms}$
Rate capability	10^7 ions/s	3×10^7 ions/s

5.5 Expected performance characteristics

From the simulation results presented in this section and from the experimental results with the prototype CSC (Sect. 3), the performance characteristics of the CSC for the Super-FRS can be projected.

In the standard operation mode, the CSC will be operated with an areal density of about $28\,\mathrm{mg/cm^2}$, corresponding to a pressure of 200 mbar and a temperature of 70 K. As discussed in Sect. 2, this will correspond to a stopping efficiency close to unity for heavy and medium-heavy fragments produced at the Super-FRS.

For the prototype CSC, extraction efficiencies in the range of 50% to 80% for ions of many elements have been achieved (Sect. 3.2). Since the CSC for the Super-FRS will feature an even better cleanliness, an extraction efficiency in excess of 50% can be expected for ions of most elements. The simulations shown in Sect. 5.4 yield a rate capability of 10^7 ions/s.

For an array of eight RF carpets with an extraction nozzle in the center each, which are foreseen for the stopping region of the CSC, the average transport path will have a length of about 20 cm, depending on longitudinal and transverse stopping distribution of the ions. In the standard operation mode with a DC field of 100 V/cm, the average transport time of the ions in the stopping region will therefore amount to about 8 ms. In the extraction region, the average transport path will have a length of about 50 cm, and the traveling wave technique will be used for ion transport along the carpet. Transport velocities up to 75 m/s have been achieved for densities of $15\,\mu\mathrm{g/cm^3}$ [141]. Since the conditions in the extraction region are less challenging, higher velocities can be expected for the CSC. Hence, transport times of about 5 ms through the extraction region seem feasible. The transport time through the RFQ beamline will take about 2 ms. Therefore, mean extraction times of about 15 ms can be expected for the CSC of the Super-FRS.

The expected performance characteristics in the standard mode are summarized in Table 1. For experiments that require performance characteristics beyond these values, the operating conditions of the CSC can be adjusted and a different compromise between areal density, extraction time, rate capability, and mass range can be chosen. Thus, one of the performance parameters can be optimized at the expense of reducing the others. The optimum expected values thus cannot all be obtained simultaneously.

6 Technical design of the stopping cell

6.1 Overall setup

The digital mock-up of the HADO-CSC of the Super-FRS is shown in Fig. 29, including the RFQ beamline, the electric supplies, and the helium recovery unit (HRU). Note the definition of the coordinate system, which is used throughout this document. Figure 30 shows a cut through the CSC.

The CSC is mounted suspended in a holding frame. The outer, warm chamber and the inner, cold chamber are rectangular vacuum chambers. The top flange of the outer chamber is connected to the frame, and the body of the outer chamber is connected to the top flange. The top flange of the inner chamber is mounted from the top flange of the outer chamber by rods, and the body of the inner chamber is connected to the top flange of the inner chamber. The DC electrode structures (DC cages) and the RF carpets of the stopping region and the extraction region are located in the inner chamber. Most electronic supplies are also mounted on the frame of the CSC.

All connections for media (pumping, cooling, helium gas) and for the electrical components are made through the top flange of the outer chamber. The conceptual design for these connections is shown schematically in Fig. 31. The CSC uses 32 electrically driven Stirling cryo-coolers; in principle, the design allows for up to 80 cryo-coolers. Compared to the cryo-system of the prototype CSC, they feature a much improved reliability and reduced need for maintenance. The cryo-coolers are mounted on the top flange of the outer, warm chamber and connected to

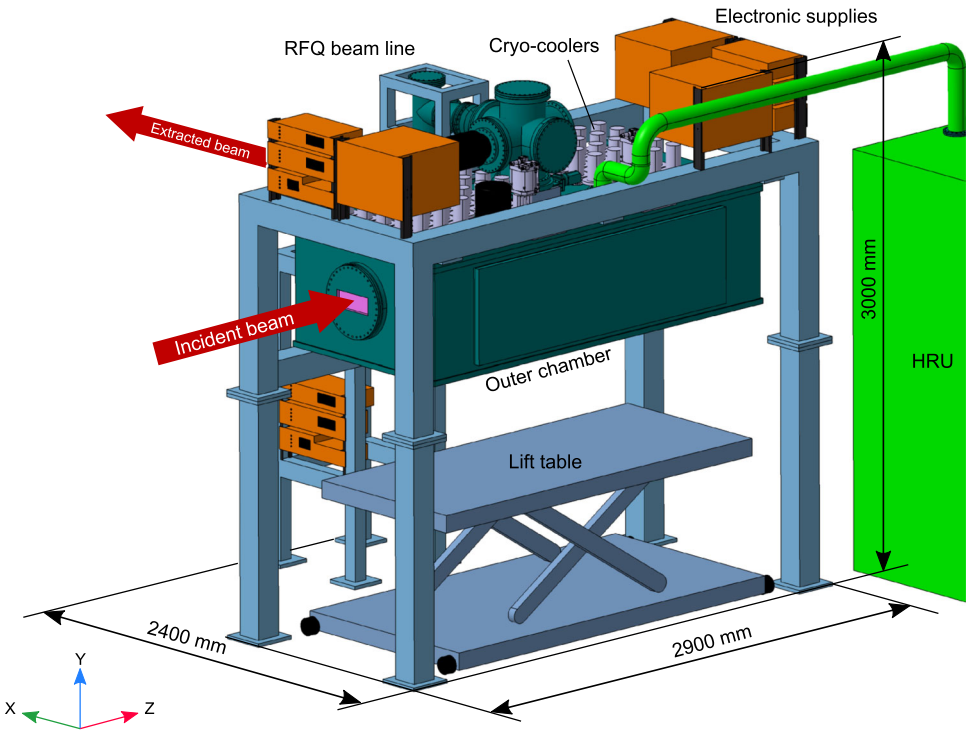

Fig. 29 Digital mock-up of the CSC including electronic supplies and the helium recovery unit. On top of the outer chamber, the RFQ beamline is mounted. A lift table (scissor table) is used to lower and raise the vacuum chamber for maintenance. To remove a dismounted vacuum chamber from under the frame, the lift table can be moved forwards and backwards. Note the definition of the coordinate system, which is used throughout this document

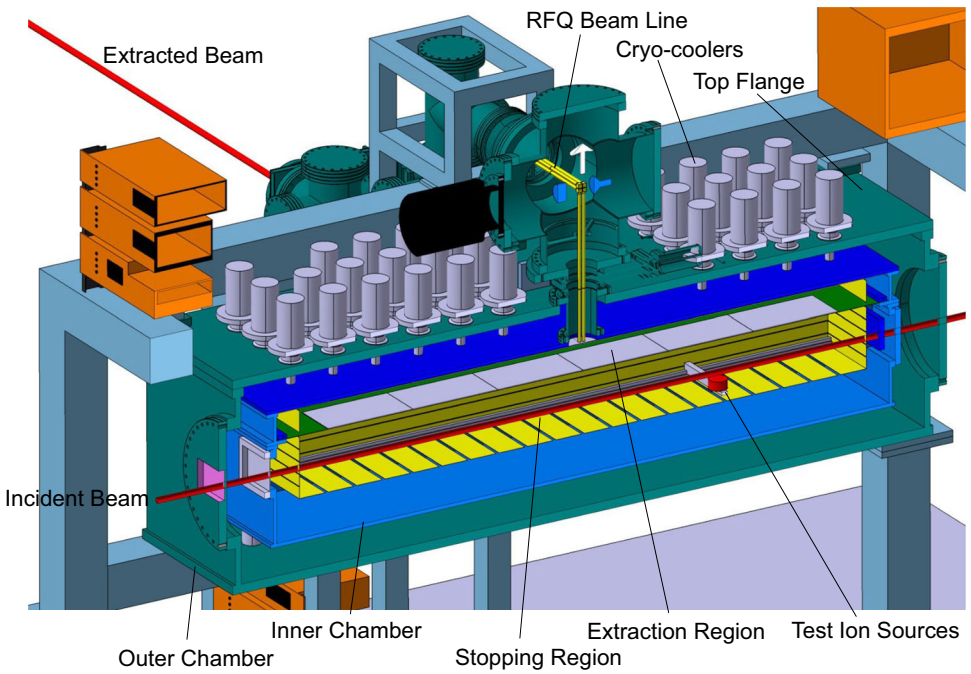

Fig. 30 Cross-section of the stopping cell showing the stopping and extraction chambers. The cryo-coolers are mounted on the top flange of the outer chamber. All connections to the stopping and extraction regions are made through the top flange. The DC electrode system is shown in yellow and the RF carpet in green. A module with test ion sources is mounted in the stopping region to test and optimize the ion extraction from the CSC

the top flange of the inner, cold chamber using copper braids. The helium stopping gas is fed into the CSC at room temperature; pre-cooling occurs in loops of the gas line that are in thermal contact with the top flange of the inner, cold chamber. A turbomolecular pump for evacuating the outer chamber is connected directly to the top flange of the outer chamber. The stopping and the extraction regions of the inner chamber are evacuated using two turbomolecular pumps; for normal operation with stopping gas in the CSC, the extraction region is connected to the HRU. The pump ports in the outer chamber are connected to the stopping and extraction regions by bellows. For normal operation, the pump port to the stopping region needs to be closed. This can be done using a cryogenic valve. Electrical connections to the stopping and extraction regions are made using flexible wires connected to feedthroughs mounted on the top flanges of the outer and the inner chamber.

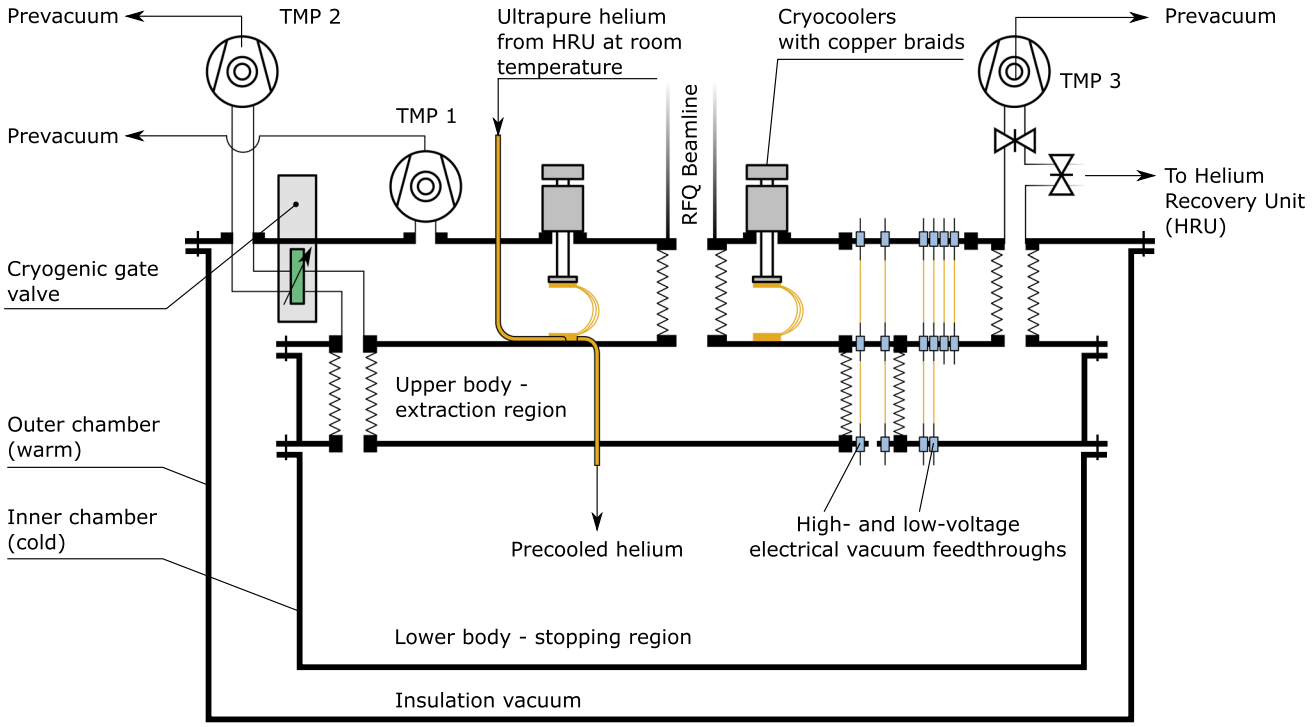

Fig. 31 Schematic figure illustrating the connections of the CSC. For details, see text

The bodies of the outer chamber and the inner chamber can be removed from the top flanges downwards in sequence using a lift table (scissor table). Since all connections to the CSC are made to the top flanges of the outer and the inner chambers, maintenance of the CSC is greatly simplified and can occur much faster than with the prototype CSC. After maintenance has been performed, the outer chamber and the inner chamber are mounted again in reverse order. Unless the extraction region needs to be accessed, no connections need to be removed or reinstalled; in this way, the maintenance is much less error-prone. An important further advantage of this arrangement is that the RF carpets of the stopping and extraction regions are mounted with their electrodes facing downwards. This prevents dirt and dust from settling on the finely structured electrodes of the RF carpets. This increases the operational reliability of the CSC.

The vacuum system of the RFQ beamline and the pulsed drift tube is built from DN160 and DN250 vacuum chambers and tubes. It is mounted in part on top of the frame of the CSC and in part on a separate frame. To decouple the CSC from the RFQ beamline without breaking the vacuum, a gate valve is installed on the top flange of the outer chamber of the CSC.

The outer dimensions of the complete system excluding the HRU are a length of 2.9 m, a width of 2.4 m, and a height of 3 m. The estimated mass of the system, including frame, cryo-coolers, pumps, and electronic supplies (without HRU), is about 4 t for a CSC with the outer and the inner chambers built from aluminum and about 5 t for the inner chamber built from aluminum and the outer chamber built from stainless steel. The dimensions of the CSC have been chosen, such that it will be possible to transport the CSC between the off-line laboratory in the Super-FRS supply building and its position in the LEB hall (see also Sect. 8). For transport, the feet of the main frame of the CSC, the RFQ beamline, and the additional frame for the part of the RFQ beamline can be dismounted from the main frame of the CSC.

6.2 Vacuum chambers

The outer chamber consists of two parts, a top flange and the body (Fig. 32). The chamber has a length of 2500 mm, a width of 1200 mm, and a height of 1200 mm.

The inner chamber consists of three major parts, a top flange, an upper body, and a lower body. A plate, which mounts the RF carpets and the feedthroughs, separates the lower and upper bodies into the stopping region and the extraction region. The lower body has a length of 2250 mm, a width of 700 mm, and a height of 500 mm. The upper body has a length of 2250 mm, a width of 700 mm, and a height of 100 mm. The top flange of the inner chamber accommodates feedthroughs and pump ports. It is mounted suspended from the top flange of the outer chamber.

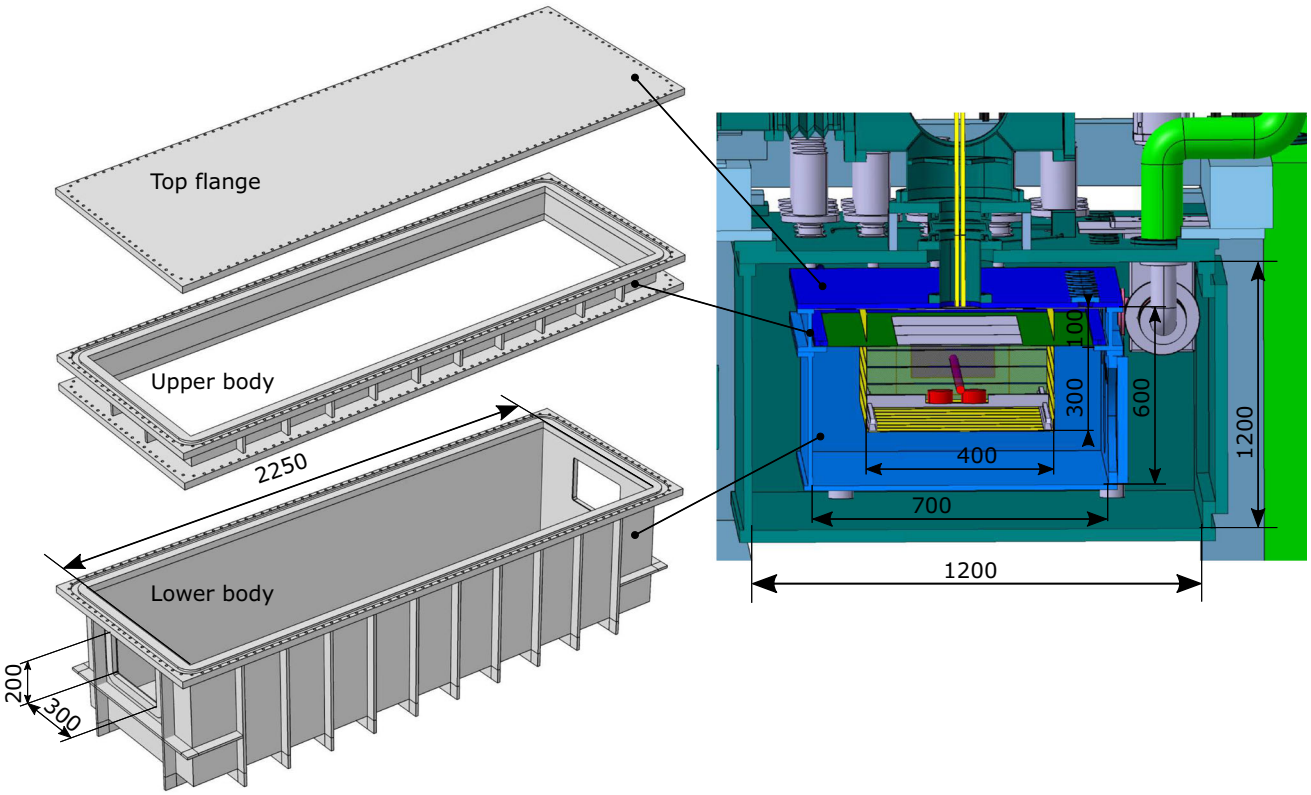

Fig. 32 Right panel: schematic figure showing a cut through the CSC including the outer vacuum chamber. Left panel: simplified technical drawings of the inner vacuum chamber consisting of top flange, upper body, and lower body. All distances are given in millimeters

Both the outer and the inner chamber are made symmetrically with beam windows on both sides to allow for a larger flexibility in the operation of the CSC. The windows have a width of 300 mm and a height of 200 mm. This cross-section fits the expected beam diameter at the final focus of the LEB. Four DN40 ports located in the bottom of each chamber allow access to the inside of the chamber from below. To increase the stiffness of the chambers, reinforcement ribs are used. The ribs are designed with the assumption that they hold half of the pressure load. There are 10 ribs each along the sides and bottom on the lower and the upper body of the inner chamber, and a total 36 ribs on the body of the outer chamber. The reinforcement ribs do not only increase the stiffness of the chamber but also reduce its total mass, which is beneficial for the cooling process and overall handling of the system.

The inner chamber and preferably also the outer chamber will be built from aluminum. Aluminum has a much higher thermal conductivity compared to stainless steel and allows for much shorter cool-down time (see Sect. 6.6). In addition, the weight of the vacuum chambers can be reduced significantly if they are built from aluminum. This is crucial for the handling of the chambers during maintenance and for the transport of the CSC between its location in the LEB hall and the off-line laboratory.

Simulations have been performed using the software package COMSOL Multiphysics 5.3 to determine the mechanical stress distribution on the outer and on the inner chamber. The model accounts for a pressure of 1 bar on the inner surface of the inner chamber, for 2 bar on the outer chamber, for gravity and for the thermal contraction due to cool-down from room temperature to a temperature of 70 K. The major requirement for the design is that the Von Mises stress under load does not exceed the maximum allowable stress for the given material. The maximum allowable stress for stainless steel 304 and for aluminum 6061-T6 are 150 MPa and 100 MPa, respectively. Figure 33 shows the Von Mises stress distribution for the lower body of the inner chamber for the case of aluminum. As it can be seen, the Von Mises stress is less than 100 MPa, which satisfies the aforementioned requirement. As a result of the calculations, a minimum thickness of the chamber walls of 3 mm and 4 mm has been determined for stainless steel and aluminum, respectively.

It is non-trivial to ensure a leak-tight sealing at cryogenic temperatures for a rectangular flange with the size of the inner chamber. Normally, for smaller chambers, CF knife-edge flanges with metal gaskets are used. However, the knife edge needs to be machined with a tolerance of about 10 µm over a perimeter of 6 m. Further, the gasket needs to accommodate thermal contraction. Additionally, a direct flange-to-flange contact is desirable for

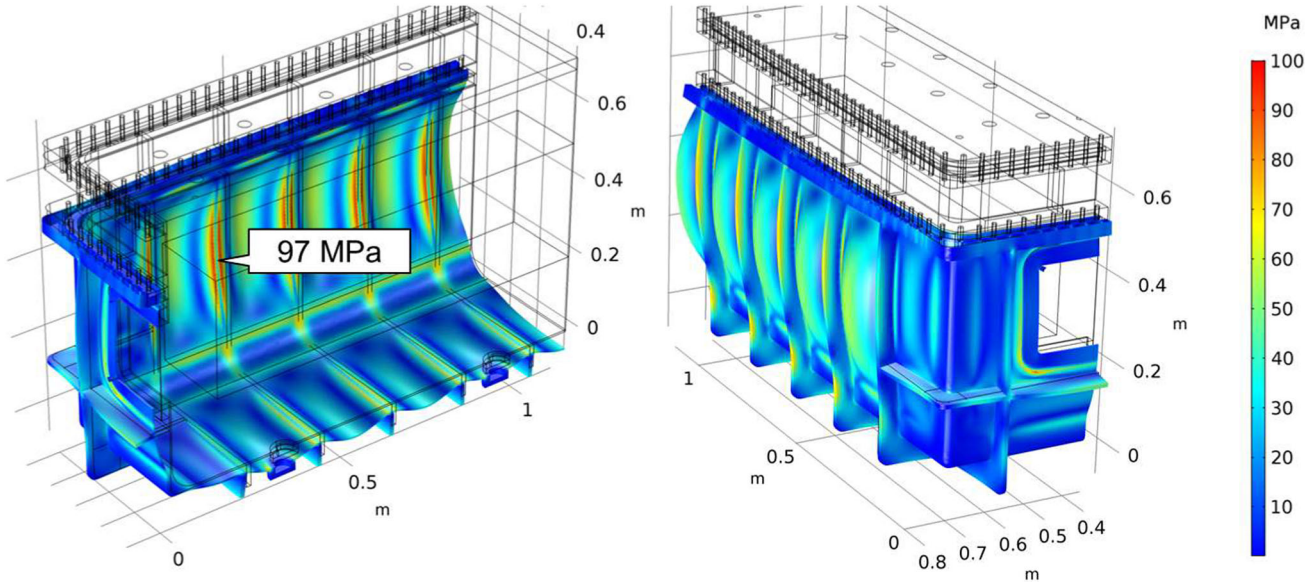

Fig. 33 Calculated stress distribution in lower body of the inner chamber. A quarter of the original model was computed with symmetry boundary conditions. Deflections are exaggerated for easier visualization

cool-down. This is hard to reach with CF flanges. Therefore, Helicoflex gaskets (Technetics Group) will be used instead of CF gaskets. Helicoflex gaskets consist of two parts, an inner helical spring and an outer soft metal jacket. The spring is selected to have a specific compression resistance. During compression, the spring pushes the jacket toward the flange-sealing surface. The jacket deforms permanently and fills the flange imperfections while ensuring reliable contact. Each coil of the helical spring acts independently and allows the seal to conform to surface irregularities on the flange surface. With heliconflex gaskets, flanges with a groove instead of a knife edge can be used. The outer chamber will be sealed using Viton gaskets.

6.3 Electrode system and RF carpets

As discussed in Sects. 4 and 5, ion transport in the CSC will occur at two different densities. In Fig. 34, this motion is shown schematically. In the stopping region, DC fields drive the ions onto an array of 8 circular RF carpets, each with a size of 250 mm × 250 mm, an electrode density of 6 electrodes/mm, and a nozzle with a diameter of 0.6 mm. An RF voltage (peak-to-peak) up to 150 V at a frequency of 15 MHz and a radial DC field in the direction of the nozzle is applied. After the ions have been swept out through one of the nozzles and transported in the gas jet in the extraction region, they are collected on a large RF carpet with an electrode density of 2 electrodes/mm, which is built from several segments. An RF voltage (peak-to-peak) up to 150 V at a frequency of 3 MHz and a radial DC field in the direction of the exit nozzle is applied. In order to collect the ions over the full length of the CSC and to focus them on a single nozzle, the electrode geometry represents a rectangular cut-out with a length of 2000 mm and a width of 250 mm from a large circular or elliptical RF carpet. Simulations show that no significant losses are to be expected at the edges of the carpet, since the ion motion occurs almost straight in the direction of the radial DC field. The RF carpet in the extraction region is operated with the traveling wave technique to increase the transport velocity of the ions along the carpet [127].

Apart from their different size and electrode density, the RF carpets will be built in a similar way as the RF carpet of the prototype CSC using PCB material and an electrode width-to-gap ratio of about 1:1 (Fig. 9). They will also have two inner layers between the front electrodes and the backside of the carpets to control the field penetration through the ring electrodes and to provide a fine control of the DC field in front of the electrodes. The resonant circuit of the RF carpet of the prototype CSC has a quality factor of about 30. Larger values are disadvantageous, since large variations in the RF voltage would occur with changes of the resonance frequency due to temperature changes. The limited quality factor causes the dissipation of power in the resonator (coil and capacitance) and leads to an increased temperature of the stopping gas. Therefore, the possibility will be investigated to drive the RF carpets of the CSC for the Super-FRS non-resonantly. In a non-resonantly-driven system, a higher RF power is required to drive the load presented by the electrodes. However, this RF power is mainly dissipated in the generator (at room temperature) and not in the load (at cryogenic temperature). The RF voltage is generated outside the CSC by several RF amplifiers (sinusoidal excitation) and fed to the electrodes of

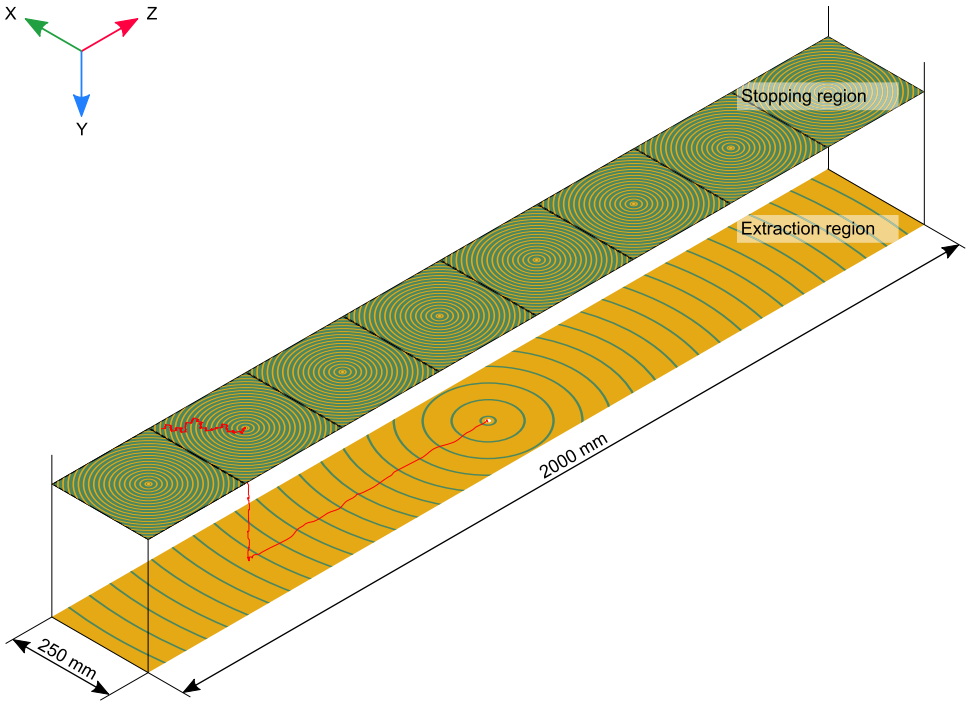

Fig. 34 Schematic figure of the layout of the RF carpets in the stopping region and in the extraction region. In the stopping region, eight high-density carpets are used with eight nozzles; in the extraction region, the ions are collected using an RF carpet with a single extraction nozzle. A schematic ion trajectory is shown to illustrate the ion motion along the carpet. Note that the figure is inverted (stopping region on top and extraction region below)

the RF Carpet with coaxial cables. As in the prototype CSC, the RF carpets are also equipped with circuits for direct measurement of the RF amplitude during operation.

The electrode system (DC cage) of the stopping region has a length of 2000 mm, a width of 400 mm, and a height of 300 mm. The size of the DC cage is larger than the required active volume of the CSC, since other elements such as test ion sources need to be mounted inside the DC cage, and because the extraction efficiency is smaller close to the electrodes than in the bulk of the stopping region. To a certain extent, the ions can be focused onto the RF carpets, which have a width of 250 mm. Furthermore, the larger DC cage allows changing the vertical distance between the beam and the RF carpets. In this way, it will be possible either to maximize the effective stopping volume (larger distance) or to minimize the extraction time and maximize the rate capability (smaller distance). The sides of the DC cage are built from overlapping electrodes as indicated in Fig. 23. The lower part of the DC cage (anode) is built either from segmented electrodes or from PCBs (DC carpets) with a large structure size ($\sim$ 2 mm per electrode). The segmentation allows applying a similar electric DC potential distribution to the anode as to the upper RF carpets (see Sect. 5.1), increasing the extraction efficiency. Furthermore, it allows the position-resolved detection of the ionization in the stopping cell, from which the stopping distribution can be determined. The windows on the DC cage are formed by a coarse mesh of thin wires (diameter $\sim 50\,\mu$m). Thus, desorption of atoms and molecules from the windows is reduced. Ions desorbed from the windows of the cold chamber can be prevented from entering the DC cage by a positive voltage offset on the windows of the DC cage.

For testing the ion transport in the CSC and the extraction of ions from the CSC, two α recoil ion sources (^{228}Th, $\sim$ 20 kBq, half-life of 1.9 years) are used, which are mounted at different horizontal positions along the bottom of the DC cage. They allow determination of extraction efficiencies and extraction times with high precision. Two weak ^{252}Cf fission sources ($\sim$ 40 kBq) are installed in the DC cage to test the ion extraction over a wide mass range and to investigate and optimize the charge states of different elements extracted from the CSC. In addition, two discharge ion sources similar to that used in the prototype CSC [100] are mounted at the bottom of the DC cage; they allow testing the operation of the CSC off-line at high ionization densities and investigating the cleanliness of the stopping gas.

The DC cage of the extraction region has a length of 2000 mm, a width of 400 mm, and a height of 100 mm. It is built in a similar way as the DC cage of the stopping region.

6.4 RFQ beamline

The separation of the ions from the stopping gas, the separation from contaminant ions, the diagnostics of the extracted ions, and the cooling and bunching of the ions before transport to the MATS-LaSpec hall are performed in a similar RFQ beamline as the one for the prototype CSC at the FRS Ion Catcher [47, 48, 73]. Compared to a conventional approach, i.e., an RFQ for beam formation, an electrostatic beamline, and a dipole magnet, the

RFQ beamline has many advantages. The operation of the RFQ beamline is compatible with the relatively high buffer gas pressure in the vicinity of the CSC, it is easy to tune and has a high transmission efficiency. Additional functionality can be readily implemented, such as mass-selective operation and collisional dissociation. An RFQ mass filter has been shown to possess excellent performance characteristics [73]. In contrast to a dipole magnet, it can be easily set to transmit a larger range of mass ratios, which has been proven to be very useful during the commissioning of the FRS Ion Catcher, and which is also required for measurements that are performed simultaneously on several nuclides with different mass numbers, e.g., for MNT studies. The combination of a twofold mass separation with collisional dissociation (IDI) is a powerful and efficient method to remove even strong isobaric molecular contamination (Sect. 3.2.3: Purity of the Extracted Ions), much superior to a single mass-separation stage in a magnetic dipole, which cannot separate isobars. Furthermore, the RFQ beamline can be easily dismounted in case other experiments are to be performed at the focal plane FLF6 of the LEB.

The RFQ beamline is shown schematically in Fig. 35. The ions are separated from the stopping gas in the extraction RFQ that guides the ions upwards. The extraction RFQ can also be used as a mass filter to provide a coarse mass separation. Behind the extraction RFQ, an RFQ segment is mounted on a sled, which can be moved using an in-vacuum step motor and gear system in a similar way as at the FRS Ion Catcher (Sect. 3.2.2). It can thus make way to close the gate valve mounted on top of the CSC. The RFQ beamline contains a dedicated RFQ mass filter, which will be used to separate the ions of interest from other isotopes and from contaminant ions with a different mass number. Collision-induced dissociation can be performed in the horizontal part of the RFQ beamline on top of the CSC. The RFQ beamline includes two RFQ switchyards [115, 142] (Sect. 3.2.2). At each RFQ switchyard, behind the extraction RFQ and behind the RFQ mass filter, a channeltron detector and a silicon surface-barrier detector are mounted to detect the ions extracted from the CSC and to optimize the transmission efficiency. The silicon detectors can be tested and calibrated using a three-line α source (^{239}Pu, ^{241}Am, ^{244}Cm) each. The RFQ switchyards also allow the introduction of ions generated using a thermal cesium ion source and an electron impact ion source. At the end of the RFQ beamline the RFQ buncher is installed. It cools the ions and produces ion bunches, which are shifted in the electric potential by about 5 kV in the pulsed drift tube [93–95] located downstream of the RFQ buncher. Another cesium ion source and set of detectors consisting of channeltron detector and silicon surface-barrier detector can be moved into place in the location of the pulsed drift tube to measure the ions extracted from the RFQ buncher. It should be noted that such an RFQ beamline, including RFQ switchyard, movable RFQ, detectors, and test ion sources, despite its novel approach and features, has already been tested successfully at the FRS Ion Catcher off-line and on-line and is in routine operation.

The RFQ beamline is built from rods of resistive carbon-filled PEEK with a rod diameter of 11 mm and a radial distance of 10 mm. It is operated with RF voltages with amplitudes of a few hundred volts and frequencies of about 1 MHz. Four separate RF generators and resonant circuits are used to provide the RF voltages for the extraction RFQ, the RFQ mass filter, the RFQ buncher, and the other sections of the RFQ beamline. A longitudinal electric field can be created along the RFQs in the beamline by applying a voltage difference of a few volts between the ends of the RFQ rods [80, 109]. In the RFQ beamline, helium is used as buffer gas. It flows into

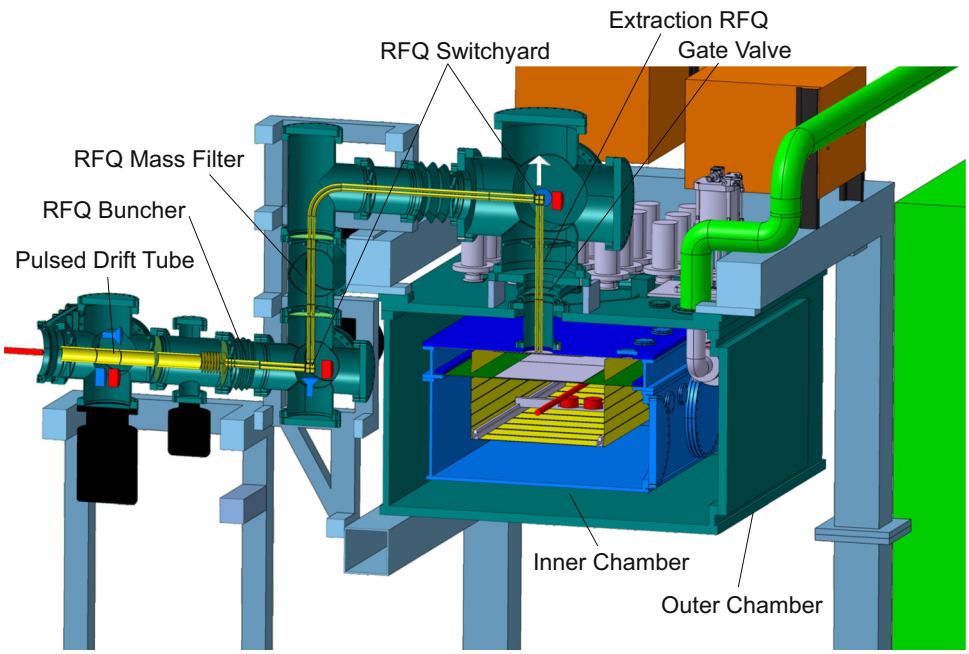

Fig. 35 Cross-section of the stopping cell showing the extraction elements

Table 2 Expected parameters for ion bunches extracted from the RFQ buncher consisting of up to 10^4 singly charged ions with a mass of 100 u

Longitudinal emittance (FWHM)	0.5 eVμs
Transverse emittance (standard deviation) at 5 keV	$\leq 1\pi$ mm mrad
Relative energy spread	0.1%
Initial time spread	100 ns

the extraction RFQ from the CSC, and in addition, it can be introduced into the cooling sections of the RFQ beamline. Differential pumping is applied in the different sections of the RFQ beamline. The section of the mass filter is pumped to a pressure of better than 10^{-4} mbar, the other sections are operated at pressures in the range from a few 10^{-3} mbar to 10^{-2} mbar. The mass filter contains Brubaker lenses [143] at its entrance and exit to improve transmission efficiency and mass resolving power. A mass resolving power of up to 200 can be achieved at a transmission efficiency of 90% [73]. The RFQ buncher contains two RFQ segments and an aperture at its end. A DC voltage offset is applied to the last RF segment, such that ions are stored in the middle of this segment. For extraction, the aperture is pulsed to a lower potential, such that an ion packet is extracted from the RFQ buncher. Based on previous work, a longitudinal emittance (FWHM) of the ion bunches of about 0.5 eVμs is expected for singly charged ions with a mass of about 100 u [73]. For the transverse emittance (standard deviation), a value of 1π mm mrad or better is expected at an energy of 5 keV. To minimize any distortions resulting from the voltage switching in the pulsed drift tube, the time-focus of the ion bunches extracted from the RFQ buncher is placed in the pulsed drift tube. For the relative energy spread, a value of 0.1% is chosen at an energy of 5 keV/charge, such that at the time-focus, the ion bunches have a temporal spread of about 100 ns. The energy spread leads to an additional time spread of the ion bunches, which amounts to about 5 ns per meter traveled in the beamline. It is hence small compared to the initial temporal bunch width and should allow for an efficient capture of the ions bunches in the MATS-LaSpec cooler and buncher [13]. The expected parameters of the ion bunches extracted from the RFQ buncher are summarized in Table 2.

The pulsed drift tube has a length of 50 cm. It is operated with a push-pull high-voltage switch; such switches are available with rise/fall times of 200 ns or better. During ion extraction from the RFQ buncher, the pulsed drift tube is held at a voltage of -5 kV, while the RFQ beamline is operated at a potential close to ground, such that the ions are accelerated by a potential difference of 5 kV. When the ion bunch is inside the drift tube, the pulsed drift tube is switched to ground potential. For singly charged ions with a mass of 100 u the flight time through drift tube amounts to 5 μs. This time is much longer than the temporal bunch width and the rise time of the high-voltage switches, such that in principle, it should be possible to make a broadening of the energy spread of the ions due to imperfections in the high-voltage switching small compared to the energy spread arising from the pulsed extraction from the RFQ buncher. However, even a doubling of the energy spread would only increase it to a value of 10 eV; ions with this energy spread can be readily captured in the MATS-LaSpec cooler and buncher.

6.5 Pumping system

The eight cylindrical nozzles in the stopping region with a diameter of 0.6 mm each have a combined conductance of about 0.5 l/s, corresponding to a flow rate of 400 mbar × l/s at room temperature. Assuming a total time of 4 months of off-line and on-line operation of the CSC per year, the consumption of He 6.0 will amount to about 500 bottles with a total cost of about 100 kEUR. To keep the operational cost of the CSC at a reasonable level, the helium stopping gas therefore needs to be recovered and re-used. The recovery needs to be implemented, such that any contamination of the helium gas is avoided. Thus, a helium recovery unit (HRU) using high vacuum technology will be used [144], similar to the one developed for the PALIS stopping cell at RIKEN [131]. An important further advantage is that the helium gas can circulate in the CSC for many cycles and can be further purified at each cycle using getters. Thus, the purity of the stopping gas increases far beyond the level achievable without the HRU.

The design of the pumping system for the CSC is shown in Fig. 36. The extraction region is pumped by the HRU. To keep the conditions (in particular the gas density) in the extraction region constant, i.e., independent of the gas density in the stopping volume, the pumping speed of the HRU can be varied; in addition, the conductance from the extraction region to the HRU can be adjusted using a butterfly valve. The HRU compresses the helium, which flows back into the stopping region through an active getter. A recovery efficiency of at least 98% is expected. To compensate the minor losses in helium and to ensure stable working conditions, an automated helium refilling system is used. The cleanliness of the helium gas that is fed into the HRU from the refilling system is purified using an active getter and a cold trap. The cold trap is needed to remove gases that are not removed by the getter, such as noble gases. Using special purification getters and a leak valve system, it will be possible to mix the stopping gas with minor quantities of other gases for charge exchange with the thermalized ions, such as neon, methane, nitrogen, or oxygen.

The helium gas purity needs to be monitored on the ppb level to ensure a proper operation of the CSC. This is achieved using different methods and at different positions in the system. A residual gas analyzer (RGA) monitors

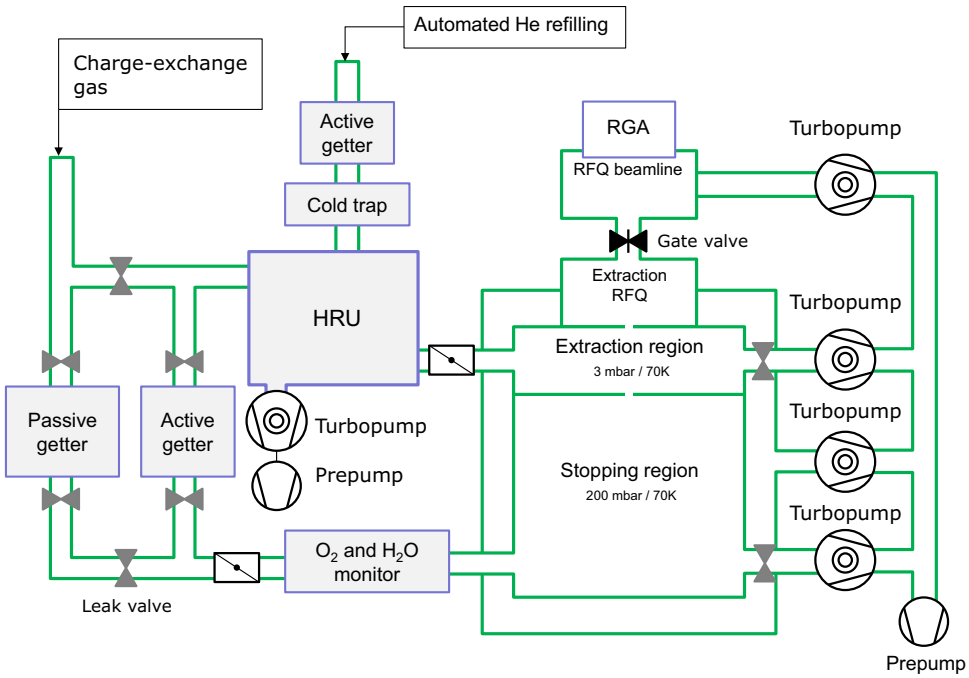

Fig. 36 Schematic figure illustrating the design of the pumping system for the CSC. Note that the scheme does not reflect the real positions of the pumping ports

the quality of the gas flowing from the CSC and determines the amount of trace gases in the system. A hygrometer is used to detect traces of water in the stopping gas over a larger dynamic range. Directly after the start-up of the system water will be the main contaminant, because the walls of the chamber and tubing have been exposed to ambient air, e.g., after maintenance on the CSC. An oxygen analyzer is used to detected traces of oxygen in the stopping gas on the level below 10 ppb. This will be the most sensitive measurement on the amount of trace gases in the system.

Turbomolecular pumps and a rough pump are used to evacuate the system. Safety valves are installed in the pumping system, which avoid overpressure and damages, e.g., to the RF carpets. Furthermore, all vacuum pumps are equipped with emergency valves, which close in case of a power failure and preserve the vacuum and thus the cleanliness of the system. The HRU has an approximate length of 2.5 m, a width of 1.5 m, and a height of 2.4 m; its mass amounts to about 1.8 t.

6.6 Cryo-system

The cooling power for the CSC will be provided by an array of free-piston Stirling cryo-coolers, e.g., the Cryotel GT cryo-cooler (Sunpower, Inc.). Each cryo-cooler has a cooling power of 16 W at a temperature of 77 K and reaches a lowest temperature of 40 K. The cryo-coolers are driven electrically and are cryogen-free and compact. A decisive advantage compared to the cooling system of the prototype CSC is a mean-time-to-failure of 200,000 h and a practically maintenance-free operation. This is due to their frictionless bearings; this sets them apart from other types of cryo-coolers. With the cooling system of the prototype CSC, the cost and time required for maintenance has proven to be a major issue. For conventional compressor-driven cryo-coolers (e.g., Cryomech AL200 GM) maintenance is required at least every two years, and the expected mean-time-to-failure (with proper maintenance) amounts to about one-third of that of a Sunpower CryoTel GT cooler.

The cryo-coolers are mounted on the top flange of the outer chamber. The cold heads are linked to the top flange of the inner, cold chamber via flexible copper braids. The copper braids allow for the contraction and avoid mechanical stress on the inner chamber during the cooling process. The external part of the cryo-coolers (pressure vessel) are attached to the top flange of the outer chamber and are at ambient temperature. The heat rejection from the cryo-cooler is provided by an external heat exchanger. Typical compressor-driven cryo-coolers can be safely heated up only to temperatures of about 350 K. Since the cryo-coolers need to be connected directly to the vacuum chamber, this temperature limit does not allow for a proper bake-out of the CSC. However, the cryo-coolers that will be used for the CSC can be water-cooled and heated up to 420 K. Hence, proper bake-out of the CSC can be performed.

The heat load expected for the CSC is summarized in Table 3. The heat load of the helium stopping gas is estimated as 160 W. The heat generated by the RF carpets is estimated from the heat deposition of the RF carpet of the prototype CSC to be about 5 W, scaled to the overall area and RF frequency of the RF carpets of the CSC

Table 3 Heat sources and estimated heat input budget for the CSC

Heat Source	Heat Input/W
Circulating buffer gas (He)	160
RF carpet	100
Radiative heat flux	7
Cables	< 1
Suspension system	3
Total	270

of the Super-FRS; it amounts to 100 W. The radiative heat flux is reduced using super-insulation. In addition, electropolishing of the chambers reduces the emissivity coefficient of the surfaces. The radiative heat flux is then estimated to about 7 W. For the cabling, 250 Manganin and 40 copper wires with the diameters of 0.14 mm and 0.25 mm, respectively, are considered. The average length of a wire is 0.4 m. Manganin wires have lower thermal conductivity, and therefore, a smaller heat input. Copper wires are used in high-power applications to minimize energy dissipation. Heat input through the suspension system of the inner chamber considers the use of 16 stainless steel rods of 8 mm diameter with the average length of 1 m; it is estimated to be 3 W.

The cool-down was studied by simulations with COMSOL Multiphysics 5.3. Calculations were performed for the inner chamber built from stainless steel 304 and from aluminum 6061-T6 taking into account the heat input given in Table 3 and 32 cryo-coolers with a total cooling power of 512 W at a temperature of 77 K. The conductive heat transfer through the buffer gas is included in the model by increasing the value of the thermal conductivity coefficient of helium by a factor that is given by the Nusselt number. The results are shown in Fig. 37. In the case of the stainless steel chamber, the cool-down is strongly limited by the poor thermal conductivity of the material. Aluminum, on the contrary, possesses a thermal conductivity that is higher by an order of magnitude. Another point of consideration is the temperature gradient between the different parts of the inner chamber. Since all the cooling power is located on the top flange of the inner chamber, the different parts of the inner chamber have different cool-down times. Temperature gradients result in unwanted mechanical stress, since the parts experience thermal contraction to variable degrees. This effect is pronounced for stainless steel due to its low thermal conductivity: temperature differences of more than 130 K arise in the flange of the chamber. For a chamber built from aluminum, the temperature differences are much smaller. For an aluminum chamber the cool-down takes about 24 h, until the helium stopping gas reaches a temperature of 70 K. For a stainless steel chamber, it takes twice as long. In addition, the weight of the vacuum chamber can be reduced significantly if it is built from aluminum. Because of these advantages, aluminum has been chosen as material for the inner chamber.

Figure 38 shows the simulated cool-down for different numbers of cryo-coolers. A minimum of about 20 cryo-coolers is required to balance the expected heat load at a temperature of 70 K. However, then the cool-down takes much longer than a day. From the experience with operation and maintenance of the prototype CSC, 1 day has

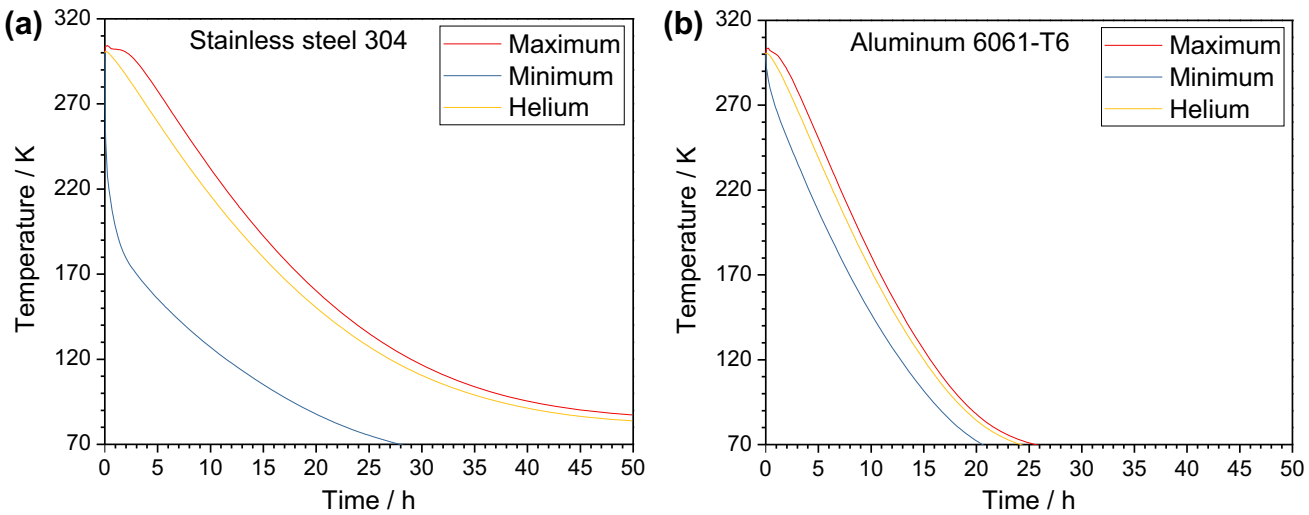

Fig. 37 Simulated maximum and minimum temperatures of the inner chamber and the temperature of the helium buffer gas during the cool-down **a** for stainless steel and **b** for aluminum

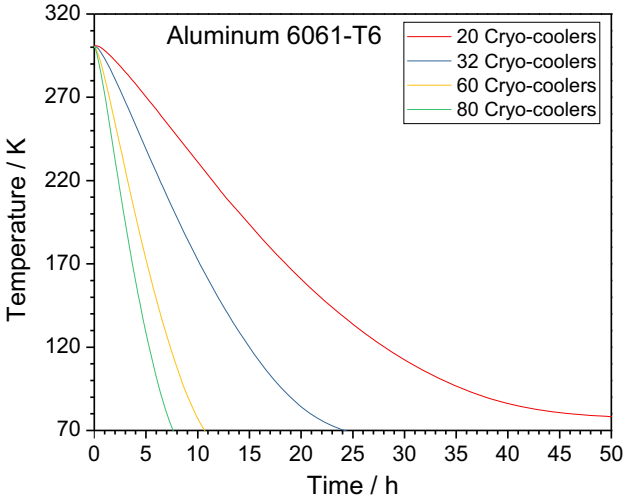

Fig. 38 Simulated temperature of the helium buffer gas during the cool-down of the inner chamber built from aluminum for different numbers of cryo-coolers

been established as a reasonable cool-down time. For 60 and 80 cryo-coolers, the time required to reach a helium temperature of 70 K can be reduced to less than 11 h and 8 h, respectively. As the best compromise between short cool-down time and costs, the number of 32 cryo-coolers has been chosen. An alternative to the Cryotel GT cryo-cooler is the newly introduced Cryotel DS30. It has the same technology and thus the same advantages as the GT16, but it has twice the cooling power at less than twice the price. In the case of the Cryotel DS30, 16 cryo-coolers would be required.

Conventional compressor-driven cryo-coolers are available with significantly higher cooling power (e.g., 160 W at 70 K for the Cryomech AL200 GM). In their case, only three cryo-coolers would be required for cooling of the CSC. While the initial investment costs of the solution with the free-piston Stirling coolers is therefore higher, over the envisaged lifetime of the system (e.g., 20 years), it is significantly less expensive due to savings in maintenance cost and costs for replacements. Furthermore, it increases the reliability of the operation of the CSC and reduces the down-time. Even in case of a failure of one or even a few of the Stirling coolers, operation of the CSC would not be significantly affected. In contrast, every failure of a more powerful compressor-driven cooler would endanger operation of the CSC until the cooler could be exchanged. The solution with the free-piston Stirling coolers also reduces the work required on the system, because maintenance on the coolers is not required. The larger number of coolers should not be a significant disadvantage, since they will be mounted on the top of the CSC, while maintenance of the CSC will be performed from below, i.e., only in rare cases, the coolers will need to be dismounted. Also, the larger number of coolers allows a more homogeneous distribution of the cooling power on the top flange of the inner cold vacuum chamber.

As in the prototype CSC, the CSC for the Super-FRS is baked to a temperature of 420 K using heating cartridges prior to cool-down to achieve optimum cleanliness of the stopping cell. The heating cartidges also allow for a fast warming-up of the CSC for maintenance.

6.7 Detectors at the final focal plane of the LEB

At the final focal plane FLF6 of the LEB, two detectors of different types, degraders and slits, are needed in front of the CSC for a successful execution of experiments with the CSC (Fig. 39). They are all mounted at air.

The degrader is of variable thickness. It is needed to slow down the ions and to adjust the energy of the ions of interest to be stopped in stopping volume of the CSC. Depending on the range of the ions of interest, either a solid variable homogeneous degrader (two anti-parallel wedges) or for the heavy low-range fragments a gas degrader (gas volume with variable pressure) [72] will be used. For the solid degrader, the components (incl. drives) of the degrader system currently used at the FRS Ion Catcher will be adapted and transferred to the Super-FRS. This degrader system has three components, disks, wedges, and plates. The disks will be used at FLF5 for the range bunching; the wedges and plates (needed for very light and larger range fragments) will be installed with a new support frame at FLF6. In case of heavy fragments with a very short range, the minimum thickness of the wedges (about 600 mg/cm^2, depending on beam size) may be too large, such that the ions are already stopped in the degrader and do not reach the CSC. In this case a gas degrader will be used instead of the solid degrader. The gas degrader consists of a vacuum vessel with thin windows (e.g., 100 µm Kapton), which is filled with a gas (nitrogen or SF_6). The pressure in the vessel can be varied between vacuum and 1 bar overpressure (controlled with an accuracy of 0.2%). With a chamber of 0.5 m length, this allows to adjust the areal density of the degrader between 40 and 160 mg/cm^2 for nitrogen and 40 and 630 mg/cm^2 for SF_6.

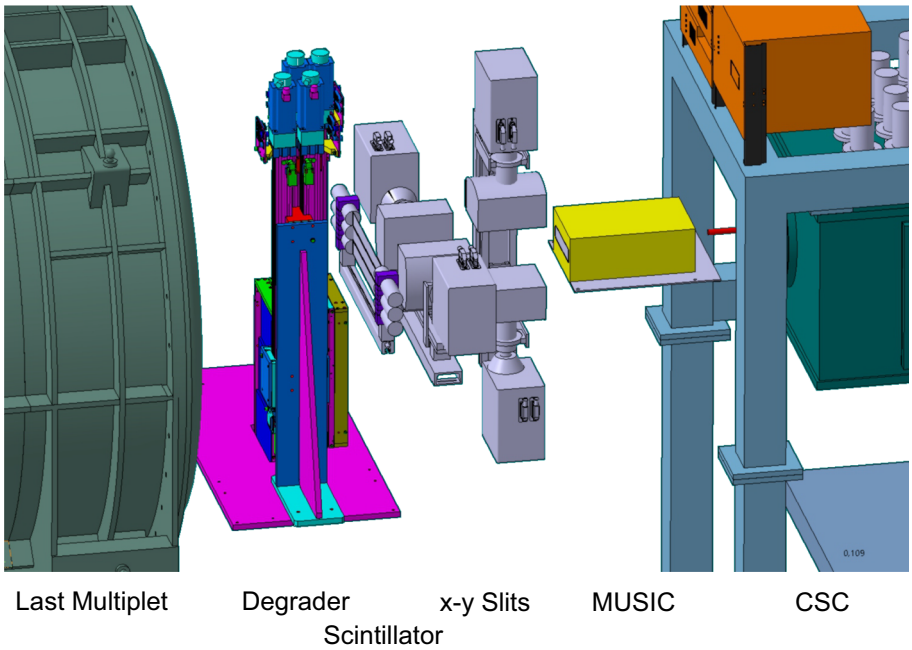

Fig. 39 Schematic view of the setup at the final focus at the LEB (FLF6), showing the degrader, detectors, and slits between the last multiplet and the CSC

A scintillator that allows for position determination in horizontal direction will be used to count and measure the position of the ions in front of the CSC. A detection area of 400 mm × 150 mm and a position resolution of a few millimeters are required. To handle the rates at the LEB of up to 10^7 ions/s, two approaches are possible, either to use a single scintillator plate for rates up to 10^6 ions/s, or to segment the detector in the vertical direction for higher rates. The latter approach would result in more complex electronics, but would allow to measure also at the highest rates and add position measurement in the vertical direction.

A multiple-sampling ionization chamber (MUSIC) [106, 107] is needed to measure the stopping position to adjust the variable degrader. Its active area amounts to 400 mm × 150 mm. Because only the stopping position and not the charge is measured a low-resolution, simplified version (4 electrodes and 20 cm length) is sufficient. The MUSIC will also allow for a more precise position measurement in the vertical position.

For a final selection of the fragment of interest and to constrain and define the phase space of the stopped ions, horizontal and vertical slits are necessary in front of the CSC. This slit system will be similar to the one in the Super-FRS, but it will be in air and have a smaller thickness, corresponding to the lower energy and thus lower range of the particles in the LEB as compared to the main separator of the Super-FRS.

6.8 Transfer beamline to MATS and LaSpec

The transport of the ions from the CSC to MATS and LaSpec will be done with an electrostatic low-energy beamline according to the conceptual design discussed in Sect. 2.3. The part of this beamline, which is located in the LEB hall, is part of this document (see also Fig. 42). The beamline has a height of 2.1 m and a length of about 6 m to the wall of the LEB hall. The ions are accelerated to a transport energy of 5 keV per charge in the pulsed drift tube located at the exit of the CSC. Focusing of the ions is performed using electrostatic quadrupole doublets.

The required size and separation of the electrostatic quadrupole elements can be estimated following the discussion in [145]. The basic requirements with respect to the beamline acceptance, stray magnetic fields and space-charge, respectively, can be put down to

$$L_\mathrm{c} < r_\mathrm{c}^2/\epsilon; \qquad L_\mathrm{c} \ll (\rho_\mathrm{m}^2\epsilon)^{1/3}; \qquad L_\mathrm{c} \ll \frac{\epsilon\beta V_0}{I \cdot 30\Omega}, \tag{4}$$

where L_c is the separation of the quadrupole doublets, r_c their aperture radius, ρ_m the radius of curvature of the ion path in the magnetic field, ϵ is the beam emittance, β the ion velocity in units of speed of light, V_0 the ion acceleration potential, and I the ion current. For a beam emittance of $\epsilon < 200\ \pi$ mm mrad, the first requirement is easily fulfilled for standard aperture radii of $r_0 = 20$–50 mm. The constraints of the latter two requirements are presented in Fig. 40. Assuming a stray magnetic field of 0.7 G, a doublet separation of 1 m ensures that the beam displacement due to the magnetic field is smaller than the beam size for all but the lightest isotopes. For

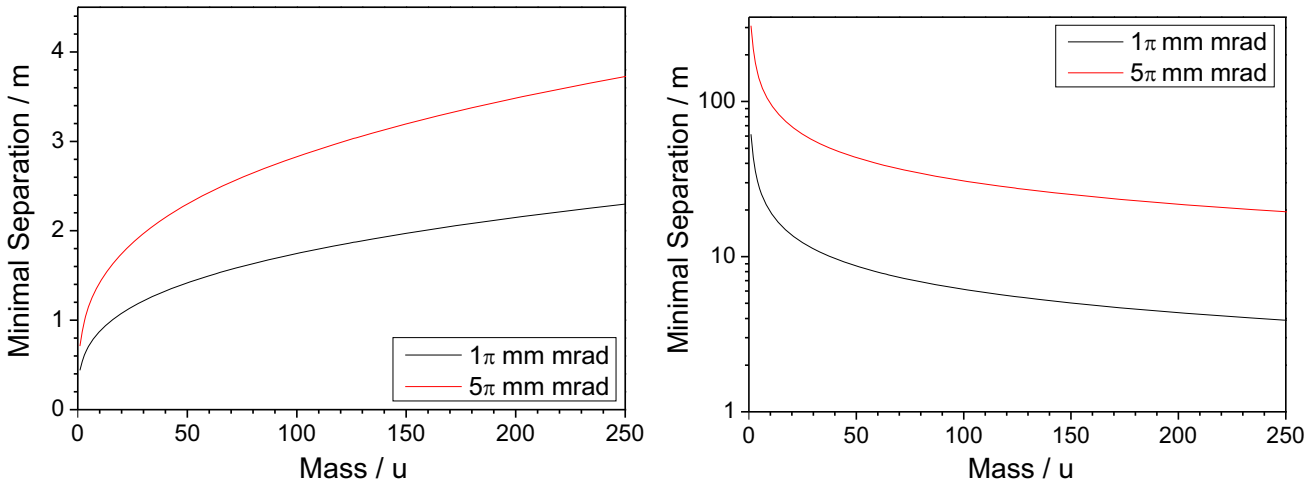

Fig. 40 Left panel: smallest admissible quadrupole doublet separation for a displacement due to a stray magnetic field of 0.7 G to be smaller than the beam size. Right panel: smallest admissible quadrupole doublet separation for the effect of space charge to be negligible, assuming 10^5 particles per bunch

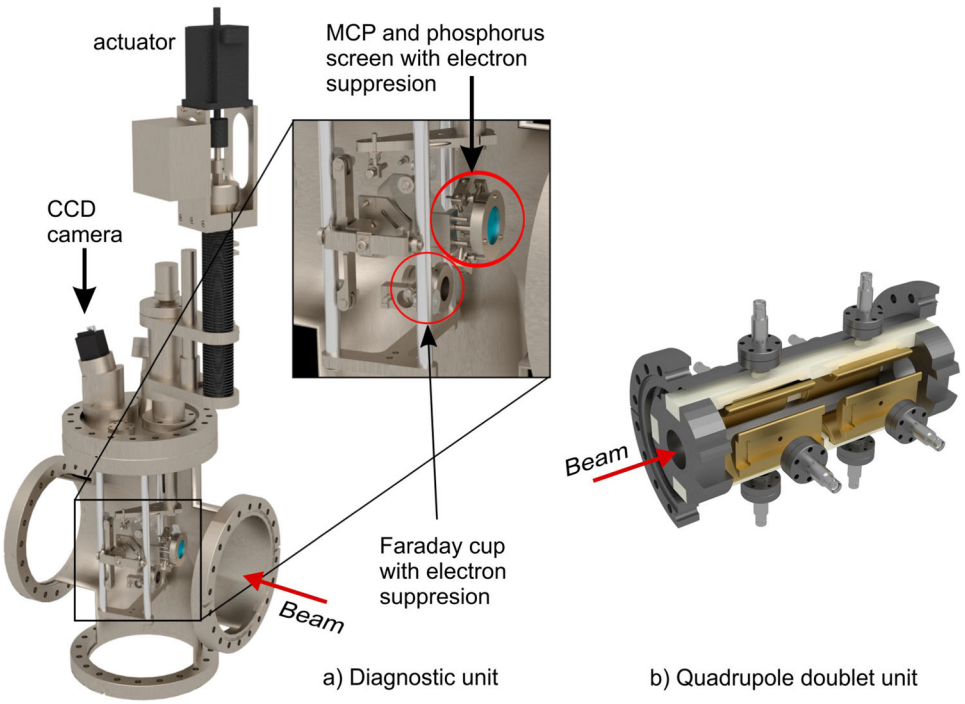

Fig. 41 **a** Overview of a typical diagnostic element consisting of an MCP and a Faraday cup, mounted on an actuator drive. An additional port on the bottom side of the vacuum chamber can be used for mounting a turbomolecular pump. Additional smaller ports can be added sideways for pressure gauges. **b** Overview of a typical quadrupole doublet unit consisting of eight hyperbolic or round electrodes. A minimum of six feedthroughs is needed for additional steering on one of the quadrupoles, or eight in case both are used as shown in figure

an emittance 5 π mm mrad, which corresponds to a conservative estimate for the acceptance of the MATS-LaSpec RFQ cooler and buncher [13], the minimum mass is as small as a few atomic mass units. For bunches of 10^5 ions or less, a doublet separation of 1 m readily fulfills the requirements that space-charge effects are negligible. Therefore, a doublet separation of 1 m has been chosen for the beamline.

A dipole voltage offset can be applied to one or both quadrupoles of each doublet to allow for the steering of the beam. The power supplies for each quadrupole electrode need to be able to deliver 1 kV or more of each polarity with a ripple lower than 20 mV. A possible design of a quadrupole doublet with the corresponding vacuum chamber is shown in Fig. 41.

The beamline is built from DN160 tubes. Three vacuum chambers providing pumping and diagnostics are placed in the beamline. The beamline is evacuated to a pressure of a few 10^{-7} mbar using turbomolecular pumps with a pumping speed of 300 l/s. The diagnostics stations will be placed in the focal plane of each doublet pair. A diagnostic unit contains a position-sensitive micro-channel plate (MCP) detector with a phosphorus screen monitored by a CCD camera as well as a Faraday cup, as shown in Fig. 41. Additional vacuum ports can be used

for vacuum pumps and residual pressure monitors. Both detectors are mounted on a single axis with a motorized drive, which can be remotely controlled to move the diagnostic elements in and out of the beam path. The CSC and the beamline in the MATS-LaSpec experimental hall can be separated from each other using valves included in the beamline behind the pulsed drift tube at the exit of the CSC and in front of the wall of the LEB hall. The same beamline concept is maintained throughout the full length of the beamline, including the part in the MATS-LaSpec hall.

7 Radiation environment and safety issues

The maximum rate foreseen for the LEB hall is 10^7 ions/s for all elements up to uranium. The CSC has been designed for this maximum rate. All electronic supplies and devices of the system are installed below or above the CSC and the beamline. The dose this equipment is subject to will be much less than 1 Gy/year even if longer experiments with maximum rate are performed.

Inside the CSC, different radioactive ion sources will be installed. (i) For calibration of silicon detectors in the RFQ beamline three-line α sources (^{239}Pu, ^{241}Am, ^{244}Cm, ~ 3 kBq) will be used. (ii) For testing the ion transport in the CSC and extraction of ions from the CSC an α recoil ion source (^{228}Th, ~ 20 kBq) will be used. This source allows determination of extraction efficiencies and extraction times with high precision. (iii) A weak ^{252}Cf fission source (~ 40 kBq) will be installed to test the ion extraction over a wide mass range and to investigate and optimize the charge states of different elements extracted from the system.

DC voltages up to 6 kV (positive and negative) but with low current (few mA) will be used. The RF carpet will be operated with voltages (peak-to-peak) up to 200 V and a frequency of 15 MHz. The RFQ beamline will be operated with voltages (peak-to-peak) of up to 2 kV and frequencies of up to 2 MHz. All electronic components and feedthroughs will be shielded, encapsulated, and labeled accordingly. For high voltages, mainly connectors according to SHV will be used.

Some parts of the system are at vacuum, while other parts are at overpressure. All components of the system will be protected against overpressure by safety valves that ensure a safe operation even in case of a power failure. The cryogenic temperatures are achieved by electrical cooling. Thus, no high-pressure lines are required. The minimal temperatures in the system are well above the boiling point of the stopping gases to be used. Therefore, there is no risk of liquefying the stopping gas at a cold point.

For the maintenance of the system, heavy components need to be moved. This will be done with a dedicated lifting table and the crane in the FHF1 focal plane area and the crane in the LEB hall. Both should be operated by trained personnel only.

The safety requirements of FAIR and the European and German safety regulations will be followed for the installation and operation of the system.

8 Cave, infrastructure and installation procedure

The CSC, the detectors, degraders and slits in front of the CSC, and the transfer beamline to MATS and LaSpec will be installed at the final focus FLF6 of the LEB, as shown in Fig. 42. Here, the system will deliver thermalized exotic nuclei to the experiments MATS and LaSpec. To allow for other experimental setups at FLF6, it must be possible to remove the CSC from its location at FLF6. In addition to the installation at the main location at FLF6, the CSC will be operated at the focal plane FHF1 in front of the High-Energy Branch. Here, experiments in Early Science/First Science will be performed until the LEB becomes operational in Science++. Furthermore, reaction studies can be performed with the CSC at FHF1, which require higher beam intensities than possible at FLF6. The assembly, maintenance, and off-line tests of the CSC will be performed in the off-line laboratory (E15.009, "Vorbereitung Stopping Cell") in the Super-FRS supply building (L0321A). It is foreseen that the CSC can be transported on wheels between the off-line laboratory and its positions at FHF1 and in the LEB hall through the shielding labyrinth of the Super-FRS. The CSC has been designed to be compatible with the size restrictions along the transport path (doors, elevators, shielding labyrinth, etc.). The transport in the LEB hall can also be done by crane. To enable this transport, the elevator in the Super-FRS supply building and the crane in the LEB hall need to be able to lift a weight of 5 t.

At its locations at FLF6, at FHF1 and in the off-line laboratory, the CSC has the same infrastructural requirements. The following media and resources are required:

- Electrical power
  - Electrical power: 8× (3 × 16 A, 400 V), 3× (3 × 32 A, 400 V), maximum power 100 kW

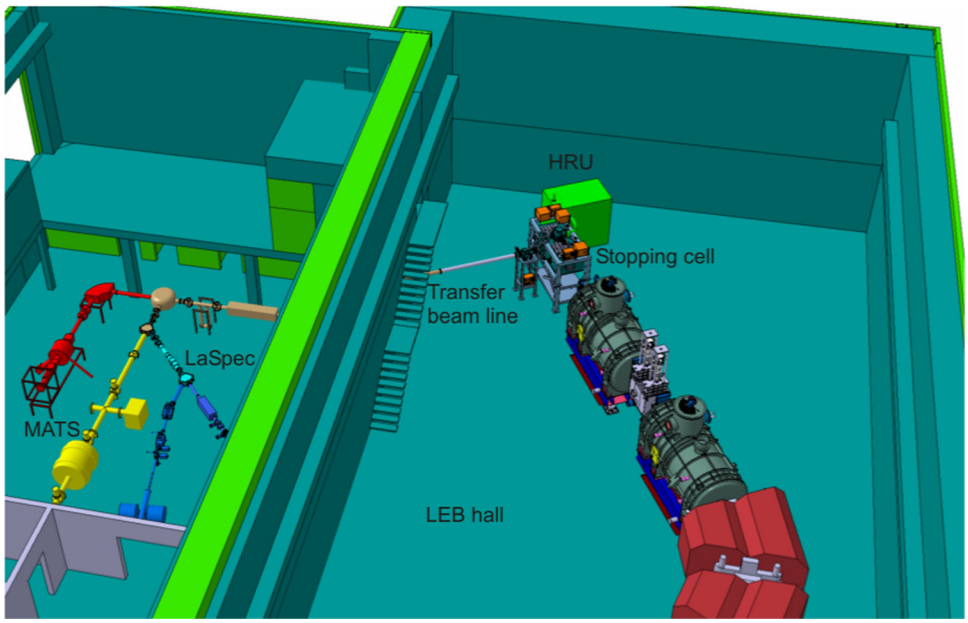

Fig. 42 Section of the LEB hall showing the location of the CSC and the transfer beamline to the MATS-LaSpec hall

  - Clean power and UPS: 1 x (3 × 16 A, 400 V)
- Cooling
  - Cooling water: temperature 18 °C; heat load of 75 kW with temperature difference of 6 °C
  - Heat dissipation into air: 5 kW
- Vacuum exhaust
- Gas lines
  - Pressurized air, dry nitrogen, nitrogen 5.0, helium 6.0, gas for MUSIC (P10 or methane)
  - Three additional gas lines (e.g., for argon, krypton, xenon, oxygen or nitrogen monoxide)
- Network resources
  - EPICS slow control, NUSTAR-DAQ, White Rabbit, about 100 network devices.

For the installation of the detectors, degrader, and slits between the last multiplet and the CSC at FLF6, an installation time of 1 month is required. An installation time of 3 months is foreseen for the first installation of the CSC at the LEB. All major components will be tested before their installation. Therefore, the off-line commissioning of the CSC and its auxiliary equipment at FLF6 can be performed in 3 months. For the commissioning of the CSC, the radioactive ion sources in the CSC (^{228}Th recoil ion source and ^{252}Cf fission source) will be used. The MR-TOF-MS will be mounted directly behind the CSC and aid in the characterization of the CSC in a similar way as it has been done for the commissioning and characterization of the prototype stopping cell (see Sect. 3.2). After commissioning of the CSC, the transfer beamline from the CSC to MATS and LaSpec will be installed and commissioned. For the installation of the beamline a time of 2 months and for the off-line commissioning a time of 3 months are foreseen.

Some maintenance and repairs (e.g., of the RF carpets) cannot be performed in the cave, e.g., because a low-dust environment is required. Such work has to be performed in the off-line laboratory in the Super-FRS supply building. Therefore, the transport from FHF1 or the LEB hall to the off-line laboratory will be a standard procedure, including the operation of the CSC in the laboratory to re-commission the system after repairs and changes.

9 Project organization

The development, construction, testing, installation, and commissioning of the CSC of the Super-FRS will be performed by the FRS Ion Catcher Collaboration—as part of the Super-FRS Experiment Collaboration—also on behalf of LEB infrastructure. The FRS Ion Catcher Collaboration has already developed and commissioned the

prototype stopping cell and performed pioneering experiments with the device at the FRS. The main partners of the collaboration are Justus Liebig University Gießen, GSI, University of Jyväskylä, University of Groningen, ELI-NP/IFIN-HH (Bucharest, Romania) and Tel Aviv University/Soreq Nuclear Research Center (Israel). The FRS Ion Catcher Collaboration is also open for collaboration with further groups and institutions. At yearly meetings, recent activities and future work are discussed in detail. Matters relating to the integration of the stopping cell at FHF1 and in the LEB and the interfaces to the connected experiments are addressed jointly with the involved NUSTAR experiment collaborations MATS, LaSpec, Super-FRS Experiment, and the FAIR project branch at GSI and the respective coordinators.

The same conceptual design of the stopping cell for the Super-FRS, the HADO-CSC, will also be the basis for the development of the stopping cells at ELI-NP [124] and SARAF (Yavne, Israel) [125]. The collaboration with these partners will be further strengthened to exploit maximum synergies. A series of HADO-CSC workshops has been started in 2017 to facilitate an intense information exchange.

Acknowledgements The authors thank D. Blum, K. Dort, and D. Schäfer for their contributions to this work and K.-H. Behr, A. Bergmann, T. Blatz, A. Brünle, C. Karagiannis, A. Kratz, C. Lotze, C. Schlör, F. Schreuder, J. Siebring, B. Szczepanczyk, T. Wasem, and R. Weißfor excellent technical support. The results presented in this paper are based on work performed before February 24, 2022. Financial support was provided within the collaboration agreement between the GSI Helmholtzzentrum für Schwerionenforschung GmbH and KVI-CART/University of Groningen, by Justus-Liebig-Universität Gießen and GSI under the JLU-GSI strategic Helmholtz partnership agreement, by the German Federal Ministry for Education and Research (BMBF) under Contract Nos. 05P12RGFN8, 05P16RGFN1, 05P19RGFN1, 05P21RGFN1, and 05P24RG4, by the Hessian Ministry for Science and Art (HMWK) through the LOEWE Center HICforFAIR, by HGS-HIRe, by EU RTD IONCATCHER under Contract No. HPRI-CT 2001-50022, by EC FP7-Capacities, contract ENSAR No. 262010, by the European Union's Horizon 2020 Research and Innovation Program under Contract No. 654002 via the JRA SATNURSE, and by the FAIR-RO/RD/2024 008 project sponsored by the Romanian Ministry of Research, Innovation and Digitalisation. For the purpose of open access, the author has applied a Creative Commons Attribution (CC BY) license to any Author Accepted Manuscript version arising from this submission. This publication is funded by the Open Access Publishing Fund of GSI Helmholtzzentrum für Schwerionenforschung.

Funding Open Access funding enabled and organized by Projekt DEAL.

Data Availability The data supporting the results of this research are available from the corresponding author on reasonable request.

References

1. H. Geissel, H. Weick, M. Winkler, G. Münzenberg, V. Chichkine, M. Yavor, T. Aumann, K.H. Behr, M. Böhmer, A. Brünle, K. Burkard, J. Benlliure, D. Cortina-Gil, L. Chulkov, A. Dael, J.-E. Ducret, H. Emling, B. Franczak, J. Friese, B. Gastineau, J. Gerl, R. Gernhäuser, M. Hellström, B. Jonson, J. Kojouharova, R. Kulessa, B. Kindler, N. Kurz, B. Lommel, W. Mittig, G. Moritz, C. Mühle, J.A. Nolen, G. Nyman, P. Roussell-Chomaz, C. Scheidenberger, K.-H. Schmidt, G. Schrieder, B.M. Sherrill, H. Simon, K. Sümmerer, N.A. Tahir, V. Vysotsky, H. Wollnik, A.F. Zeller, The Super-FRS project at GSI. Nucl. Instrum. Methods B **204**, 71–85 (2003)
2. J.S. Winfield, H. Geissel, J. Gerl, G. Münzenberg, C. Nociforo, W.R. Plaß, C. Scheidenberger, H. Weick, M. Winkler, M.I. Yavor, A versatile high-resolution magnetic spectrometer for energy compression, reaction studies and nuclear spectroscopy. Nucl. Instrum. Methods A **704**, 76–83 (2013)
3. H. Geissel, J.S. Winfield, G.P.A. Berg, B. Franczak, N. Iwasa, G. Münzenberg, C. Nociforo, W.R. Plaß, C. Scheidenberger, H. Weick, M. Winkler, M. Yavor, Dispersion-matched spectrometer in the low-energy branch of the Super-FRS for high-resolution measurements with large-emittance relativistic fragment beams. Nucl. Instrum. Methods B **317**, 277–283 (2013)
4. T. Dickel, W.R. Plaß, A. Becker, U. Czok, H. Geissel, E. Haettner, C. Jesch, W. Kinsel, M. Petrick, C. Scheidenberger, M.I. Yavor, A high-performance multiple-reflection time-of-flight mass spectrometer and isobar separator for the research with exotic nuclei. Nucl. Instrum. Methods A **777**, 172–188 (2015)

5. I. Miskun, T. Dickel, I. Mardor, C. Hornung, D. Amanbayev, S. Ayet San Andrés, J. Bergmann, J. Ebert, H. Geissel, M. Górska, F. Greiner, E. Haettner, W.R. Plaß, S. Purushothaman, C. Scheidenberger, A.-K. Rink, H. Weick, S. Bagchi, P. Constantin, S. Kaur, W. Lippert, B. Mei, I. Moore, J.-H. Otto, S. Pietri, I. Pohjalainen, A. Prochazka, C. Rappold, M.P. Reiter, Y.K. Tanaka, J.S. Winfield, A novel method for the measurement of half-lives and decay branching ratios of exotic nuclei. Eur. Phys. J. A **55**(9), 148 (2019)
6. G. Münzenberg, H. Geissel, S. Heinz, C. Scheidenberger, H.M. Devaraja, S. Hofmann, M. Winkler, J.S. Winfield, W.R. Plaß, M. Gupta, SHE research on the way to NUSTAR and FAIR. Proceedings of the International Symposium on Exotic Nuclei, pp. 541–550 (2015)
7. T. Dickel, A. Kankainen, A. Spataru, D. Amanbayev, O. Beliuskina, S. Beck, P. Constantin, D. Benyamin, H. Geissel, L. Gröf, C. Hornung, A.V. Karpov, I. Mardor, G. Münzenberg, D. Nichita, W.R. Plaß, I. Pohjalainen, S. Purushothaman, M. Reponen, A. Rotaru, V.V. Saiko, C. Scheidenberger, J.S. Winfield, A. Zadvornaya, Multi-nucleon transfer reactions at ion catcher facilities: a new way to produce and study heavy neutron-rich nuclei. J. Phys.: Conf. Ser. **1668**, 012012 (2020)
8. A. Mollaebrahimi, P. Constantin, T. Dickel, D. Amanbayev, S. Glöckner, E. Haettner, D. Kar, G. Kripko-Koncz, D. Kumar, K. Mahajan, I. Mardor, D. Morrissey, M. Narang, W.R. Plaß, A. Shrayer, N. Tortorelli, J. Yu, J. Ahokas, B. Amorim, Ayet San Andrés, S., Bagchi, S., Bajzek, M., Balabanski, D., Bergmann, J., Botsiou, K., Charviakova, V., Eronen, T., Ge, Z., Harakeh, M., Hornung, C., Hubbard, N., Jaries, A., Kalantar-Nayestanaki, N., Kankainen, A., Karmakar, A., Lozeva, R., Rodriguez Sanchez, J.L., Mitsiou, I., Reiter, M.P., Piau, V., Podolyak, Z., Prajapat, R., Prajapati, D., Purushothaman, S., Reponen, M., Rocco, E., Ruotsalainen, J., Scheidenberger, C., Simonov, M., Kostyleva, D., Singh, S.K., Spataru, A., State, A., Stefanescu, I., Tanaka, Y.K., Trache, L., Welde, L., Zhao, J., First observation of MNT isotope beams at the FRS Ion Catcher. Nucl. Phys. A **1057**, 123041 (2025)
9. J. Äystö, K.-H. Behr, J. Benlliure, A. Bracco, P. Egelhof, A. Fomichev, S. Gales, H. Geissel, T. Grahn, L.V. Grigorenko, M.N. Harakeh, R. Hayano, S. Heinz, K. Itahashi, A. Jokinen, N. Kalantar-Nayestanaki, R. Kanungo, H. Lenske, I. Mukha, G. Münzenberg, C. Nociforo, H.J. Ong, S. Pietri, M. Pfützner, W. Plaß, A. Prochazka, S. Purushothaman, T. Saito, C. Scheidenberger, H. Simon, I. Tanihata, S. Terashima, H. Toki, L. Trache, H. Weick, J.S. Winfield, M. Winkler, V. Zamfir, Experimental program of the Super-FRS Collaboration at FAIR and developments of related instrumentation. Nucl. Instrum. Methods B **376**, 111–115 (2016)
10. C. Hornung, T. Dickel, D. Amanbayev, Ayet San Andrés, S., Balabanski, D.L., Beck, S., Bergmann, J., Constantin, P., Ebert, J., Geissel, H., Greiner, F., Gröf, L., Haettner, E., Harakeh, M.N., Hucka, J.-P., Kalantar-Nayestanaki, N., Kostyleva, D.A., Kripko-Koncz, G., Miskun, I., Mollaebrahimi, A., Mukha, I., Münzenberg, G., Pietri, S., Plaß, W.R., Purushotaman, S., Reiter, M.P., Rink, A.-K., Roesch, H., Scheidenberger, C., Spataru, A., Tanaka, Y.K., Weick, H., Zhao, J., Mass tagging: verification and calibration of particle identification by high-resolution mass measurements. Nucl. Instrum. Methods B **541**, 257–259 (2023)
11. T. Dickel, W.R. Plaß, H. Geissel, F. Heiße, I. Miskun, S. Purushothaman, M.P. Reiter, A.-K. Rink, C. Scheidenberger, Conceptional design of a novel next-generation cryogenic stopping cell for the Low-Energy Branch of the Super-FRS. Nucl. Instrum. Methods B **376**, 216–220 (2016)
12. A. Spataru, C. Hornung, T. Dickel, E. Haettner, S. Pietri, Ayet San Andrés, S., Bagchi, S., Balabanski, D.L., Bergmann, J., Ebert, J., Finley, A., Geissel, H., Greiner, F., Hall, O., Kaur, S., Lippert, W., Miskun, I., Otto, J.-H., Plaß, W.R., Prochazka, A., Purushothaman, S., Rappold, C., Rink, A.-K., Scheidenberger, C., Tanaka, Y.K., Toernqvist, H., Weick, H., Winfield, J.S., First coupling of the FRS particle identification and the FRS-Ion Catcher data acquisition systems: the case of ^{109}In. Nucl. Instrum. Methods B **522**, 32–37 (2022)
13. D. Rodriguez et al., MATS and LaSpec: High-precision experiments using ion traps and lasers at FAIR. Eur. Phys. J. Spec. Top. **183**, 1–123 (2010)
14. D. Rodriguez, The advanced trapping facility MATS at FAIR. Int. J. Mass Spectrom. **349–350**, 255–263 (2013)
15. W. Nörtershäuser, P. Campbell, LaSpec at FAIR's low energy beam line: a new perspective for laser spectroscopy of radioactive nuclei. Hyperfine Interact. **171**, 149–156 (2006)
16. H. Geissel, T. Schwab, P. Armbruster, J.P. Dufour, E. Hanelt, K.-H. Schmidt, B. Scherrill, G. Münzenberg, Ions penetrating through ion-optical systems and matter - non-Liouvillian phase-space modelling. Nucl. Instrum. Methods A **282**, 247–260 (1989)
17. H. Weick, H. Geissel, C. Scheidenberger, F. Attallah, T. Baumann, D. Cortina, M. Hausmann, B. Lommel, G. Münzenberg, N. Nankov, F. Nickel, T. Radon, H. Schatz, K. Schmidt, J. Stadlmann, K. Sümmerer, M. Winkler, H. Wollnik, Slowing down of relativistic few-electron heavy ions. Nucl. Instrum. Methods B **164–165**, 168–179 (2000)
18. C. Scheidenberger, H. Geissel, M. Maier, G. Münzenberg, M. Portillo, G. Savard, P.V. Duppen, H. Weick, M. Winkler, M. Yavor, F. Attallah, K.-H. Behr, V. Chichkine, S. Eliseev, M. Hausmann, M. Hellström, E. Kaza, B. Kindler, Y. Litvinov, B. Lommel, G. Marx, M. Matos, N. Nankov, T. Ohtsubo, K. Sümmerer, Z.-Y. Sun, Z. Zhou, Energy and range focusing of in-flight separated exotic nuclei: a study for the energy-buncher stage of the low-energy branch of the Super-FRS. Nucl. Instrum. Methods B **204**, 119–123 (2003)
19. M. Wada, Genealogy of gas cells for low-energy RI-beam production. Nucl. Instrum. Methods B **317**, 450–456 (2013)
20. J. Ärje, K. Valli, Helium-jet ion guide for an on-line isotope separator. Nucl. Instrum. Methods **179**, 535–539 (1981)
21. J. Ärje, J. Äysto, H. Hyvönen, P. Taskinen, V. Koponen, J. Honkanen, A. Hautojärvi, K. Vierinen, Submillisecond on-line mass separation of nonvolatile radioactive elements: an application of charge exchange and thermalization processes of primary recoil ions in helium. Phys. Rev. Lett. **54**, 99–101 (1985)

22. M. Wada, Y. Ishida, T. Nakamura, Y. Yamazaki, T. Kambara, H. Ohyama, Y. Kanai, T.M. Kojima, Y. Nakai, N. Ohshima, A. Yoshida, T. Kubo, Y. Matsuo, Y. Fukuyama, K. Okada, T. Sonoda, S. Ohtani, K. Noda, H. Kawakami, I. Katayama, Slow RI-beams from projectile fragment separators. Nucl. Instrum. Methods B **204**, 570–581 (2003)
23. G. Savard, J. Clark, C. Boudreau, F. Buchinger, J.E. Crawford, H. Geissel, J.P. Greene, S. Gulick, A. Heinz, J.K.P. Lee, A. Levand, M. Maier, G. Münzenberg, C. Scheidenberger, D. Seweryniak, K.S. Sharma, G. Sprouse, J. Vaz, J.C. Wang, B.J. Zabransky, Z. Zhou, Development and operation of gas catchers to thermalize fusion-evaporation and fragmentation products. Nucl. Instrum. Methods B **204**, 582–586 (2003)
24. K. Cooper, C.S. Sumithrarachchi, D.J. Morrissey, A. Levand, J.A. Rodriguez, G. Savard, S. Schwarz, B. Zabransky, Extraction of thermalized projectile fragments from a large volume gas cell. Nucl. Instrum. Methods A **763**, 543–546 (2014)
25. L. Weissman, D.J. Morrissey, G. Bollen, D.A. Davies, E. Kwan, P.A. Lofy, P. Schury, S. Schwarz, C. Sumithrarachchi, T. Sun, R. Ringle, Conversion of 92 MeV/u ^{38}Ca/^{37}K projectile fragments into thermalized ion beams. Nucl. Instrum. Methods A **540**, 245–258 (2005)
26. K. Lund, G. Bollen, D. Lawton, D. Morrissey, J. Ottarson, R. Ringle, S. Schwarz, C. Sumithrarachchi, A. Villari, J. Yurkon, Online tests of the advanced cryogenic gas stopper at NSCL. Nucl. Instrum. Methods B **463**, 378–381 (2020)
27. J.B. Neumayr, L. Beck, D. Habs, S. Heinz, J. Szerypo, P.G. Thirolf, V. Varentsov, F. Voit, D. Ackermann, D. Beck, M. Block, Z. Di, S.A. Eliseev, H. Geissel, F. Herfurth, F.P. Heßberger, S. Hofmann, H.-J. Kluge, M. Mukherjee, G. Münzenberg, M. Petrick, W. Quint, S. Rahaman, C. Rauth, D. Rodriguez, C. Scheidenberger, G. Sikler, Z. Wang, C. Weber, W.R. Plaß, M. Breitenfeldt, A. Chaudhuri, G. Marx, L. Schweikhard, A.F. Dodonov, Y. Novikov, M. Suhonen, The ion-catcher device for SHIPTRAP. Nucl. Instrum. Methods B **244**, 489–500 (2006)
28. C. Droese, S. Eliseev, K. Blaum, M. Block, F. Herfurth, M. Laatiaoui, F. Lautenschläger, E.M. Ramirez, L. Schweikhard, V.V. Simon, P.G. Thirolf, The cryogenic gas stopping cell of SHIPTRAP. Nucl. Instrum. Methods B **338**, 126–138 (2014)
29. J.B. Neumayr, P.G. Thirolf, D. Habs, S. Heinz, V.S. Kolhinen, M. Sewtz, J. Szerypo, Performance of the MLL-IonCatcher. Rev. Sci. Instrum. **77**, 065109 (2006)
30. G. Savard, S. Baker, C. Davids, A.F. Levand, E.F. Moore, R.C. Pardo, R. Vondrasek, B.J. Zabransky, G. Zinkann, Radioactive beams from gas catchers: the CARIBU facility. Nucl. Instrum. Methods B **266**, 4086–4091 (2008)
31. L. Wense, P.G. Thirolf, D. Kalb, M. Laatiaoui, Towards a direct transition energy measurement of the lowest nuclear excitation in ^{229}Th. J. Instrum. **8**(3), 03005 (2013)
32. A. Takamine, M. Wada, K. Okada, T. Sonoda, P. Schury, T. Nakamura, Y. Kanai, T. Kubo, I. Katayama, S. Ohtani, H. Wollnik, H.A. Schuessler, Hyperfine structure constant of the neutron halo nucleus ^{11}Be^{+}. Phys. Rev. Lett. **112**, 162502 (2014)
33. J. Savory, P. Schury, C. Bachelet, M. Block, G. Bollen, M. Facina, C.M. Folden III., C. Guenaut, E. Kwan, A.A. Kwiatkowski, D.J. Morrissey, G.K. Pang, A. Prinke, R. Ringle, H. Schatz, S. Schwarz, C.S. Sumithrarachchi, rp process and masses of N $\approx$ Z $\approx$ 34 nuclides. Phys. Rev. Lett **102**, 132501 (2009)
34. A. Hamaker, E. Leistenschneider, R. Jain, G. Bollen, S. Giuliani, K. Lund, W. Nazarewicz, L. Neufcourt, C. Nicoloff, D. Puentes et al., Precision mass measurement of lightweight self-conjugate nucleus ^{80}Zr. Nat. Phys. **17**(12), 1408–1412 (2021)
35. C. Rauth, D. Ackermann, K. Blaum, M. Block, A. Chaudhuri, Z. Di, S. Eliseev, R. Ferrer, D. Habs, F. Herfurth, F.P. Heßberger, S. Hofmann, H.-J. Kluge, G. Maero, A. Martin, G. Marx, M. Mukherjee, J.B. Neumayr, W.R. Plaß, S. Rahaman, D. Rodriguez, C. Scheidenberger, L. Schweikhard, P.G. Thirolf, G. Vorobjev, C. Weber, First Penning trap mass measurements beyond the proton drip line. Phys. Rev. Lett. **100**, 012501 (2008)
36. M. Block, D. Ackermann, K. Blaum, C. Droese, M. Dworschak, S. Eliseev, T. Fleckenstein, E. Haettner, F. Herfurth, F.P. Heßberger, S. Hofmann, J. Ketelaer, J. Ketter, H.-J. Kluge, G. Marx, M. Mazzocco, Y.N. Novikov, W.R. Plaß, A. Popeko, S. Rahaman, D. Rodriguez, C. Scheidenberger, L. Schweikhard, P.G. Thirolf, G.K. Vorobjev, C. Weber, Direct mass measurements above uranium bridge the gap to the island of stability. Nature **463**, 785–788 (2010)
37. Y. Ito, P. Schury, M. Wada, F. Arai, H. Haba, Y. Hirayama, S. Ishizawa, D. Kaji, S. Kimura, H. Koura, M. MacCormick, H. Miyatake, J.Y. Moon, K. Morimoto, K. Morita, M. Mukai, I. Murray, T. Niwase, K. Okada, A. Ozawa, M. Rosenbusch, A. Takamine, T. Tanaka, Y.X. Watanabe, H. Wollnik, S. Yamaki, First direct mass measurements of nuclides around $Z = 100$ with a multireflection time-of-flight mass spectrograph. Phys. Rev. Lett. **120**, 152501 (2018)
38. D.L. Lincoln, J.D. Holt, G. Bollen, M. Brodeur, S. Bustabad, J. Engel, S.J. Novario, M. Redshaw, R. Ringle, S. Schwarz, First direct double-β decay Q-value measurement of ^{82}Se in support of understanding the nature of the neutrino. Phys. Rev. Lett **110**, 012501 (2013)
39. M.G. Sternberg, R. Segel, N.D. Scielzo, G. Savard, J.A. Clark, P.F. Bertone, F. Buchinger, M. Burkey, S. Caldwell, A. Chaudhuri, J.E. Crawford, C.M. Deibel, J. Greene, S. Gulick, D. Lascar, A.F. Levand, G. Li, A.P. Galvan, K.S. Sharma, J.V. Schelt, R.M. Yee, B.J. Zabransky, Limit on tensor currents from ^{8}Li β decay. Phys. Rev. Lett **115**, 182501 (2015)
40. L. Wense, B. Seiferle, M. Laatiaoui, J.B. Neumayr, H.-J. Maier, H.-F. Wirth, C. Mokry, J. Runke, K. Eberhardt, C.E. Duellmann, N.G. Trautmann, P.G. Thirolf, Direct detection of the ^{229} Th nuclear clock transition. Nature **533**(7601), 47–51 (2016)
41. H. Geissel, P. Armbruster, K.H. Behr, A. Brünle, K. Burkard, M. Chen, H. Folger, B. Franczak, H. Keller, O. Klepper, B. Langenbeck, F. Nickel, E. Pfeng, M. Pfützner, E. Roeckl, K. Rykaczewski, I. Schall, D. Schardt, C. Scheidenberger, K.-H. Schmidt, A. Schröter, T. Schwab, K. Sümmerer, M. Weber, G. Münzenberg, T. Brohm, H.-G. Clerc, M. Fauerbach,

J.-J. Gaimard, A. Grewe, E. Hanelt, B. Knödler, M. Steiner, B. Voss, J. Weckenmann, C. Ziegler, A. Magel, H. Wollnik, J.P. Dufour, Y. Fujita, D.J. Vieira, B. Sherrill, The GSI projectile fragment separator (FRS): a versatile magnetic system for relativistic heavy ions. Nucl. Instrum. Methods B **70**, 286–297 (1992)
42. M. Petrick, W.R. Plaß, K.-H. Behr, A. Brünle, L. Caceres, J. Clark, Z. Di, S. Elisseev, M. Facina, A. Fettouhi, H. Geissel, W. Hüller, M. Huyse, C. Karagiannis, B. Kindler, R. Knöbel, Y. Kudryavtsev, J. Kurcewicz, T. Levant, Y.A. Litvinov, B. Lommel, M. Maier, D.J. Morrissey, G. Münzenberg, M. Portillo, G. Savard, C. Scheidenberger, P.V. Duppen, H. Weick, M. Winkler, B. Zabransky, Online test of the FRS Ion Catcher at GSI. Nucl. Instrum. Methods B **266**, 4493–4497 (2008)
43. M. Ranjan, S. Purushothaman, T. Dickel, H. Geissel, W.R. Plaß, D. Schäfer, C. Scheidenberger, J. Van de Walle, H. Weick, P. Dendooven, New stopping cell capabilities: RF carpet performance at high gas density and cryogenic operation. Eur. Phys. Lett. **96**, 52001 (2011)
44. M. Ranjan, Design and characterization of a cryogenic stopping cell for radioactive ions. PhD thesis, KVI, University of Groningen (2012)
45. S. Purushothaman, M.P. Reiter, E. Haettner, P. Dendooven, T. Dickel, H. Geissel, J. Ebert, C. Jesch, W.R. Plaß, M. Ranjan, H. Weick, F. Amjad, S. Ayet, M. Diwisch, A. Estrade, F. Farinon, F. Greiner, N. Kalantar-Nayestanaki, R. Knöbel, J. Kurcewicz, J. Lang, I. Moore, I. Mukha, C. Nociforo, M. Petrick, M. Pfuetzner, S. Pietri, A. Prochazka, A.-K. Rink, S. Rinta-Antila, C. Scheidenberger, M. Takechi, Y.K. Tanaka, J.S. Winfield, M.I. Yavor, First online results of a cryogenic stopping cell with short-lived heavy uranium fragments produced at 1000 MeV/u. Eur. Phys. Lett. **104**, 42001 (2013)
46. M. Ranjan, P. Dendooven, S. Purushothama, T. Dickel, M.P. Reiter, S. Ayet, E. Haettner, I.D. Moore, N. Kalantar-Nayestanaki, H. Geissel, W.R. Plaß, D. Schäfer, C. Scheidenberger, F. Schreuder, H. Timersma, J. Van de Walle, H. Weick, Design, construction and cooling system performance of a prototype cryogenic stopping cell for the Super-FRS at FAIR. Nucl. Instrum. Methods A **770**, 87–97 (2015)
47. M.P. Reiter, Pilot experiments with relativistic uranium projectile and fission fragments thermalized in a cryogenic gas-filled stopping cell. PhD thesis, Justus Liebig University Gießen (2015)
48. W.R. Plaß, T. Dickel, S. Purushothaman, P. Dendooven, H. Geissel, J. Ebert, E. Haettner, C. Jesch, M. Ranjan, M.P. Reiter, H. Weick, F. Amjad, S. Ayet, M. Diwisch, A. Estrade, F. Farinon, F. Greiner, N. Kalantar-Nayestanaki, R. Knöbel, J. Kurcewicz, J. Lang, I. Moore, I. Mukha, C. Nociforo, M. Petrick, M. Pfuetzner, S. Pietri, A. Prochazka, A.-K. Rink, S. Rinta-Antila, D. Schäfer, C. Scheidenberger, M. Takechi, Y.K. Tanaka, J.S. Winfield, M.I. Yavor, The FRS Ion Catcher: a facility for high-precision experiments with stopped projectile and fission fragments. Nucl. Instrum. Methods B **317**, 457–462 (2013)
49. T. Dickel, W.R. Plaß, Ayet San Andrés, S., Ebert, J., Geissel, H., Haettner, E., Hornung, C., Miskun, I., Pietri, S., Purushothaman, S., Reiter, M.P., Rink, A.K., Scheidenberger, C., Weick, H., Dendooven, P., Diwisch, M., Greiner, F., Heiße, F., Knöbel, R., Lippert, W., Moore, I.D., Pohjalainen, I., Prochazka, A., Ranjan, M., Takechi, M., Winfield, J.S., Xu, X., First spatial separation of a heavy ion isomeric beam with a multiple-reflection time-of-flight mass spectrometer. Phys. Lett. B **744**, 137–141 (2015)
50. M.P. Reiter, A.-K. Rink, T. Dickel, E. Haettner, F. Heiße, W.R. Plaß, S. Purushothaman, F. Amjad, Ayet San Andrés, S., Bergmann, J., Blum, D., Dendooven, P., Diwisch, M., Ebert, J., Geissel, H., Greiner, F., Hornung, C., Jesch, C., Kalantar-Nayestanaki, N., Knöbel, R., Lang, J., Lippert, W., Miskun, I., Moore, I.D., Nociforo, C., Petrick, M., Pietri, S., Pfützner, M., Pohjalainen, I., Prochazka, A., Scheidenberger, C., Takechi, M., Tanaka, Y.K., Weick, H., Winfield, J.S., Xu, X., Rate capability of a cryogenic stopping cell for uranium projectile fragments produced at 1000 MeV/u. Nucl. Instrum. Methods B **376**, 240–245 (2016)
51. A.-K. Rink, Mass and Life-Time Measurement of the 1.7 ms ^{215}Po Isotope: a crucial Test of the Novel Concept of the Cryogenic Ion Catcher for the Super FRS at GSI-FAIR. PhD thesis, Justus Liebig University Gießen (2017)
52. Ayet San Andrés, S., Hornung, C., Ebert, J., Plaß, W.R., Dickel, T., Geissel, H., Scheidenberger, C., Bergmann, J., Greiner, F., Haettner, E., Jesch, C., Lippert, W., Mardor, I., Miskun, I., Patyk, Z., Pietri, S., Pihktelev, A., Purushothaman, S., Reiter, M.P., Rink, A.-K., Weick, H., Yavor, M.I., Bagchi, S., Charviakova, V., Constantin, P., Diwisch, M., Finlay, A., Kaur, S., Knöbel, R., Lang, J., Mei, B., Moore, I.D., Otto, J.-H., Pohjalainen, I., Prochazka, A., Rappold, C., Takechi, M., Tanaka, Y.K., Winfield, J.S., Xu, X., High-resolution, accurate multiple-reflection time-of-flight mass spectrometry for short-lived, exotic nuclei of a few events in their ground and low-lying isomeric states. Phys. Rev. C **99**, 064313 (2019)
53. W.R. Plaß, T. Dickel, I. Mardor, S. Pietri, H. Geissel, C. Scheidenberger, D. Amanbayev, Ayet San Andrés, S., Äystö, J., Balabanski, D.L., Beck, S., Bergmann, J., Charviakova, V., Constantin, P., Eronen, T., Grahn, T., Greiner, F., Haettner, E., Hornung, C., Hucka, J.P., Jokinen, A., Kankainen, A., Miskun, I., Moore, I.D., Pikthtelev, A., Pohjalainen, I., Purushothman, S., Patyk, Z., Reiter, M.P., Rink, A.-K., Rinta-Antila, S., Spataru, A., Weick, H., Winfield, J.S., Yavor, M.I., The science case of the FRS Ion Catcher for FAIR Phase-0. Hyperfine Interact. **240**, 73 (2019)
54. F. Greiner, T. Dickel, S. Ayet San Andrés, J. Bergmann, P. Constantin, J. Ebert, H. Geissel, E. Haettner, C. Hornung, I. Miskun, W. Lippert, I. Mardor, I. Moore, W.R. Plaß, S. Purushothaman, A.-K. Rink, M.P. Reiter, C. Scheidenberger, H. Weick, Removal of molecular contamination in low-energy RIBs by the isolation-dissociation-isolation method. Nucl. Instrum. Methods B **463**, 324–326 (2020)
55. C. Hornung, D. Amanbayev, I. Dedes, G. Kripko-Koncz, I. Miskun, N. Shimizu, Ayet San Andrés, S., Bergmann, J., Dickel, T., Dudek, J., Ebert, J., Geissel, H., Gorska, M., Grawe, H., Greiner, F., Haettner, E., Otsuka, T., Plaß, W.R., Purushothaman, S., Rink, A.-K., Scheidenberger, C., Weick, H., Bagchi, S., Blazhev, A., Charviakova, O., Curien, D.,

Finlay, A., Kaur, S., Lippert, W., Otto, J.-H., Patyk, Z., Pietri, S., Tanaka, Y.K., Tsunoda, Y., Winfield, J.S., Isomer studies in the vicinity of the doubly-magic nucleus ^{100} Sn : observation of a new low-lying isomeric state in ^{97}Ag. Phys. Lett. B **802**, 135200 (2020)
56. S. Ayet San Andrés, A. Mollaebrahimi, T. Dickel, J. Bergmann, J. Ebert, H. Geissel, F. Greiner, E. Haettner, C. Hornung, N. Kalantar-Nayestanaki, I. Miskun, W.R. Plass, S. Purushothaman, A.K. Rink, C. Scheidenberger, H. Weick, S. Bagchi, P. Constantin, A. Finlay, S. Kaur, W. Lippert, I. Mardor, B. Mei, I. Moore, J.H. Otto, S. Pietri, I. Pohjalainen, A. Prochazka, C. Rappold, M.P. Reiter, Y.K. Tanaka, J.S. Winfield, Mass and half-life measurements of neutron-deficient iodine isotopes. Eur. Phys J. A **56**, 5 (2020)
57. N. Tortorelli, M.P. Reiter, A.K. Rink, S. Purushothaman, S. Ayet-San-Andrés, J. Bergmann, T. Dickel, M. Diwisch, J. Ebert, H. Geissel et al., Alpha spectroscopy of purified beams of exotic nuclei at the FRS Ion Catcher. Nuclear Phys. A **1053**, 122967 (2025)
58. I. Mardor, T. Dickel, D. Amanbayev, Ayet San Andrés, S., Beck, S., Benyamin, D., Bergmann, J., Constantin, P., Cuillerier, A.C., Geissel, H., Gröf, L., Hornung, C., Kripko-Koncz, G., Mollaebrahimi, A., Miskun, I., Plaß, W.R., Pomp, S., Rotaru, A., Scheidenberger, C., Stanic, G., Will, C., Determining spontaneous fission properties by direct mass measurements with the FRS Ion Catcher. EPJ Web Conf. **239**, 02004 (2020)
59. A. Spataru, D. Amanbayev, S. Ayet San Andrés, D. Balabanski, S. Beck, J. Bergmann, P. Constantin, T. Dickel, H. Geissel, C. Hornung et al., Nuclear structure studies with high-precision mass measurements of spontaneous fission fragments at the FRS Ion Catcher. Bulg. J. Phys **48**, 535–540 (2021)
60. Y. Waschitz, D. Amanbayev, A. Spataru, I. Mardor, T. Dickel, E.O. Cohen, O. Aviv, S. Ayet-San-Andrés, D.L. Balabanski, S. Beck, J. Bergmann, Z. Brencic, P. Constantin, M. Dehghan, H. Geissel, L. Gröf, C. Hornung, N. Kalantar-Nayestanaki, G. Kripko-Koncz, I. Miskun, A. Mollaebrahimi, D. Nichita, W.R. Plaß, S. Pomp, C. Scheidenberger, A. Solders, G. Stanic, M. Wasserheß, M. Vencelj, J. Zhao, Independent isotopic fission yields of ^{252}Cf spontaneous fission via mass measurements at the FRS Ion Catcher. EPJ Web Conf. **284**, 04005 (2023)
61. A. Spataru, G. Kripko-Koncz, D. Amanbayev, S. Ayet San Andrés, D.L. Balabanski, S. Beck, J. Bergmann, P. Constantin, T. Dickel, H. Geissel, C. Hornung, N. Kalantar-Nayestanaki, I. Mardor, N. Minkov, A. Mollaebrahimi, W.R. Plaß, C. Scheidenberger, M. Wasserheß, J. Zhao, Studying shape phase transition in even-proton nuclei via mass measurements. Phys. Scr. **99**, 075305 (2024)
62. L. Varga, H. Wilsenach, O. Hall, T. Dickel, M. Reiter, D. Amanbayev, T. Davinson, D. Morrissey, I. Pohjalainen, N. Tortorelli et al., Novel device to study double-alpha decay at the FRS Ion Catcher. Nucl. Instrum. Methods A **1063**, 169252 (2024)
63. I. Mardor, S. Ayet-San-Andrés, T. Dickel, D. Amanbayev, S. Beck, J. Bergmann, H. Geissel, L. Gröf, E. Haettner, C. Hornung, N. Kalantar-Nayestanaki, G. Kripko-Koncz, I. Miskun, A. Mollaebrahimi, W.R. Plaß, C. Scheidenberger, H. Weick, S. Bagchi, D.L. Balabanski, A.A. Bezbakh, Z. Brencic, O. Charviakova, V. Chudoba, P. Constantin, M. Dehghan, A.S. Fomichev, L.V. Grigorenko, O. Hall, M.N. Harakeh, J.-P. Hucka, A. Kankainen, O. Kiselev, R. Knöbel, D.A. Kostyleva, S.A. Krupko, N. Kurkova, N. Kuzminchuk, I. Mukha, I.A. Muzalevskii, D. Nichita, C. Nociforo, Z. Patyk, M. Pfützner, S. Pietri, S. Purushothaman, M.P. Reiter, H. Roesch, F. Schirru, P.G. Sharov, A. Spataru, G. Stanic, A. State, Y.K. Tanaka, M. Vencelj, M.I. Yavor, J. Zhao, Mass measurements of As, Se, and Br nuclei, and their implication on the proton-neutron interaction strength toward the $N = Z$ line. Phys. Rev. C **103**, 034319 (2021)
64. A. Mollaebrahimi, C. Hornung, T. Dickel, D. Amanbayev, G. Kripko-Koncz, W.R. Plaß, S. Ayet-San-Andrés, S. Beck, A. Blazhev, J. Bergmann et al., Studying Gamow–Teller transitions and the assignment of isomeric and ground states at N = 50. Phys. Lett. B **839**, 137833 (2023)
65. T. Dickel, C. Hornung, D. Amanbayev, S. Ayet-San-Andrés, S. Beck, J. Bergmann, H. Geissel, J. Gerl, M. Gorska, L. Gröf, E. Haettner, J.-P. Hucka, D.A. Kostyleva, G. Kripko-Koncz, A. Mollaebrahimi, I. Mukha, S. Pietri, W.R. Plaß, Z. Podolyak, S. Purushothaman, M.P. Reiter, H. Roesch, C. Scheidenberger, Y.K. Tanaka, H. Weick, J. Zhao, Mean range bunching of exotic nuclei produced by in-flight fragmentation and fission - stopped-beam experiments with increased efficiency. Nucl. Instrum. Methods B **541**, 275–278 (2023)
66. G. Bollen, D.J. Morrissey, S. Schwarz, A study of gas stopping of intense energetic rare isotope beams. Nucl. Instrum. Methods A **550**, 27–38 (2005)
67. S. Schwarz, C. Sumithrarachchi, G. Bollen, C. Magsig, D. Morrissey, J. Ottarson, A. Villari, The cyclotron gas stopper at FRIB getting ready for operations. Nucl. Instrum. Methods B **541**, 109–113 (2023)
68. L. Vermeeren, N. Bijnens, M. Huyse, Y.A. Kudryavtsev, P. Van Duppen, J. Wauters, Z. Qamhieh, P. Thoen, E. Vandeweert, R. Silverans, An on-line laser ion source based on resonance photoionization in a gas cell. Phys. Rev. Lett. **73**(14), 1935 (1994)
69. M. Facina, B. Bruyneel, S. Dean, J. Gentens, M. Huyse, Y. Kudryavtsev, P. Van den Bergh, P. Van Duppen, A gas cell for thermalizing, storing and transporting radioactive ions and atoms: part II—on-line studies with a laser ion source. Nucl. Instrum. Methods B **226**, 401–418 (2004)
70. T. Dickel, W.R. Plaß, P. Reiter, H. Geissel, C. Scheidenberger, Conceptual design of a next-generation cryogenic stopping cell for the Low-Energy Branch of the Super-FRS. GSI Sci. Rep. **2013**, 106 (2014)
71. N. Iwasa, H. Geissel, G. Münzenberg, C. Scheidenberger, T. Schwab, H. Wollnik, MOCADI, a universal Monte Carlo code for the transport of heavy ions through matter within ion-optical systems. Nucl. Instrum. Methods B **126**, 284–289 (1997)
72. S. Purushothaman, T. Dickel, S. Ayet, S. Bagchi, K.-H. Behr, J. Bergmann, T. Blatz, P. Constantin, J. Ebert, A. Finley, H. Geissel, F. Greiner, E. Haettner, C. Hornung, S. Kaur, W. Lippert, B. Lommel, I. Mardor, B. Mei, I. Miskun, I.

Moore, J.-H. Otto, S. Pietri, A. Pikhtelev, W.R. Plaß, I. Pohjalainen, A. Prochazka, C. Rappold, M.P. Reiter, A.-K. Rink, C. Scheidenberger, B. Szczepanczyk, Y. Tanaka, H. Weick, J.S. Winfield, A gas degrader for the low-energy branch of the Super-FRS at FAIR. GSI Sci. Rep. **2016**, 180 (2017)
73. E. Haettner, W.R. Plaß, U. Czok, T. Dickel, H. Geissel, W. Kinsel, M. Petrick, T. Schäfer, C. Scheidenberger, A versatile triple radiofrequency quadrupole system for cooling, mass separation and bunching of exotic nuclei. Nucl. Instrum. Methods A **880**, 138–151 (2018)
74. M. Smith, M. Brodeur, T. Brunner, S. Ettenauer, A. Lapierre, R. Ringle, V.L. Ryjkov, F. Ames, P. Bricault, G.W.F. Drake, P. Delheij, D. Lunney, F. Sarazin, J. Dilling, First Penning-trap mass measurement of the exotic halo nucleus ^{11}Li. Phys. Rev. Lett. **101**, 202501 (2008)
75. T. Marketin, L. Huther, G. Martinez-Pinedo, Large-scale evaluation of β-decay rates of r-process nuclei with the inclusion of first-forbidden transitions. Phys. Rev. C **93**, 025805 (2016)
76. J. Gerhold, Properties of cryogenic insulants. Cryogenics **38**, 1063–1081 (1998)
77. M.A. Liebermann, A.J. Lichtenberg, *Principles of Plasma Discharges and Materials Processing*, 2nd edn. (Wiley, Hoboken, New Jersey, 2005)
78. L.A. Viehland, Zero-field mobilities in helium: highly accurate values for use in ion mobility spectrometry. Int. J. Ion Mobil. Spec. **15**, 21–29 (2012)
79. M. Huyse, M. Facina, Y. Kudryavtsev, P.V. Duppen, Intensity limitations of a gas cell for stopping, storing and guiding of radioactive ions. Nucl. Instrum. Methods B **187**, 535–547 (2002)
80. A. Takamine, M. Wada, Y. Ishida, T. Nakamura, K. Okada, Y. Yamazaki, T. Kambara, Y. Kanai, T.M. Kojima, Y. Nakai, N. Oshima, A. Yoshida, T. Kubo, S. Ohtani, K. Noda, I. Katayama, P. Hostain, V. Varentsov, H. Wollnik, Space-charge effects in the catcher gas cell of a rf ion guide. Rev. Sci. Instrum. **76**, 103503 (2005)
81. D.J. Morrissey, Extraction of thermalized projectile fragments from gas. Eur. Phys. J. Spec. Top. **150**, 365–366 (2007)
82. I.D. Moore, New concepts for the ion guide technique. Nucl. Instrum. Methods B **266**, 4434–4441 (2008)
83. M. Facina, C. Bachelet, M. Block, G. Bollen, D. Davies, C.M. Folden III., C. Guenaut, J. Huikari, E. Kwan, D.J. Morrissey, G.K. Pang, A. Prinke, R. Ringle, J. Savory, P. Schury, S. Schwarz, C. Sumithrarachchi, T. Sun, Charged particle transport and extraction studies in the NSCL gas cell for stopping radioactive fragments. Nucl. Instrum. Methods B **266**, 4471–4474 (2008)
84. G. Savard, Large radio-frequency gas catchers and the production of radioactive nuclear beams. J. Phys: Conf. Ser. **312**, 052004 (2011)
85. R. Ringle, G. Bollen, K. Lund, C. Nicoloff, S. Schwarz, C. Sumithrarachchi, A. Villari, Particle-in-cell techniques for the study of space charge effects in the Advanced Cryogenic Gas Stopper. Nucl. Instrum. Methods B **496**, 61–70 (2021)
86. F. Heiße, Investigation of the cryogenic gas-filled stopping cell for the FRS Ion Catcher. Master thesis, Technische Universität Dresden (2015)
87. A. Kramida, Y. Ralchenko, J. Reader, N.A. Team, NIST Atomic Spectra Database (Version 5.6.1). https://physics.nist.gov/asd, National Institute of Standards and Technology, Gaithersburg, MD, USA (2018)
88. P. Dendooven, S. Purushothaman, K. Gloos, On a cryogenic noble gas ion catcher. Nucl. Instrum. Methods A **558**, 580–583 (2006)
89. S. Purushothaman, P. Dendooven, I. Moore, H. Penttila, J. Ronkainen, A. Saastamoinen, J. Äystö, K. Peräjärvi, N. Takahashi, K. Gloos, Cryogenic helium as stopping medium for high-energy ions. Nucl. Instrum. Methods B **266**, 4488–4492 (2008)
90. P.D. Bentley, The modern cryopump. Vacuum **30**, 145–158 (1980)
91. A. Jaries, J. Ruotsalainen, R. Kronholm, T. Eronen, A. Kankainen, HIBISCUS: a new ion beam radio-frequency quadrupole cooler-buncher for high-precision experiments with exotic radioactive ions. Nucl. Instrum. Methods A **1073**, 170273 (2025)
92. F. Herfurth, W.R. Plaß, Evaluation of options for the LEB slow beam facility. Internal report, GSI Helmoltzzentrum für Schwerionenforschung (2016)
93. F. Herfurth, J. Dilling, A. Kellerbauer, G. Bollen, S. Henry, H.-J. Kluge, E. Lamoura, D. Lunney, R.B. Moore, C. Scheidenberger, S. Schwarz, G. Sikler, J. Szerypo, A linear radiofrequency ion trap for accumulation, bunching, and emittance improvement of radioactive ion beams. Nucl. Instrum. Methods A **469**, 254–275 (2001)
94. T. Brunner, M.J. Smith, M. Brodeur, S. Ettenauer, A.T. Gallant, V.V. Simon, A. Chaudhuri, A. Lapierre, E. Mane, R. Ringle, M.C. Simon, J.A. Vaz, P. Delheij, M. Good, M.R. Pearson, J. Dilling, TITAN's digital RFQ ion beam cooler and buncher, operation and performance. Nucl. Instrum. Methods A **676**, 32–43 (2012)
95. M. Rosenbusch, D. Atanasov, K. Blaum, C. Borgmann, S. Kreim, D. Lunney, V. Manea, L. Schweikhard, F. Wienholtz, R.N. Wolf, Ion bunch stacking in a Penning trap after purification in an electrostatic mirror trap. Appl. Phys. B **114**, 147–155 (2014)
96. M. Maier, New applications for slowing down of high-energy heavy ions. PhD thesis, Justus Liebig University Gießen (2004)
97. S. Eliseev, Design, construction and commissioning of an ortho-TOF mass spectrometer for investigations of exotic nuclei. PhD thesis, Justus Liebig University Gießen (2004)
98. M. Petrick, Aufbau und Erprobung einer neuartigen Separationsmethode für exotische Kerne bei relativistischen Energien. PhD thesis, Justus Liebig University Gießen (2008)
99. D. Schäfer, Design and simulation of a cryogenic stopping cell for the low-energy branch of the Super-FRS at FAIR. Diplomarbeit, Justus Liebig University Gießen (2010)

100. F. Greiner, Collision-induced dissociation - an effective method for removing molecular contaminants in beams of short-lived nuclei (in German). Master thesis, Justus Liebig University Gießen (2017)
101. I. Miskun, A novel method for the measurement of half-lives and decay branching ratios of exotic nuclei with the FRS Ion Catcher. PhD thesis, Justus Liebig University Gießen (2019)
102. A. Mollaebrahimi, Mass and half-life measurements of neutron-deficient isotopes with $A \sim 100$ and developments for the FRS Ion Catcher and CISE. PhD thesis, University of Groningen (2021)
103. A.N. State, S. Beck, D. Amanbayev, D.L. Balabanski, H. Brand, P. Constantin, T. Dickel, C. Hornung, D. Nichita, W.R. Plaß, H. Roesch, A. Rotaru, C. Scheidenberger, J. Siebring, A. Spataru, N. Tortorelli, J. Zhao, The slow control system of the FRS Ion Catcher. Nucl. Instrum. Methods A **1034**, 166772 (2022)
104. A. Mollaebrahimi, D. Amanbayev, S. Ayet San Andrés, S. Beck, J. Bergmann, T. Dickel, H. Geissel, C. Hornung, N. Kalantar-Nayestanaki, G. Kripko-Koncz, I. Miskun, D. Nichita, W.R. Plaß, I. Pohjalainen, C. Scheidenberger, G. Stanic, A. State, J. Zhao, Recent upgrades of the gas handling system for the cryogenic stopping cell of the FRS Ion Catcher. Nucl. Instrum. Methods A **1055**, 168554 (2023)
105. R. Janik, A. Prochazka, B. Sitar, P. Strmen, I. Szarka, H. Geissel, K.-H. Behr, C. Karagiannis, C. Nociforo, H. Weick, M. Winkler, Time projection chambers with C-pads for heavy-ion tracking. Nucl. Intrum. Methods A **640**, 54–57 (2011)
106. M. Pfützner, H. Geissel, G. Münzenberg, F. Nickel, C. Scheidenberger, K.-H. Schmidt, K. Sümmerer, T. Brohm, B. Voss, H. Bichsel, Energy deposition by relativistic heavy ions in thin argon absorbers. Nucl. Instrum. Methods B **86**, 213–218 (1994)
107. A. Stolz, T. Faestermann, H.-J. Körner, R. Schneider, E. Wefers, S. Winkler, A detector system for the identification of relativistic heavy ions at high rates. GSI Sci. Rep. **1998**, 174 (1999)
108. W.R. Plaß, T. Dickel, M. Petrick, D. Boutin, Z. Di, T. Fleckenstein, H. Geissel, C. Jesch, C. Scheidenberger, Z. Wang, An RF quadrupole-time-of-flight system for isobar-separation and multiplexed low energy rare-isotope beam experiments. Eur. Phys. J. Spec. Top. **150**, 367–368 (2007)
109. A. Simon, Entwicklung und Test eines CFK-basierten RF-Quadrupols für ein Multireflektions-Flugzeitmassenspektrometer. Bachelor thesis, Justus Liebig University Gießen (2008)
110. M.P. Reiter, Simulation of the cryogenic stopping cell of the FRS ion catcher experiment and construction of a novel RFQ beam line system. Master thesis, Justus Liebig University Gießen (2011)
111. I. Miskun, Commissioning, performance and possible applications of RFQ mass-filter in the diagnostic unit of the FRS Ion Catcher facility. Diploma thesis, Tomsk Polytechnical University, Russia (2015)
112. W.R. Plaß, T. Dickel, U. Czok, H. Geissel, M. Petrick, K. Reinheimer, C. Scheidenberger, M.I. Yavor, Isobar separation by time-of-flight mass spectrometry for low-energy radioactive ion beam facilities. Nucl. Instrum. Methods B **266**, 4560–4564 (2008)
113. W.R. Plaß, T. Dickel, C. Scheidenberger, Multiple-reflection time-of-flight mass spectrometry. Int. J. Mass Spectrom. **349**, 134–144 (2013)
114. M.I. Yavor, W.R. Plaß, T. Dickel, H. Geissel, C. Scheidenberger, Ion-optical design of a high-performance multiple-reflection time-of-flight mass spectrometer and isobar separator. Int. J. Mass Spectrom. **381–382**, 1–9 (2015)
115. W.R. Plaß, T. Dickel, S. Ayet San Andrés, J. Ebert, F. Greiner, C. Hornung, C. Jesch, J. Lang, W. Lippert, T. Majoros, D. Short, H. Geissel, E. Haettner, M.P. Reiter, A.-K. Rink, C. Scheidenberger, M.I. Yavor, High-performance multiple-reflection time-of-flight mass spectrometers for research with exotic nuclei and for analytical mass spectrometry. Phys. Scr. T **166**, 014069 (2015)
116. T. Dickel, M.I. Yavor, J. Lang, W.R. Plaß, W. Lippert, H. Geissel, C. Scheidenberger, Dynamical time focus shift in multiple-reflection time-of-flight mass spectrometers. Int. J. Mass Spectrom. **412**, 1–7 (2017)
117. N.E. Bradbury, R.A. Nielsen, Absolute values of the electron mobility in hydrogen. Phys. Rev. **49**, 388–393 (1936)
118. J.F. Ziegler, M.D. Ziegler, J.P. Biersack, SRIM: the stopping and range of ions in matter (2010). Nucl. Instrum. Methods B **268**, 1818–1823 (2010)
119. W.R. Leo, *Techniques for Nuclear and Particle Physics Experiments* (Springer, Berlin, Heidelberg, New York, 1994), p.131
120. J.W. Zhao, D. Amanbayev, T. Dickel, I. Miskun, W.R. Plaß, N. Tortorelli, S. Ayet San Andrés, S. Beck, J. Bergmann, Z. Brencic, P. Constantin, H. Geissel, F. Greiner, L. Gröf, C. Hornung, N. Kuzminchuk, G. Kripko-Koncz, I. Mardor, I. Pohjalainen, C. Scheidenberger, P.G. Thirolf, S. Bagchi, E. Haettner, E. Kazantseva, D. Kostyleva, A. Oberstedt, S. Pietri, M.P. Reiter, Y.K. Tanaka, M. Wada, D.L. Balabanski, D. Benyamin, M.N. Harakeh, N. Hubbard, N. Kalantar-Nayestanaki, A. Mollaebrahimi, I. Mukha, M. Narang, T. Niwase, Z. Patyk, S. Purushothaman, A. Rotaru, A. Spataru, G. Stanic, M. Vencelj, H. Weick, J. Yu, Increasing the rate capability for the cryogenic stopping cell of the FRS Ion Catcher. Nucl. Instrum. Methods B **547**, 165175 (2024)
121. A. Rotaru, D. Amanbayev, D.L. Balabanski, D. Benyamin, P. Constantin, T. Dickel, L. Gröf, I. Mardor, I. Miskun, D. Nichita, W.R. Plaß, C. Scheidenberger, A. Spataru, A. State, INCREASE: an in-cell reaction system for multi-nucleon transfer and spontaneous fission at the FRS ion catcher. Nucl. Instrum. Methods B **512**, 83–90 (2022)
122. P. Schury, G. Bollen, M. Block, D. Morrissey, R. Ringle, A. Prinke, J. Savory, S. Schwarz, T. Sun, Beam purification techniques for low energy rare isotope beams from a gas cell. Hyperfine Interact. **173**, 165–170 (2006)
123. I. Miskun, T. Dickel, S. Ayet San Andrés, J. Bergmann, P. Constantin, J. Ebert, H. Geissel, F. Greiner, E. Haettner, C. Hornung et al., Separation of atomic and molecular ions by ion mobility with an RF carpet. Int. J. Mass Spectrom. **459**, 116450 (2021)

124. D.L. Balabanski, F. Ibrahim, A. Krasznahorkay, I. Boztosun, D. Choudhury, S. Coban, P. Constantin, L. Csige, P.V. Cuong, T. Dickel, H. Djapo, I. Dobrin, S. Essabaa, D. Filipescu, S. Franchoo, G. Georgiev, I. Gheorge, D. Ghita, T. Glodariu, M. Gupta, A. Jokinen, J. Kaur, N. Marginean, R. Marginean, I. Moore, H. Pentilla, C. Petcu, W. Plaß, T. Sava, G. Savard, C. Scheidenberger, D. Yordanov, Photofission experiments at ELI-NP. Rom. Rep. Phys. **68**, 621 (2016)
125. I. Mardor, O. Aviv, M. Avrigeanu, D. Berkovits, A. Dahan, T. Dickel, I. Eliyahu, M. Gai, I. Gavish-Segev, S. Halfon, M. Hass, T. Hirsh, B. Kaiser, D. Kijel, A. Kreisel, Y. Mishnayot, I. Mukul, B. Ohayon, M. Paul, A. Perry, H. Rahangdale, J. Rodnizki, G. Ron, R. Sasson-Zukran, A. Shor, I. Silverman, M. Tessler, S. Vaintraub, L. Weissman, The Soreq Applied Research Accelerator Facility (SARAF): overview, research programs and future plans. Eur. Phys. J. A **54**, 91 (2018)
126. D. Amanbayev, Mass measurements at the N = Z and N = 126 limits at the FRS Ion Catcher and development of the Cryogenic Stopping Cell for the Super-FRS. PhD thesis, Justus Liebig University Gießen (2023)
127. G. Bollen, "Ion surfing" with radiofrequency carpets. Int. J. Mass Spetrom. **299**, 131–138 (2011)
128. B. Blank, L. Audirac, G. Canchel, F. Delalee, C.E. Demonchy, J. Giovinazzo, L. Hay, P. Hellmuth, J. Huikari, S. LeBlanc, S. List, C. Marchand, I. Matea, J.-L. Pedroza, J. Pibernat, A. Rebii, L. Serani, D. Oliveira Santos, S. Grevy, L. Perrot, C. Stodel, J.C. Thomas, C. Borcea, C. Dossat, R. Oliveira, A time projection chamber to study two-proton radioactivity. Nucl. Instrum. Meth. B **266**, 4606–4611 (2008)
129. F. Sauli, GEM: a new concept for electron amplification in gas detectors. Nucl. Instrum. Meth. A **386**, 531–534 (1997)
130. M.P. Lener, G. Corradi, C. Curceanu, D. Tagnani, A.R. Vidal, J. Zmeskal, Performance of an active target GEM-based TPC for the AMADEUS experiment. Mod. Instrum. **4**, 32–41 (2015)
131. T. Sonoda, T. Tsubota, M. Wada, I. Katayama, T.M. Kojima, M. Reponen, A gas circulation and purification system for gas-cell-based low-energy RI-beam production. Rev. Sci. Instrum. **87**, 065104 (2016)
132. D.A. Dahl, SIMION for the personal computer in reflection. Int. J. Mass Spectrom. **200**, 3–25 (2000)
133. D.J. Manura, D.A. Dahl, SIMION 8.0 User Manual. Sci. Instrument Services, Inc., Idaho Nat. Lab., (2006). Sci. Instrument Services, Inc., Idaho Nat. Lab
134. W.R. Plaß, The dependence of RF ion trap mass spectrometer performance on electrode geometry and collisional processes. PhD thesis, Justus Liebig University Gießen (2001)
135. G. Wu, R.G. Cooks, Z. Ouyang, M. Yu, W.J. Chappell, W.R. Plass, Ion trajectory simulation for electrode configurations with arbitrary geometries. J. Am. Soc. Mass Spectrom. **17**, 1216–1228 (2006)
136. W.R. Plaß, T. Dickel, B. Fabian, E. Haettner, An advanced concept for mass spectrometry simulations – the Ion Trajectory Simulation program ITSIM 6. In: Proceedings of the 56th ASMS Conference on Mass Spectrometry and Allied Topics, Denver, USA, p. 015 (2008)
137. W.R. Plass, L.A. Gill, H.A. Bui, R.G. Cooks, Ion mobility measurements by Dc tomography in an Rf quadrupole ion trap. J. Phys. Chem. A **104**, 5059–5065 (2000)
138. A. Hamaker, M. Brodeur, J.M. Kelly, J. Long, C. Nicoloff, S. Ryan, B.E. Schultz, P. Schury, M. Wada, Experimental investigation of the repelling force from RF carpets. Int. J. Mass Spectrom. **404**, 14–19 (2016)
139. P.L. Patterson, Temperature dependence of helium-ion mobilities. Phys. Rev. A **2**, 1154 (1970)
140. S. Purushothaman, Superfluid helium and cryogenic noble gases as stopping media for ion catchers. PhD thesis, University of Groningen (2008)
141. M. Brodeur, A.E. Gehring, G. Bollen, S. Schwarz, D.J. Morrissey, Experimental investigation of the ion surfing transport method. Int. J. Mass Spetrom. **336**, 53–60 (2013)
142. F. Greiner, Construction and commissioning of an RF quadrupole switchyard (in German). Bachelor thesis, Justus Liebig University Gießen (2013)
143. W.M. Brubaker, An improved quadrupole mass analyser. Advances in mass spectrometry **4**, 293–299 (1968)
144. A.-N. State, Ion transport and extraction with gas flows in next generation ion catchers. PhD thesis, University Polytechnica of Bucharest (2022)
145. R. Baartman, Low energy beam transport design optimization for RIBs. Nucl. Instrum. Methods B **204**, 92–399 (2003)